



**Lappeenranta University of Technology**

School of Engineering Science

Degree Program in Chemical and Process Engineering

M.Sc. Thesis

**Photocatalytic degradation of Benzophenone 3 in aqueous media under UV light  
irradiation**

Author: Anjan Deb

Examiner: Professor Mika Sillanpää

Head, Department of Green Chemistry, 50130 Mikkeli, Finland

Supervisor: Zhao Wang

Junior Researcher, Department of Green Chemistry, 50130 Mikkeli, Finland

**ABSTRACT**

Lappeenranta University of Technology  
School of Engineering Science  
Degree program in Chemical and Process Engineering  
Department of Green Chemistry

Anjan Deb

**Photocatalytic degradation of Benzophenone 3 in aqueous media under UV light irradiation**

Master's Thesis

2018

90 pages, 45 figures, 14 tables

**Keywords:** UV filters, BP-3, Photocatalytic water treatment, Emerging contaminants.

Benzophenone-3 (BP-3), an organic UV filter widely used in sunscreen and other personal care products, has been detected at several ppm level in surface and ground water, which could significantly affect the human health and aquatic environment. In this study, the photocatalytic degradation of BP-3 along with optimal operating conditions such as initial pH, initial concentration, catalysts loading, degradation kinetics and efficiency, degree of mineralization was investigated. Two different catalysts composite, PbO/TiO<sub>2</sub> and Sb<sub>2</sub>O<sub>3</sub>/TiO<sub>2</sub>, were synthesized by hydrothermal methods. Synthesized catalysts were further characterized by XRD, SEM, EDS, BET and UV-Vis DRS techniques to investigate the crystalline properties, surface morphologies, elemental analysis, textural properties and the optical properties respectively. Photocatalytic experiments under UV-C irradiation demonstrated the complete removal of BP-3 using PbO/TiO<sub>2</sub> catalyst within 120 min. Pollutant degradation rate and removal efficiency was higher at pH 7 when the initial contaminant concentration was 20µM and the catalysts dose was 0.75 g/L.

## ACKNOWLEDGEMENTS

This research was accomplished at the Laboratory of Green Chemistry (LGC), Mikkeli, Finland from November 2017 to February 2018.

First of all, I remain beholden to Prof. Mika Sillanpää for providing me the opportunity to execute my M.Sc thesis at the LGC along with his inspirations and encouragements.

Accordingly, my earnest appreciation goes to Zhao Wang, my supervisor, who provided me the necessary guidelines to carry out my experiments in the laboratory. Also, her encouragement to perform the research experiment independently helps me to learn the valuable decision-making strategy.

I am grateful to Varsha Srivastava for helping in BET and XRD analysis and thankful to Nancy and Tam for helping in HPLC analysis. Also, special thank goes to Jannatul Ferdous Rumky for supporting me always.

I would like to thank all LGC researchers for their good and kind behavior and thankful to XAMK and Aalto University for helping in SEM and UV-Vis DRS analysis.

Finally, I would like to express my honest gratitude to my parents, siblings and all friends and well-wishers.

Anjan Deb

29<sup>th</sup> May 2018

Finland

## TABLE OF CONTENTS

ABSTRACT.....	I
ACKNOWLEDGEMENTS.....	II
TABLE OF CONTENTS.....	III
LIST OF FIGURES .....	V
LIST OF TABLES .....	VIII
LIST OF SYMBOLS AND ABBREVIATIONS .....	IX
1. Introduction .....	1
1.1. Aim and Objective .....	3
2. Treatment of Organic Contaminants in Wastewater .....	4
2.1. Contaminants of emerging concern.....	4
2.2. Advanced technologies for abatement of organic pollutants (OP) in water .....	6
2.3. Advanced oxidation process.....	8
3. Photocatalysis .....	10
3.1. Fundamental mechanism of photocatalytic pollutant degradation.....	10
3.2. Advanced materials in photocatalytic water treatment .....	12
3.3. Strategies for improved photocatalytic performance .....	17
3.3.1. Bandgap engineering .....	18
3.3.2. Morphological Improvement .....	20
3.3.3. Dye sensitization.....	20
3.3.4. Composite semiconductors .....	21
4. Literature Review .....	23
4.1. UV Filters.....	23
4.2. Organic UV filters and their characteristics.....	23
4.3. Toxicological impact of UV filters in environment and aquatic life .....	24
4.4. Degradation of organic UV filters by AOPs .....	26
5. Materials and Methods .....	29
5.1. Chemicals.....	29
5.2. Catalyst synthesis methods.....	29
5.2.1. Synthesis of TiO <sub>2</sub> by sol-gel method .....	29
5.2.2. Synthesis of PbO/TiO <sub>2</sub> .....	30

5.2.3.	Synthesis of $\text{Sb}_2\text{O}_3/\text{TiO}_2$ .....	32
5.3.	Characterization methods.....	34
5.3.1.	XRD analysis .....	34
5.3.2.	SEM and EDX analysis .....	34
5.3.3.	BET Analysis .....	34
5.3.4.	UV-Vis diffuse reflectance spectra.....	34
5.4.	Photocatalytic Experiment .....	35
5.5.	Analytical Methods .....	36
5.5.1.	HPLC method for BP-3 analysis.....	36
5.5.2.	GC-MS for identification of degradation intermediates .....	36
5.5.3.	Methods of TOC determination.....	36
6.	Result and Discussion.....	37
6.1.	Characterization of catalysts .....	37
6.1.1.	XRD Analysis .....	37
6.1.2.	SEM Analysis .....	39
6.1.3.	EDS Analysis .....	41
6.1.4.	BET Analysis .....	43
6.1.5.	Optical properties of the synthesized catalysts .....	45
6.2.	Photocatalytic performance of synthesized catalysts.....	46
6.3.	Effect of Initial pH .....	47
6.4.	Effect of catalysts dose.....	49
6.5.	Effect of initial concentration.....	51
6.6.	Mineralization study.....	55
6.7.	Identification of degradation byproducts .....	56
7.	Conclusion and Recommendation .....	57
	References.....	58
	Appendix.....	74

## LIST OF FIGURES

Figure 2.1: Major sources and typical pathways for ground and surface water pollution by ECs. (Source: (Lapworth et al., 2012)) .....	6
Figure 2.2: Organic Pollutant (OP) removal methods from wastewater.....	7
Figure 3.1: Schematic of Photocatalytic Process (Pelaez et al., 2012). .....	11
Figure 3.2: Thermodynamic requirements for water treatment (A) and solar fuel production (B) (Li et al., 2018). .....	18
Figure 3.3: Improvement of photocatalytic process by dye sensitization process (Rehman et al., 2009). .	21
Figure 3.4: Different types of heterojunction composites (Marschall, 2014). .....	21
Figure 5.1: Synthesis process of PbO/TiO <sub>2</sub> nanocatalysts. ....	31
Figure 5.2: Synthesis process of Sb <sub>2</sub> O <sub>3</sub> /TiO <sub>2</sub> nanocatalysts.....	33
Figure 6.1: XRD patterns of synthesized PbO/TiO <sub>2</sub> catalysts of different ratio. ....	37
Figure 6.2: XRD patterns of synthesized Sb <sub>2</sub> O <sub>3</sub> /TiO <sub>2</sub> catalysts of different ratio.....	38
Figure 6.3: SEM micrograph of synthesized PbO/TiO <sub>2</sub> photocatalysts (a&b: PbO/TiO <sub>2</sub> = 1:2; c&d: PbO/TiO <sub>2</sub> = 1:1; e&f: PbO/TiO <sub>2</sub> = 2:1). ....	39
Figure 6.4: SEM micrograph of synthesized Sb <sub>2</sub> O <sub>3</sub> /TiO <sub>2</sub> photocatalysts (a&b: Sb <sub>2</sub> O <sub>3</sub> /TiO <sub>2</sub> = 1:2; c&d: Sb <sub>2</sub> O <sub>3</sub> /TiO <sub>2</sub> = 1:1; e&f: Sb <sub>2</sub> O <sub>3</sub> /TiO <sub>2</sub> = 2:1).....	40
Figure 6.5: EDS spectrum of PbO/TiO <sub>2</sub> (1:2).....	41
Figure 6.6: EDS spectrum of PbO/TiO <sub>2</sub> (1:1).....	41
Figure 6.7: EDS spectrum of PbO/TiO <sub>2</sub> (2:1).....	41
Figure 6.8: EDS spectrum of Sb <sub>2</sub> O <sub>3</sub> /TiO <sub>2</sub> (1:1).....	42
Figure 6.9: EDS spectrum of Sb <sub>2</sub> O <sub>3</sub> /TiO <sub>2</sub> (2:1).....	42
Figure 6.10: EDS spectrum of Sb <sub>2</sub> O <sub>3</sub> /TiO <sub>2</sub> (1:2).....	42
Figure 6.11: N <sub>2</sub> adsorption-desorption isotherm of PbO/TiO <sub>2</sub> photocatalysts.....	43
Figure 6.12: Pore size distribution of PbO/TiO <sub>2</sub> photocatalysts. ....	43
Figure 6.13: N <sub>2</sub> adsorption-desorption isotherm of Sb <sub>2</sub> O <sub>3</sub> /TiO <sub>2</sub> photocatalysts.....	44

Figure 6.14: Pore size distribution of $\text{Sb}_2\text{O}_3/\text{TiO}_2$ photocatalysts.....	44
Figure 6.15: UV-Vis DR spectra of $\text{PbO}/\text{TiO}_2$ photocatalysts.....	45
Figure 6.16: Plot of $(\alpha h\nu)^2$ vs. photon energy ( $h\nu$ ) for bandgap estimation of $\text{PbO}/\text{TiO}_2$ photocatalysts...	45
Figure 6.17: UV-Vis DR spectra of $\text{Sb}_2\text{O}_3/\text{TiO}_2$ photocatalysts. ....	45
Figure 6.18: Plot of $(\alpha h\nu)^2$ vs. photon energy ( $h\nu$ ) for bandgap estimation of $\text{Sb}_2\text{O}_3/\text{TiO}_2$ photocatalysts.	45
Figure 6.19: Performance testing of synthesized catalysts (Catalysts dose: 1g/L, Initial conc.: 20 $\mu\text{M}$ , Irradiation time: 2 hr).....	46
Figure 6.20: Effect of Initial pH on overall removal of pollutant by $\text{PbO}/\text{TiO}_2$ catalysts (Initial concentration = 20 $\mu\text{M}$ , Catalyst dose = 1g/L, UVC irradiation time = 120 min). ....	47
Figure 6.21: Effect of Initial pH on the photocatalytic degradation of pollutant by $\text{PbO}/\text{TiO}_2$ catalysts (Initial concentration = 20 $\mu\text{M}$ , Catalyst dose = 1g/L, UVC irradiation time = 120 min).....	47
Figure 6.22: Effect of Initial pH on overall removal of pollutant by $\text{Sb}_2\text{O}_3/\text{TiO}_2$ catalysts (Initial concentration = 20 $\mu\text{M}$ , Catalyst dose = 1g/L, UVC irradiation time = 120 min).....	48
Figure 6.23: Effect of Initial pH on photocatalytic degradation of pollutant by $\text{Sb}_2\text{O}_3/\text{TiO}_2$ catalysts (Initial concentration = 20 $\mu\text{M}$ , Catalyst dose = 1g/L, UVC irradiation time = 120 min).....	48
Figure 6.24: Effect of catalysts ( $\text{PbO}/\text{TiO}_2$ (2:1)) dose on BP-3 degradation (Initial pH = 7, Initial concentration = 20 $\mu\text{M}$ , UVC irradiation time = 120 min).....	49
Figure 6.25: Effect of catalysts ( $\text{Sb}_2\text{O}_3/\text{TiO}_2$ (2:1)) dose on BP-3 degradation (Initial pH = 9, Initial concentration = 20 $\mu\text{M}$ , UVC irradiation time = 120 min).....	50
Figure 6.26: Effect of initial pollutant concentration on the degradation of BP-3 by $\text{PbO}/\text{TiO}_2$ (2:1) catalyst (Initial pH = 7, Catalyst dose = 0.75 g/L, UVC irradiation time = 120 min).....	51
Figure 6.27: Degradation kinetics of BP-3 by ( $\text{PbO}/\text{TiO}_2$ (2:1)) at different initial concentration of pollutant (Initial pH = 7, Catalyst dose = 0.75 g/L).....	52
Figure 6.28: Degradation kinetics modelling of BP-3 by ( $\text{PbO}/\text{TiO}_2$ (2:1)) at different initial concentration of pollutant (Initial pH = 7, Catalyst dose = 0.75 g/L).....	52
Figure 6.29: Effect of initial pollutant concentration on the degradation of BP-3 by $\text{Sb}_2\text{O}_3/\text{TiO}_2$ (2:1) catalyst (Initial pH = 7, Catalyst dose = 0.25 g/L, UVC irradiation time = 120 min).....	53
Figure 6.30: Degradation kinetics of BP-3 by ( $\text{Sb}_2\text{O}_3/\text{TiO}_2$ (2:1)) at different initial concentration of pollutant (Initial pH = 7, Catalyst dose = 0.25 g/L).....	54

Figure 6.31: Degradation kinetics modelling of BP-3 by ( $\text{Sb}_2\text{O}_3/\text{TiO}_2$ (2:1)) at different initial concentration of pollutant (Initial pH = 7, Catalyst dose = 0.25 g/L).....	54
Figure 6.33: Mineralization efficiency of $\text{PbO}/\text{TiO}_2$ (2:1) catalysts at different catalysts loading (Initial pH = 7, Initial concentration = 20 $\mu\text{M}$ , UV-C irradiation time = 120 min).....	55
Figure 6.34: Mineralization efficiency of $\text{PbO}/\text{TiO}_2$ (2:1) catalysts at different Initial Concentration (Initial pH = 7, Catalyst dose = 0.75 g/L, UV-C irradiation time = 120 min). ....	55
Figure 6.35: Mineralization efficiency of $\text{Sb}_2\text{O}_3/\text{TiO}_2$ (2:1) catalysts at different catalysts loading (Initial pH = 9, Initial concentration = 20 $\mu\text{M}$ , UV-C irradiation time = 120 min). ....	55
Figure 6.36: Mineralization efficiency of $\text{Sb}_2\text{O}_3/\text{TiO}_2$ (2:1) catalysts at different Initial Concentration (Initial pH = 9, Catalyst dose = 0.25 g/L, UV-C irradiation time = 120 min). ....	55
Figure 6.37: Possible degradation byproducts from photocatalytic degradation of BP-3.....	56

**LIST OF TABLES**

Table 2.1: Concentrations of ECs in wastewater from different research	4
Table 2.2: AOPs with corresponding reactions for the production of reactive free-radicals (Alok D Bokare and Choi, 2014; Hu and Long, 2016; Sirés et al., 2014)	9
Table 3.1: Principle characteristics of some promising photocatalytic materials.	12
Table 4.1: Molecular structure and physico-chemical properties of some commonly used UV filters	23
Table 4.2: UV filters concentration in swimming pool water	25
Table 4.3: Summary of AOP methods used for UV filter degradation.	27
Table 5.1: Required amount of lead nitrate and titanium butoxide for synthesis	30
Table 5.2: Required amount of antimony trichloride and titanium dioxide for synthesis	32
Table 6.1: Mass and Atomic composition of PbO/TiO <sub>2</sub> catalysts from EDS data.	41
Table 6.2: Mass and Atomic composition of Sb <sub>2</sub> O <sub>3</sub> /TiO <sub>2</sub> catalysts from EDS data	42
Table 6.3: Physical properties of PbO/TiO <sub>2</sub> catalysts.	43
Table 6.4: Physical properties of Sb <sub>2</sub> O <sub>3</sub> /TiO <sub>2</sub> catalysts.	44
Table 6.5: Kinetic parameters of BP-3 degradation by (PbO/TiO <sub>2</sub> (2:1)) at different initial concentration.	53
Table 6.6: Kinetic parameters of BP-3 degradation by (Sb <sub>2</sub> O <sub>3</sub> /TiO <sub>2</sub> (2:1)) at different initial concentration.	54

**LIST OF SYMBOLS AND ABBREVIATIONS**

AOP	advanced oxidative processes
BG	band gap
BP-3	benzophenone 3
COD	chemical oxygen demand
CB	conduction band
DRS	diffuse reflectance spectra
$e^-$	electron
EDS	endocrine disrupting compounds
FTIR	fourier transform infra-red
GC-MS	gas chromatography mass spectroscopy
$h^+$	hole
HPLC	high performance liquid chromatography
NaOH	sodium hydroxide
Nps	nanoparticles
OH	hydroxyl group
$\cdot$ OH	hydroxyl radical
PCPs	Personal Care Products
SEM	scanning electron microscopy
SPE	solid phase extraction
TEM	transmission electron microscopy
TOC	total organic carbon
TM	transition metal
UV	ultraviolet
UV-Vis	ultraviolet-visible
VB	valence band
XRD	x-ray diffraction
$\mu$ M	micro molar

## 1. INTRODUCTION

Water is the most fundamental elements for the survival of all the living beings on this earth. Approximately, 71% of our earth exterior is camouflaged with water which accounts for a volume of  $1.39 \times 10^9$  km<sup>3</sup>. However, only 2.5% of it can be claimed as clean or fresh water and almost 69% of this fresh water are stored in polar glaciers while the remaining amounts are available for beneficial uses. Out of this available fresh water only 7% is used for domestic purposes like drinking, cooking, bathing and washing, whereas the rest amounts are consumed in agricultural and industrial purposes (Sillanpää et al., 2017). Therefore, a scarcity of fresh water is obvious around the world. It has been reported that, more than 120 million people in our planet have lack access to clean drinking water; 260 million are out of sanitation facilities and millions are dying annually from the diseases associated with water pollution (Vasudevan and Oturan, 2014). Apart from that, industrial development, agricultural advancement and the improved way of living is continuously introducing new types of pollutants into the water system as well as our environment. These new types of contaminants include PCPs, pharmaceuticals, pesticides, flame retardants, surfactants and other numerous industrial additives. Collectively these are known as contaminants of emerging concern (Jorgenson et al., 2018; Pennington et al., 2018). Recently these types of contaminants are detected in a significant level into the soil and aquatic environment that were unregulated previously. Also, their harmful effects on the living being such as human and the aquatic organisms are identified by many researchers (Díaz-Cruz et al., 2012; Lambropoulou et al., 2002; Santos et al., 2012; Schlumpf et al., 2004). Therefore, researchers around the world are now trying to find out a way to get rid of these types of pollutants.

Among these various emerging contaminants, UV filters are drawing attention due to their existence in surface and tap water in a significant level. UV filters are mainly aromatic compounds sometimes conjugated with aliphatic double bond or carbonyl groups, used extensively in sunscreen lotion and PCPs to protect our skin from the harmful effect of UV radiation from the sun (Serpone et al., 2007; Shaath, 1987). Their exposure into the environment happens during the bathing and recreational activities in beach, lake, river and swimming pool. UV filters are usually photostable compound with the ability of absorption or reflection of the UV radiation. However, in aqueous environment they may undergo some photodegradation and produce harmful by

products that are threatening to the aquatic species (Jorgenson et al., 2018; Krause et al., 2018; Vione et al., 2013).

Advanced oxidation process (AOP) is an effective method that can be used to fight against this type of contaminants effectively. Recently AOPs are gaining extensive attention due to its non-selective nature regarding pollutant degradation and possibility of complete mineralization of pollutants (Sillanpää et al., 2018). During AOP *in situ* formation of strong oxidative species, such as hydroxyl radicals ( $\bullet\text{OH}$ ), take place which can degrade the organic contaminants into carbon dioxide and water. Among the various AOP methods, heterogeneous photocatalysis is considered as a promising method to get remediation from the organic pollutants (Ohtani, 2011; Pelaez et al., 2012). Besides, photocatalysts use the light energy to generate oxidative radicals which is considered as a green and sustainable approach for water treatment.

Generally, different semiconductors of metal oxide, such as  $\text{TiO}_2$ ,  $\text{ZnO}$ ,  $\text{Cu}_2\text{O}$  has been reported to perform well in photocatalytic water treatment. However, some shortcomings like higher bandgap and fast electron-hole recombination rate impedes the practical application of these materials in water treatment. To overcome these shortcomings several strategies are being applied by the researchers which includes bandgap engineering, morphological improvement, metal oxide composites formation etc. Coupling of metal oxides with suitable energy levels and band positions can reduce the  $e^-/h^+$  recombination rate by transferring the photogenerated  $e^-$  and  $h^+$  to the more negative CB and positive VB, respectively. Recently, Iwaszuk and Nolan reported that the lead oxide modified  $\text{TiO}_2$  established new states over the VB which results the hole movement to the  $\text{PbO}$  surface and electrons placement at the  $\text{TiO}_2$  surface (Iwaszuk and Nolan, 2013). Therefore, an improved charge carrier separation with enhanced photocatalytic performance of  $\text{PbO}/\text{TiO}_2$  is expected. On the other hand,  $\text{Sb}_2\text{O}_3$  (b.g.-3.0 eV) has a smaller band gap than  $\text{TiO}_2$  (b.g.-3.2 eV) and the VB and CB position of  $\text{Sb}_2\text{O}_3$  is below the  $\text{TiO}_2$  which ensues the transfer of VB holes in the  $\text{TiO}_2$  surface and localization of CB electrons on the  $\text{Sb}_2\text{O}_3$  surface (Liu et al., 2012). In this thesis an effort was made to synthesis the semiconductor composites,  $\text{PbO}/\text{TiO}_2$  and  $\text{Sb}_2\text{O}_3/\text{TiO}_2$  and study its application in the degradation of organic UV filter Benzophenone-3.

## 1.1. Aim and Objective

The aim of this study is to investigate the degradation of BP-3 by photocatalysis. To reach this goal the following objectives were made and studied:

- Synthesis of semiconductor composites  $\text{PbO/TiO}_2$  and  $\text{Sb}_2\text{O}_3/\text{TiO}_2$  for improved photocatalytic efficiency.
- Characterization of the synthesized composite photocatalyst to evaluate its structural, optical and chemical properties.
- Study of photocatalytic performance of the produced catalysts by degradation of BP-3 in aqueous environment.
- Study the effect of different operating conditions on photocatalytic degradation of BP-3.
- Study the degree of mineralization.
- Identification of the degradation by-products using GC-MS analysis.

## 2. TREATMENT OF ORGANIC CONTAMINANTS IN WASTEWATER

### 2.1. Contaminants of emerging concern

Emerging contaminants (ECs) are new type of pollutants that have been detected in the air, soil, food chain and aquatic environment in a very trace ( $\mu\text{g/L}$  or  $\text{ng/L}$ ) level. These types of pollutants are identified very recently and their fate and transportation through the environment are not well established yet due to the lack of knowledge regarding their analytical identification (Lapworth et al., 2012; Naidu et al., 2016). Consequently, their effects on ecosystem as well as on human health are not recognized very well. ECs are now detected at various level of concentrations in surface water, ground water and effluents of wastewater treatment plant as listed in Table 2.1.

Table 2.1: Concentrations of ECs in wastewater from different research

ECs	Compounds	Detected conc. (ng/L)	References
Pharmaceuticals	Acetaminophen	34.7	(Estévez et al., 2012; Jurado et al., 2012; Radjenović et al., 2008; Teijon et al., 2010)
	Codeine	348.3	
	Carbamazepine	167	
	Diclofenac	477	
	Gemfibrozil	574	
	Ibuprofen	185	
	Ketoprofen	314	
	Mepivacaine	252	
	Naproxen	263	
	Propyphenazone	296	
Pesticides	Atrazine	3450	(Garrido et al., 2000; Jurado et al., 2012; Köck-Schulmeyer et al., 2012; Teijon et al., 2010)
	Alachlor	9950	
	Chlortoluron	1700	
	Chlorfenvinphos	2500	
	Desethylatrazine	1980	
	Dimethoate	2277	
	Malathion	3500	
	Prometryn	1000	
	Simazine	1690	
Terbutylazine	1270		
Industrial Compounds	Bisphenol A	1500	(Bono-Blay et al., 2012; Jurado et al., 2012; Lacorte et al., 2002)
	Nonylphenol	5280	
	Octylphenol	1800	
	Dimethyl phthalate	120	
	Diethyl phthalate	1115	

ECs	Compounds	Detected conc. (ng/L)	References
Personal care products	Benzophenone-3	290	(Bester, 2003; Díaz-Cruz et al., 2012; Jurado et al., 2012)
	Ethylhexyl methoxycinnamate	260	
	Galaxolide	359	
	Octocrylene	170	
	Triclosan	1000	
Drugs of abuse	3-(4-methylbenzylidene) camphor	35	(Huerta-Fontela et al., 2008; Jurado et al., 2012)
	Cocaine	60.2	
	Benzoyllecgonine	19.6	
	Morphine	27.2	
Life-style compounds	Methadone	68.3	(Huerta-Fontela et al., 2008; Jurado et al., 2012)
	Caffeine	505	
	Nicotine	144	
	Paraxanthine	147	
	Theobromine	252.5	
	Theophylline	35.2	

ECs include a numerous variety of chemicals such as PCPs, pharmaceuticals, pesticides, wastewater treatment effluents (mainly metabolites and degradation byproducts), and very recently identified various carbon-based and metallic nanoparticles (Naidu et al., 2016). Extensive researches are taking place all over the world regarding the identification and fate of ECs along with their effect on environment and human life. Some of the ECs are identified as persistent in our ecosystem and make their way back to human either via food chain or drinking water. Apart from that, some of the ECs are found to be potential to cause undesirable effects on human health such as antibiotic resistance, behavioral alteration, and endocrine disruption (Batt et al., 2017; Naidu et al., 2016).

ECs enter the environment either directly from various sources including effluents of wastewater treatment plant, medical effluents, domestic and industrial wastes, septic tanks, animal manure and waste lagoons or indirectly from surface water-groundwater exchange process (Lapworth et al., 2012; Naidu et al., 2016). Currently operating wastewater treatment plant could not eliminate the ECs and their metabolites completely and they are deposited as sewage effluent which are further discharged into the environment. Consequently, they are entering the environment at a very low concentration, accumulating gradually and causing adverse impact on ecosystems and aquatic

organisms. Figure 2.1 represents the major and minor pathways of the ECs to the environment and aquatic system from different direct and indirect sources.

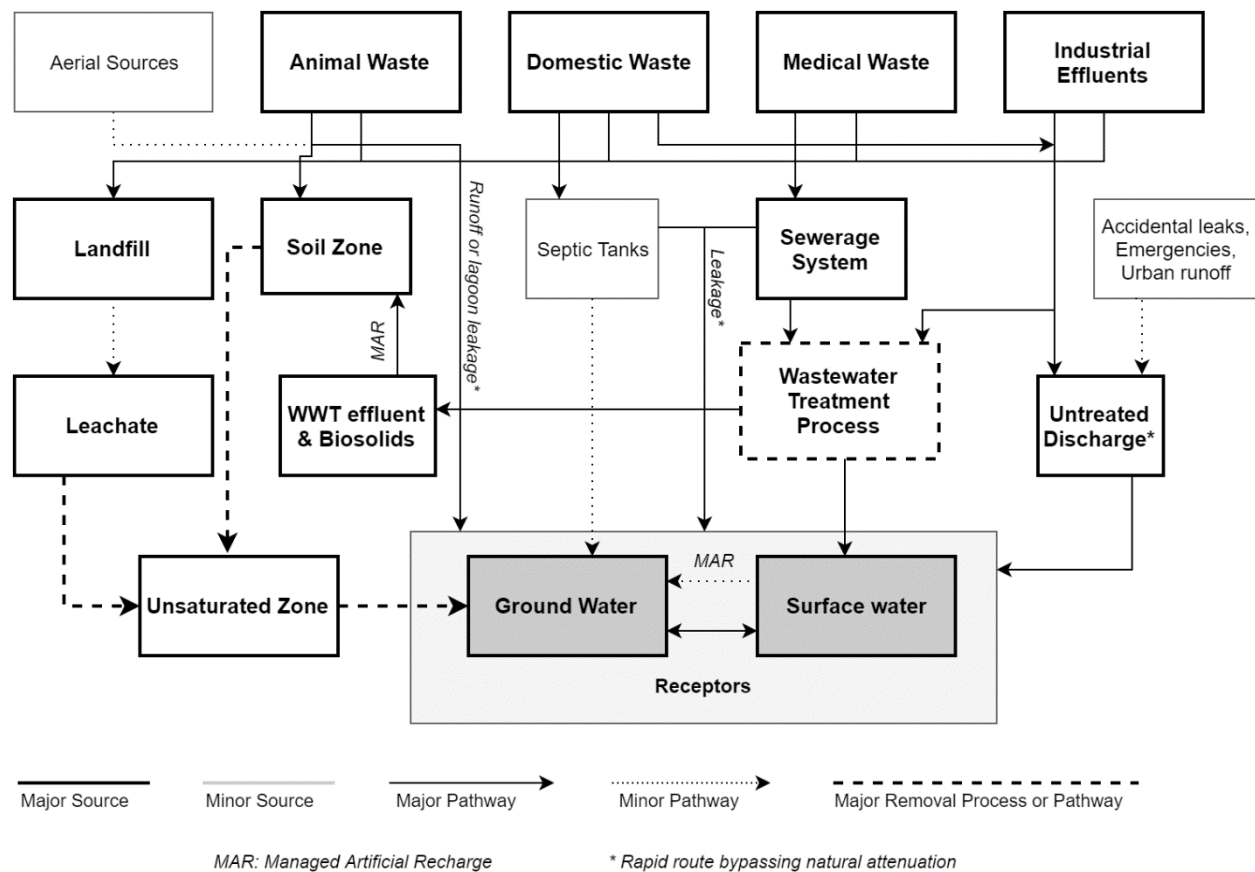


Figure 2.1: Major sources and typical pathways for ground and the surface water contamination by ECs. (Source: (Lapworth et al., 2012))

## 2.2. Advanced technologies for abatement of organic pollutants (OP) in water

In last few decades, several treatment technologies have been invented and developed to treat the organic pollutants in water system. These can be broadly categorized into two types: separation-based processes and degradation-based processes as shown in Figure 2.2. Separation based processes involves physical separation of contaminants from wastewater without any degradation. Such processes include adsorption, ion-exchange, coagulation-flocculation and membrane filtration. On the other hand, degradation-based processes involve biological, chemical, electrochemical and advanced oxidation processes where the complex contaminants are degraded

into simpler compounds or sometimes even into carbon dioxide and water. Due to the raising concern regarding the emerging organic contaminants because of their accumulation tendency into the soil, environment and aquatic system, a degradation-based process would be the ultimate solution to abate these contaminants. Therefore, recent efforts are being made to study the biological, chemical, electrochemical methods for the degradation and removal of emerging contaminants.

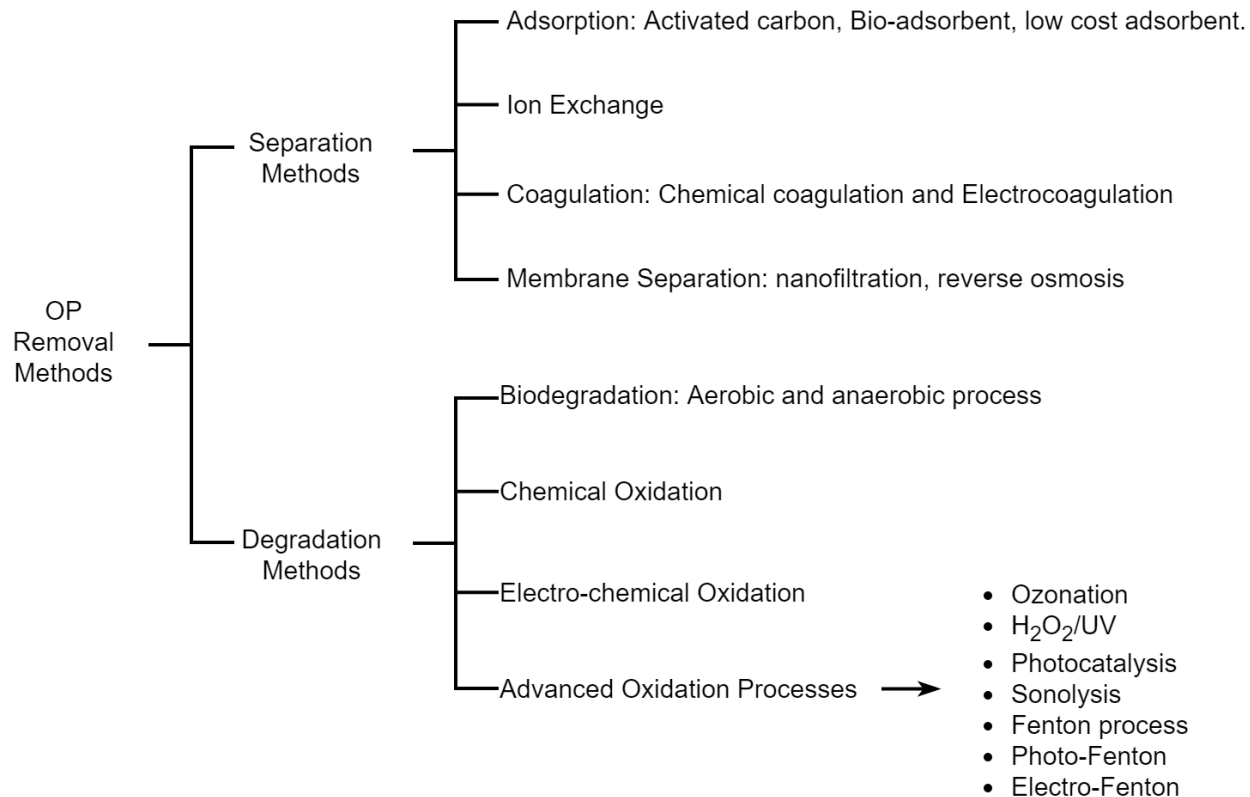


Figure 2.2: Organic Pollutant (OP) removal methods from wastewater.

Treatment of municipal and industrial wastewater is a complicated process and a single method is not enough to remove all types of contaminant from the wastewater due to the variation in their characteristics. Most of the current wastewater treatment plant comprises of primary clarification followed by biological process, secondary clarification, advanced processes such as adsorption on activated carbon, membrane filtration and UV/ozone disinfection. Biological process involves the action of micro-organisms either in aerobic condition or in anaerobic condition for the degradation of organic pollutants. It is one of the widely used process to treat the domestic or municipal

wastewater. However, for industrial water treatment it cannot be applied due to the biomass poisoning by different chemicals (Alok D. Bokare and Choi, 2014).

Adsorption process is widely studied for the removal of organic micropollutants due to simpler design, ease of operation, low investment cost and environmentally benign. Till now several adsorbent materials have been developed and studied for adsorption of ECs. Sophia and Lima reviewed the adsorption of ECs by different adsorbent materials including activated carbon, graphene and carbon nanotubes, modified biochar and composite adsorbents (Sophia A. and Lima, 2018). However, adsorption is unable to degrade the micropollutant and thereby it remains in the regeneration effluent which may need further treatment prior to discharge into the environment.

Membrane processes such as ultrafiltration (UF), nanofiltration (NF), forward osmosis (FO) and reverse osmosis (RO) have been widely studied for the separation of ECs from water and wastewater. Transport and separation of ECs by membranes are significantly affected by the Types of membranes, as well as the wastewater conditions and properties of ECs. Rodriguez-Narvaez et al. reported that, highly water soluble and polar ECs are easily separable than low water soluble and non-polar compounds by UF membrane (Rodriguez-Narvaez et al., 2017). NF has higher potential and removal efficiency in some ECs than the UF. Acero et al. reported the caffeine removal efficiency by UF was in the range of 2-21%, whereas 46-84% removal efficiency was obtained for NF (Acero et al., 2010). FO and RO process uses a semi-permeable membrane to separate the dissolved contaminants from water, however the driving forces for separation are different. In the FO process a concentrated draw solution is used to create an osmotic pressure gradient across the membrane. As a result, water permeates from the feed solution to the concentrated draw solution. While the RO process uses a hydraulic pressure gradient as a driving force to transport water across the membrane. It has been reported that the removal efficiency of ECs by different types of membranes declined in the following order:  $RO \geq FO > NF > UF$  (Kim et al., 2018).

### **2.3. Advanced oxidation process**

Advanced Oxidation Processes (AOPs) are gaining much popularity in present-days due to their effectiveness in the elimination of various organic pollutants from the wastewater. AOP involves the application of various oxidizing agents including ozone ( $O_3$ ), hydrogen peroxide ( $H_2O_2$ ) or

heterogeneous catalysts, e.g.  $\text{TiO}_2$ , Fe, in the presence or absence of an irradiation source for *on-site* production of highly reactive radicals, particularly the hydroxyl ( $\bullet\text{OH}$ ) radicals, that control the degradation mechanism of various hazardous pollutants (Al-Anazi et al., 2018; Sirés et al., 2014). Hydroxyl ( $\bullet\text{OH}$ ) radical can be characterized as the second most dominant oxidizing agent (next to fluorine) having a redox potential of  $E^\circ (\bullet\text{OH}/\text{H}_2\text{O}) = +2.8 \text{ V/SHE}$  which can react with the organic pollutants at a rate constant of  $10^8\text{--}10^{11} \text{ M}^{-1} \text{ s}^{-1}$ . Compare to other free radicals it is non-selective in reacting with many organic pollutants and can be produced at ambient temperature and pressure. Once generated,  $\bullet\text{OH}$  radicals can readily react with the complex organic contaminants and neutralize them to  $\text{CO}_2$  and water through a series of chain reactions (Sillanpää et al., 2018). Till now several AOP methods have been developed and applied efficiently in wastewater treatment. Table 2.2 summarizes the principle AOP methods with their corresponding reactions for the generation of free radicals.

Table 2.2: AOPs with corresponding reactions for the production of reactive free-radicals (Alok D Bokare and Choi, 2014; Hu and Long, 2016; Sirés et al., 2014)

AOP methods	Reactions
Ozonation	$3\text{O}_3 + \text{OH}^- + \text{H}^+ \rightarrow 2\text{HO}^\bullet + 4\text{O}_2$
$\text{O}_3/\text{H}_2\text{O}_2$	$2\text{O}_3 + \text{H}_2\text{O}_2 \rightarrow 2\text{HO}^\bullet + 3\text{O}_2$
$\text{O}_3/\text{UV}$	$\text{O}_3 + \text{H}_2\text{O} + h\nu \rightarrow \text{O}_2 + \text{H}_2\text{O}_2$
$\text{H}_2\text{O}_2/\text{UV}$	$\text{H}_2\text{O}_2 + h\nu \rightarrow 2\text{HO}^\bullet$
Ultrasound (US)/ $\text{O}_3$	$\text{O}_3 + \text{H}_2\text{O} + \text{US} \rightarrow \text{O}_2(\text{g}) + 2\text{HO}^\bullet$
US/ $\text{H}_2\text{O}_2$	$\text{H}_2\text{O}_2 + \text{US} \rightarrow 2\text{HO}^\bullet$
Fenton	$\text{Fe}^{2+} + \text{H}_2\text{O}_2 \rightarrow \text{Fe}^{3+} + \text{HO}^\bullet + \text{OH}^-$
Photo-Fenton	$\text{Fe}^{2+} + \text{H}_2\text{O}_2 + h\nu \rightarrow \text{Fe}^{3+} + \text{HO}^\bullet + \text{OH}^-$ $\text{Fe}(\text{OH})^{2+} + h\nu \rightarrow \text{Fe}^{2+} + \text{HO}^\bullet$ $\text{Fe}(\text{OOCR})^{2+} + h\nu \rightarrow \text{Fe}^{2+} + \text{CO}_2 + \text{R}^\bullet$
Heterogeneous photocatalysis ( $\text{TiO}_2/\text{UV}$ )	$\text{TiO}_2 + h\nu \rightarrow \text{TiO}_2(e^- + h^+)$ $h^+ + \text{H}_2\text{O} \rightarrow \text{HO}^\bullet + \text{H}^+$ $e^- + \text{O}_2 \rightarrow \text{O}_2^{\bullet-}$
Heterogeneous sulfate radical based AOP	$\text{CoOH}^+ + \text{HSO}_5^- \rightarrow \text{CoO}^+ + \text{SO}_4^{\bullet-} + \text{H}_2\text{O}$

### 3. PHOTOCATALYSIS

The term ‘Photocatalysis’ implies the combined action of light and catalysts to bring about a chemical reaction or to accelerating the reaction kinetics (Ohtani, 2011). The materials that initiate the chemical reactions by absorbing the photon energy is known as photocatalysts. In a typical photocatalytic process, the photocatalyst doesn’t undergo any chemical conversion but acts as an active surface for the reaction. Photocatalysis is being considered to be the “green” and one of the effective advanced oxidation processes and used extensively in a variety of field including water treatment, air purification, energy application, self-cleaning and self-sterilizing surfaces (Pelaez et al., 2012).

#### 3.1. Fundamental mechanism of photocatalytic pollutant degradation

Photocatalytic degradation of the pollutant in the aqueous media takes place according to the following steps (Marschall, 2014; Pelaez et al., 2012):

1. Absorption of photon energy results the excitation of charge carriers (generation of electron and hole).
2. Diffusion of charge carrier to the catalysts surface.
3. Formation of reactive free radicals by redox reactions between the excited charge carrier and adsorbate molecules.
4. Interaction of free radicals with the pollutant at the catalysts surface.
5. Transformation of pollutant into CO<sub>2</sub> and H<sub>2</sub>O.

A schematic diagram representing the general semiconductor photocatalysis is depicted in Figure 3.1. As can be seen in Figure 3.1, when light of sufficient energy ( $>E_g$ ) interacts with catalysts, it excites an  $e^-$  from the VB to the CB, subsequently a hole is generated in the VB. This process can be expressed by Eq. (3.1):



For photoexcitation, it must be noted that, the energy of the light needed to be greater than the band gap energy of the catalyst material. If we consider anatase TiO<sub>2</sub> ( $E_g = 3.2$  eV), as an example, then to overcome the band gap energy the wavelength of the light should be  $\leq 387$  nm.

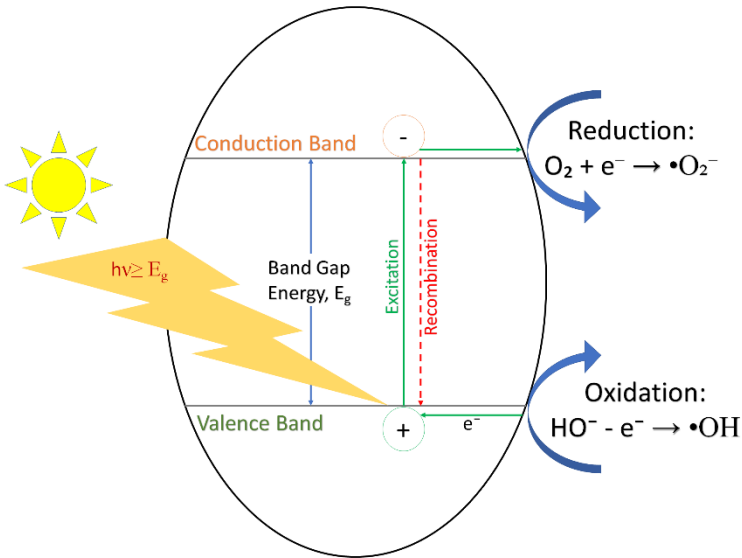
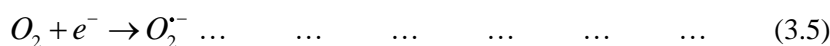


Figure 3.1: Schematic of the Photocatalytic Process (Pelaez et al., 2012).

Photogenerated electrons and holes are then either get recombined by dissipating energy (Eq. 3.2) or starts to migrate from inside to the catalysts surface and get trapped on the surface. Trapped electrons and holes can immediately participate in redox reactions. For example, the positively charged hole on the valance band can oxidize water or  $\text{OH}^-$  adsorbed at the catalyst surface to produce highly oxidative  $\bullet\text{OH}$  radicals (Eq. 3.3). On the other hand, excited electrons on the conduction band is entrapped by an electron acceptor (e.g., dissolved oxygen) and leads to the generation of superoxide radicals (Eq. 3.5). The superoxide radicals then further transform into hydroperoxyl radical by accepting a proton (Eq. 3.6) and may be reduced to  $\text{H}_2\text{O}_2$  (Eq. 3.9) as well.



The degradation process of organic pollutants initiates immediately on the surface of catalysts after the production of  $\bullet\text{OH}$  radicals and the active oxygen species.  $\bullet\text{OH}$  radicals reduce the organic pollutant to carbon dioxide and water (Eq. 3.4), while some pollutants are oxidized by reactive oxygen species (Eq. 3.7 & 3.8). It must be noted that, the dissolved oxygen in the aqueous media is the key element that initiates the reactions during the photocatalytic process.

### 3.2. Advanced materials in photocatalytic water treatment

Development of a model photocatalytic material with all the desired properties is a challenging task and efforts are being made regarding their development. Till now several materials has been developed including binary and ternary compounds. The binary materials include metal oxide, metal sulfide and carbon-based non-metal material. Some of them have very promising photocatalytic activity. This section mainly illustrates the structural and photocatalytic characteristics of those compounds.

In photocatalytic application  $\text{TiO}_2$  is one of the most promising material and used extensively in a variety of application including water and air purification, hydrogen evolution, carbon dioxide conversion, dye-sensitized solar cell and self-cleaning surfaces.  $\text{TiO}_2$  is basically an n-type semiconductor material due to the deficiency of oxygen. There are three different crystalline phases of  $\text{TiO}_2$  are known to exists: anatase, brookite and rutile. The bandgap energy for anatase, brookite and rutile is 3.2, 3.2 and 3.0 eV respectively (Hu et al., 2003). Besides  $\text{TiO}_2$  other metal oxide semiconductors have been studied by several researchers for photocatalytic applications such as  $\text{ZrO}_2$ ,  $\text{CeO}_2$ ,  $\text{SnO}_2$ ,  $\text{ZnO}$ ,  $\text{CuO}$ ,  $\text{WO}_3$  etc. Principle characteristics of these materials with their application field is listed in Table 3.1.

Table 3.1: Principle characteristics of some promising photocatalytic materials.

Material	Type	$E_g$ , (eV)	Characteristics	Reference
$\text{TiO}_2$	n	3.0-3.2	There are three different crystalline phases of $\text{TiO}_2$ are known to exists: anatase, brookite and rutile. Rutile is the most stable phase while anatase and brookite are metastable which transforms into rutile if calcinated beyond $600^\circ\text{C}$ .	(Hu et al., 2003; Linsebigler et al., 1995)

Material	Type	$E_g$ , (eV)	Characteristics	Reference
ZrO <sub>2</sub>	n	~5.0	Due to wide bandgap it exhibits photocatalytic activity under UV light region. Apart from water treatment it is used in hydrogen generation, fuel cell electrolytes due to position of conduction band minimum at high energy level.	(Reddy et al., 2018; Wang et al., 2016)
CeO <sub>2</sub>	n	3.37	High thermal stability, better UV light absorption ability with high reactivity. Also used in fuel cells, sensors, oxygen storage, electrochemical devices, biological applications and solar cell.	(Bakkiyaraj et al., 2016)
SnO <sub>2</sub>	n	3.6	Rutile structure is widely studied due to high surface area, good chemical and thermal stability, high electrical conductivity. Besides water treatment application it is used in sanitary disinfection and sensing devices.	(Al-Hamdi, 2017)
ZnO	n	3.2-3.7	Three crystal structures: rocksalt, wurtzite and cubic. Hexagonal wurtzite is the most stable at ambient temperature and pressure. It has strong oxidation ability and good optical property. Apart from water treatment it is used in cosmetics, paints, ceramics, rubber and fertilizer industries. Photo-corrosion is reported as a major drawback.	(An et al., 2008; Lee et al., 2016)
CuO	p	1.2	Inexpensive, non-toxic and high stability. Nanostructured CuO is used in many applications such as heterogeneous catalysis, battery, sensors, super capacitors due to high specific surface area and good electrochemical activity.	(Murugesan et al., 2018)

Material	Type	$E_g$ , (eV)	Characteristics	Reference
PbO	-	2.2-2.6	Temperature dependent two polymorphs are available: Red tetragonal phase ( $\alpha$ -PbO) and yellow orthorhombic phase ( $\beta$ -PbO). $\alpha$ -PbO undergoes a phase transition to $\beta$ -PbO at atmospheric pressure and 489°C. It is effectively used in a variety of application including fabrication of nanodevices, sensor, electrodes in batteries, efficient and reusable catalysts.	(Borhade et al., 2013; Hai et al., 2013)
WO <sub>3</sub>	n	2.6-2.8	Four crystal structures depend on the temperature: tetragonal, orthorhombic, monoclinic and triclinic. Monoclinic is the most available phase due to its stability at room temperature. Moreover, it offers chemically stability, robustness to photocorrosion, and W exists in 2+, 3+, 4+, 5+, and 6+ oxidation states which facilitates it to store photogenerated electrons.	(Lassner and Schubert, 1999; Praus et al., 2017)
ZnS	n	3.7-3.8	Two different crystalline forms: cubic and hexagonal, at low temperature cubic form is more stable, good electronic mobility and thermal stability, water insoluble.	(Lee and Wu, 2017)
CdS	-	2.42	Two crystal forms same as ZnS: cubic and hexagonal. Due to low bandgap it is widely studied for hydrogen generation. However, high recombination rate and photo-corrosion are the major drawbacks regarding its application.	(Wei et al., 2018)
g-C <sub>3</sub> N <sub>4</sub>	n	2.7	Sustainable polymeric organic and metal free semiconductor with amazing electronic structure, inexpensive and high	(Liu et al., 2018; Tan et al., 2018)

Material	Type	$E_g$ , (eV)	Characteristics	Reference
$\text{Bi}_2\text{O}_3$	-	2.8	thermochemical stability. However, low surface area, poor light absorption efficiency and lower charge carrier separation rate suppressed its photocatalytic activity.	(Jiang et al., 2018; Medina et al., 2018)
$\text{Sb}_2\text{O}_3$	n	3.0	Among the six different crystalline phase $\alpha$ - $\text{Bi}_2\text{O}_3$ is the most stable phase at room temperature. Photogenerated hole has the strong oxidative capability due to its energy level position therefore great possibility of $\bullet\text{OH}$ radical formation and better pollutant degradation efficiency. However, rapid charge recombination rate decreases the photocatalytic efficiency.	(He et al., 2013; Wang et al., 2017)
$\text{Fe}_2\text{O}_3$	n	2.2	It is widely used in glasses, sensors, fire retardants, catalysis and anode material in batteries. Due to long term stability, reproducibility and low cost it is used as a coupling component in photocatalysis. It has three different polymorphs $\alpha$ , $\beta$ and $\gamma$ - $\text{Sb}_2\text{O}_3$ . $\alpha$ - $\text{Sb}_2\text{O}_3$ exists at low temperature as orthorhombic phase while two others exist at higher temperature.s	(Domingo et al., 2018; Xia et al., 2013)
			It can be found in four different crystalline forms such as hematite ( $\alpha$ - $\text{Fe}_2\text{O}_3$ ), magnetite ( $\text{Fe}_3\text{O}_4$ ), maghemite ( $\gamma$ - $\text{Fe}_2\text{O}_3$ ) and wüstite ( $\text{FeO}$ ). $\alpha$ - $\text{Fe}_2\text{O}_3$ is the most stable and widely available in Nature. Due to its low bandgap and stability it is used in a variety of application from water treatment to energy capture.	

Material	Type	$E_g$ , (eV)	Characteristics	Reference
$\text{In}_2\text{O}_3$	n	3.6	Semiconductor with excellent conductivity and superior photoelectrochemical stability. Due to wide bandgap its visible light activity is very low. Apart from water treatment application it is used in solar cells, biosensors and gas sensors application.	(Gan et al., 2017; Pan et al., 2018)
$\text{BiFeO}_3$	-	2.1	Perovskite type rhombohedrally distorted material with high chemical stability and photocatalytic activity. Efficient charge carrier separation takes place due to ferroelectric properties which results better photocatalytic performance under visible light irradiation.	(Ahmad et al., 2017; Pattnaik et al., 2018)
$\text{Bi}_2\text{WO}_6$	n	2.7	Its band energy position facilitates $\bullet\text{OH}$ radical formation rather than $\bullet\text{O}_2^-$ radical therefore very much effective in organic pollutant degradation. However, higher recombination rate decreases its photocatalytic activity.	(Jonjana et al., 2018; Zhang and Ma, 2017a)
$\text{BiVO}_4$	-	2.3-2.4	It exists as three different crystal forms: monoclinic scheelite, tetragonal scheelite, and tetragonal zircon. Many researchers explored its application towards water splitting because of its location of conduction band. However, addition with electron scavenger it can degrade the organic micro-pollutants in visible light irradiation.	(Guo et al., 2010; Xie et al., 2006)
$\text{BiPO}_4$	-	3.85	It has three allotropes: low temperature monoclinic, high temperature monoclinic and hexagonal. It represents higher	(Maisang et al., 2017)

Material	Type	$E_g$ , (eV)	Characteristics	Reference
			photocatalytic activity than $TiO_2$ due to higher charge carrier separation resulted from electrostatic field generated by $PO_4$ tetrahedrons.	
$InVO_4$	p	2.0	Lower bandgap and suitable energy band position enabled wide application of the material including organic pollutants degradation, air purification, water splitting, gas sensor and so on.	(Hoon et al., 2012; Yan et al., 2012)
$Ag_3PO_4$	p	2.45	More than 90% quantum efficiency has been reported as a visible light driven catalyst. However due to poor photostability and high cost its application has been limited. Recently several composite catalysts are being developed using this compound.	(Chi et al., 2018; Guo et al., 2018)
$Ag_3VO_4$	n	$\sim 2$ eV	Due to the narrow bandgap it is one of promising visible light driven photocatalyst. However, due to higher charge carrier recombination rate its application has increased in composite catalysis.	(Zhang and Ma, 2017a, 2017b)

### 3.3. Strategies for improved photocatalytic performance

Development of new photocatalytic material is a challenging field of research and significant efforts are being made since the last decades. For a successful photocatalytic operation both kinetic and thermodynamic requirements must be satisfied. The kinetic process is discussed in the earlier 3.1 section. The key challenges in the kinetic process development is the reduction of charge carrier reunification which takes place in the range of nanoseconds. Several strategies can be adopted to enhance the kinetic properties of the photocatalytic processes such as development of

highly efficient charge transport nanostructures, creating high quality heterojunction interfaces and development of highly reactive surfaces and co-catalysts.

On the other hand, thermodynamic properties include the minimum required band gap energy for photoexcitation, position of the valence and conduction band and their corresponding overpotential for the redox reactions (Li et al., 2018). For example, semiconductor with higher VB labels are suitable for water oxidation reaction (WOR) and therefore can be used in photocatalytic dye degradation and other water treatment application. Whereas semiconductors with higher CB position is effective for carbon dioxide reduction reaction (CRR) and hydrogen evolution reaction (HER). A schematic of thermodynamic requirements for a photocatalytic reaction is illustrated in Figure 3.2. For improvement of the thermodynamic properties of photocatalysts the key strategies include the development of wide spectrum responsive photocatalysts and composition engineering like doping and defect reduction (Li et al., 2016).

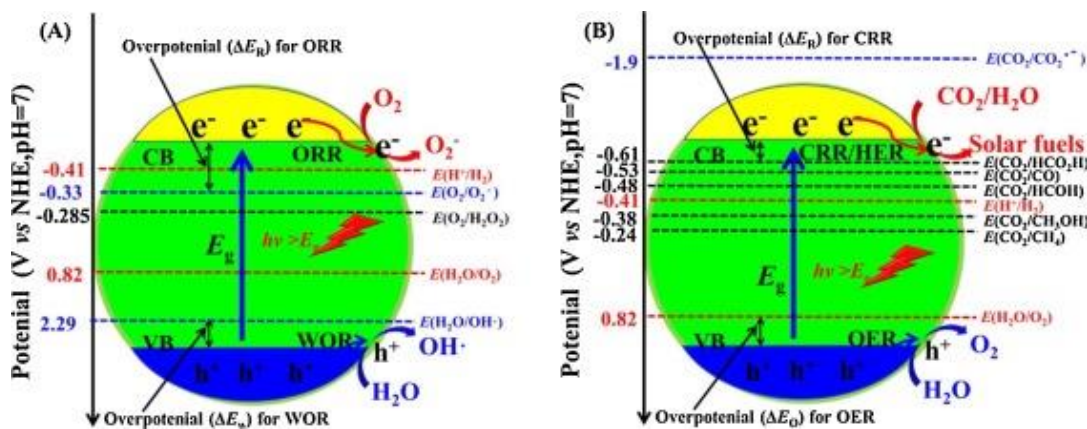


Figure 3.2: Thermodynamic requirements for water treatment (A) and solar fuel production (B) (Li et al., 2018).

It must be noted that, semiconductors with higher valence band level exhibits higher oxidation potential and therefore suitable for water oxidation reaction to produce  $\bullet\text{OH}$  radicals and the pollutant degradation as well. Different strategies for the development of photocatalytic material are explained in the following sub-sections.

### 3.3.1. Bandgap engineering

Band structure engineering is an effective approach to the improvement of photocatalytic activity of semiconductor material as the bandgap configuration significantly affects the photon absorption

efficiency, formation of electron-hole pairs and capabilities of redox reactions by excited charge carriers. Therefore, in recent years tremendous efforts were made in the bandgap engineering by many researchers around the world. Bandgap modification can be performed either by altering the valence band or conduction band position by incorporating the additional components into the base structure. Band gap engineering is usually made by doping with impurities such as the alkali metals, transition metals (e.g. Cr, Fe, Co, Ni, Zn), noble metals (e.g. Ag, Au, Pt, Pd) and non-metal elements (e.g. N, C, S, F).

Band gap modification by doping with the alkali or alkaline-earth metals including Li, Na, Ca, Sr, Ba etc. has been reported by many researchers (Sato et al., 2002, 2003; Jiang Yin et al., 2003; Zhang et al., 2007). In that case radius of the metal ion influences the cut in band gap energy. For example, Yin et al. reported that the band gap energy of  $\text{MC}_{0.1/3}\text{Nb}_{2/3}\text{O}_3$  (M = Ca, Sr and Ba) reduced from 2.77 to 2.27 eV when Ba was incorporated instead of Ca (J Yin et al., 2003).

In many studies it has been testified that the assimilation of transition metal into the  $\text{TiO}_2$  structures may lead to the establishment of new energy levels between the VB and CB; thereby, significantly reduces the band gap energy and improved the visible light absorption range (Dvoranova et al., 2002; Fuerte et al., 2001; Li and Li, 2002, 2001; Li et al., 2010; Lin et al., 2005; Seabra et al., 2011; Wu and Chen, 2004). However, some limitations such as role of transition metal as recombination sites for charge carriers and photo-corrosion has also been reported (Demeestere et al., 2005).

Visible light response of metal oxide semiconductors can also be enhanced by doping with noble metals (Behar and Rabani, 2006; Cihlar et al., 2013; Ishibai et al., 2007; Li and Li, 2001; Xiong et al., 2015; Zeng et al., 2007). Incorporation of noble metal significantly reduces the recombination rate of charge carriers by creating more electron trap and promoting the interfacial charge transfer.

Non-metal elements doping is also an auspicious technique to enhance the visible light activity of semiconductor materials. Among the various non-metal dopants, nitrogen is the most promising one due to its high stability, lower ionization energy and comparable atomic dimensions with oxygen. Visible light response of N-doped  $\text{TiO}_2$  was first explored by Asahi and his co-workers (Asahi et al., 2001). They produced N-doped  $\text{TiO}_2$  via sputter deposition technique under  $\text{N}_2/\text{Ar}$  atmosphere. After that, substantial efforts are being made by many researchers to understanding

the fundamental mechanisms for improved photocatalytic efficiency of N-doped TiO<sub>2</sub> by studying its electronic, optical and structural properties (Chen and Mao, 2007; Serpone, 2006; Zhu et al., 2009). Also, other non-metals such as C, P and S significantly contribute in band gap narrowing by changing the lattice parameters and creating the trapping states within the valence and conduction bands from electronic disorder (Ohno et al., 2003; Shen et al., 2006; Yang et al., 2007).

### 3.3.2. Morphological Improvement

Morphology and surface chemistry of the semiconductor material plays a vital role in the transfer of charge carrier at the catalyst surface, selectivity, redox potential and exposure towards photo-corrosion. In several research it was shown that the morphological properties are strongly reliant on the crystallinity and architecture of the particles (He et al., 2012; Shang et al., 2008; Zhang and Zhu, 2012). Crystallinity of the material can be improved by reducing the defect concentration which in turn reduces the electron-hole recombination sites. Also, the particle size favors the charge carrier migration to the catalysts surface by reducing the diffusion resistance. However, expansion of band gap was reported if the radius of particles becomes less than the Bohr radius.

Crystal facets also said to be play a substantial role in photocatalytic reactions. In a report, Yang et al. showed that the [001] facet is more reactive than [101] facet in anatase TiO<sub>2</sub> (Yang et al., 2008).

### 3.3.3. Dye sensitization

Photosensitization properties of dyes can be used as an effective approach to modify the photo sensitive characteristics of semiconductor material such as improvement of visible light response of TiO<sub>2</sub> (Chatterjee and Mahata, 2001; Moon et al., 2003). The fundamental mechanism lies behind the dye sensitization is the excitation of electron from HOMO (highest occupied molecular orbital) to the LUMO (lowest unoccupied molecular orbital) resulted from the absorption of light in the visible range. The photoexcited electron subsequently moves to the CB of TiO<sub>2</sub> and participate in the reduction reaction at the titania surface to produce superoxide radical ( $\bullet\text{O}_2^-$ ) and hydrogen peroxide radical ( $\bullet\text{OOH}$ ), while the VB of TiO<sub>2</sub> remains unaffected (Figure 3.3). The photoactive radicals then participate to degrade the organic substances and mineralize then to CO<sub>2</sub> and H<sub>2</sub>O. In this process it must be noted that, the LUMO of dye molecules must have more negative potential than the CB of TiO<sub>2</sub> (Pelaez et al., 2012; Rehman et al., 2009).

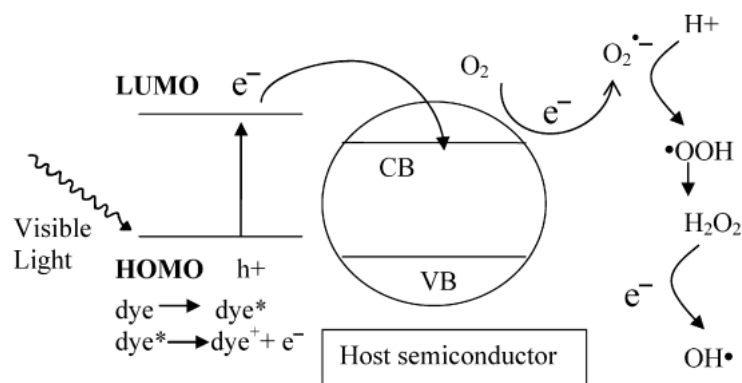


Figure 3.3: Improvement of photocatalytic process by dye sensitization process (Rehman et al., 2009).

### 3.3.4. Composite semiconductors

Composite catalysts, by combining two or more catalysts, are also considered as a promising approach to advance the photo response of catalysts towards the range of visible light. They not only recompense the shortcomings of individual materials, but also establish a synergistic outcome such as improved charge separation and photostability (Marci et al., 2001; Marschall, 2014). Composite catalysts can be two types, namely, multicomponent and multiphase heterojunction. When two different types of materials are combined to prepare a composite, it is called the multicomponent heterojunction whereas the later one consists of two different phases of same materials (Marschall, 2014).

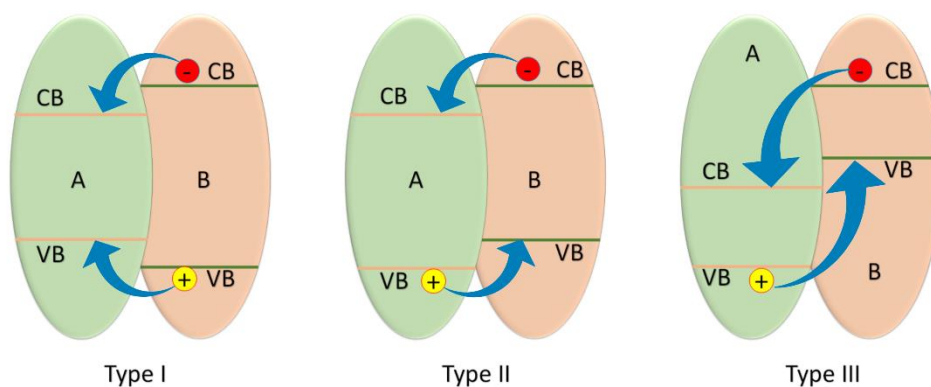


Figure 3.4: Different types of heterojunction composites (Marschall, 2014).

Multicomponent heterojunction semiconductor can be three types based on their band position as shown in Figure 3.4. When two semiconductors, namely A & B, are combined where the CB

position of A is lower than the CB position of B and VB position of A is higher than the VB position of B, both excited electron and hole are accumulated on the CB and VB of A respectively. In that case, higher recombination rate of charge carrier is observed which in turn reduces the photocatalytic efficiency of the composite materials. However, selective incorporation of co-catalysts within the composite system significantly improves the catalytic performance. A characteristic example of type I composite is  $\text{TiO}_2/\text{WO}_3/\text{Pt}$  (Srinivasan and Miyauchi, 2012).

Composites with type II heterojunction offers the effective charge carrier separation due to their relative band positions. Since holes and electrons are moved up and down respectively for gaining energy, photoexcited electrons shift from the CB of B to the CB of A and a simultaneous transformation of the holes from the VB of A to the VB of B takes place. As a result, an effective charge carrier separation is accomplished. A widely studied example of type II composite is the  $\text{CdS}/\text{TiO}_2$  system (Bai et al., 2010; Baker and Kamat, 2009). The bandgap energy of  $\text{CdS}$  and  $\text{TiO}_2$  are 2.4 and 3.2 eV, respectively. Therefore, under the visible light the electron-hole pair is created only from the excitation of  $\text{CdS}$  while  $\text{TiO}_2$  remains unaffected. The photoexcited  $e^-$  transfer to the CB of  $\text{TiO}_2$  due to the lower position of CB compared to  $\text{TiO}_2$ . On the other hand,  $h^+$  are accumulated on the VB of  $\text{CdS}$  rather than transferring due to the higher position of VB in  $\text{CdS}$  relative to  $\text{TiO}_2$ .

In type III composite, the band arrangements are such that, the CB position of semiconductor A is even lower than the VB position of semiconductor B. This type of band positioning is often called the broken-gap condition and hardly used to improve the photocatalytic efficiency. Charge carrier separation takes place as like type II composite (Marschall, 2014).

## 4. LITERATURE REVIEW

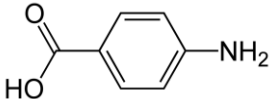
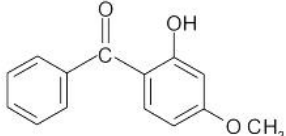
### 4.1. UV Filters

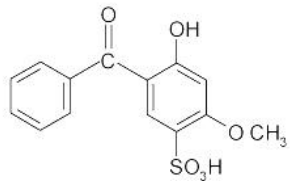
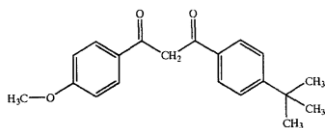
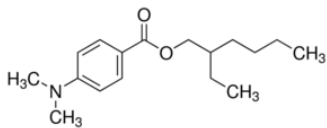
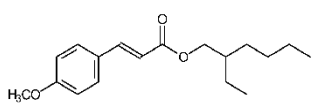
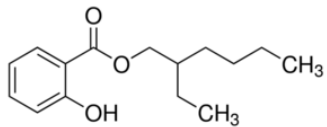
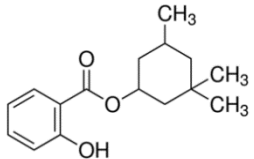
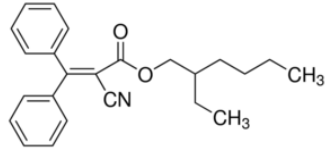
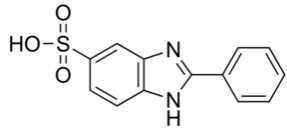
UV filters are the principal ingredients of personal care products such as sunscreen lotions, lipsticks, shampoo, hairspray or makeup and used as a UV stabilizer in different plastic products and paints. Their primary function is to absorb, reflect or scatter the UV radiations, UVA (320-400nm) and UVB (290-320nm), and protect the consumer's skin and products from the harmful effect of sunlight.

### 4.2. Organic UV filters and their characteristics

Two types of UV filters are available: inorganic and organic UV filters. Inorganic UV filters usually reflect or scatter the UV radiation whereas the organic one absorbs the UV radiation, mostly UVB (Serpone et al., 2007). There are two inorganic materials known to exist that acts as UV filters: Zinc oxide (ZnO) and Titanium dioxide (TiO<sub>2</sub>). On the other hand, number of organic UV filters are still unknown; the most common compounds are benzophenones, cinnamates, benzimidazoles, para-aminobenzoates, dibenzoylmethane, and camphor derivatives. Different countries around the world has different legislation for the approval and usage of these UV filters. There are approximate fifty-five UV filters permitted for use in personal care products worldwide. In Europe 27 UV filters are approved by European Union among which 10 compounds are uniformly approved (Santos et al., 2012). Table 4.1 represents some common UV filters with the physico-chemical characteristics.

Table 4.1: Molecular structure and physico-chemical properties of some commonly used UV filters

Name	Structure	Molecular wt. (g/mol)	Solubility in water @ 25°C	Log <i>K<sub>ow</sub></i>	$\lambda_{max}$ (nm)
<i>p</i> -amino benzoic acid (PABA)		137.14	915	0.83	282
Benzophenone-3 (BP-3)		228.24	0.21	3.79	290

Name	Structure	Molecular wt. (g/mol)	Solubility in water @ 25°C	Log $K_{ow}$	$\lambda_{max}$ (nm)
Benzophenone-4 (BP-4)		308.31	0.65	0.88	288
Butyl methoxy dibenzoyl methane (BMDM)		310.39	0.037	2.41	358
Ethyl-hexyl dimethyl PABA (EHPABA)		277.4	0.0021	6.15	310
Ethyl-hexyl methoxycinnamate (EHMC)		290.4	0.15	5.8	306
Ethyl-hexyl salicylate (EHS)		250.34	0.028	5.77	240
Homosalate (HS)		262.35	0.02	6.16	-
Octocrylene (OC)		361.49	0.0002	7.35	300
Phenyl benzimidazole sulfonic acid (PBSA)		274.3	0.26	0.01	300

### 4.3. Toxicological impact of UV filters in environment and aquatic life

UV filters enter the environment in two different way: direct and indirect way (Santos et al., 2012). Direct way means their direct exposure to the environment such as during bathing and swimming activities in the lake, beach, river and swimming pool. Also, it may come directly from the manufacturing industry. Indirect exposures are related to household wastewater discharges and

effluent from the wastewater treatment plant. For example, during showering and laundry, they mixed with water and then comes to the environment or wastewater treatment plant. In the water treatment plant, UV filters and their degradation products are usually accumulated in the sludge and finally comes to the environment during sludge disposal. Environmental existence of UV filter was first reported in 1982 when benzophenone (BP) was detected in the water of Baltic Sea (Ehrhardt et al., 1982).

UV filters primarily enter the pool water during the swimming and recreational activities from the swimmer's body. Recently, they are detected in the swimming pool water and surface water in different countries with different concentration levels (Table 4.2). Commonly detected compounds are Benzophenone-3 (BP-3), 4-methyl-benzylidene camphor (4-MBC), Octyl *p*-methoxycinnamate (OMC), Isoamyl methoxycinnamate (IMC), Octocrylene (OC), Octyl dimethyl-*p*-aminobenzoate (ODPABA), 2-phenyl-1H-benzimidazole-5-sulfonic acid (PBS).

Table 4.2: UV filters concentration in swimming pool water

Country	UV Filters and their concentrations, $\mu\text{g/L}$							References
	BP-3	4-MBC	OMC	IMC	OC	ODPABA	PBS	
Germany	1.2	0.6-10	1.8-7		7-25		2-16	(Zwiener et al., 2007)
Spain	< 0.11	< 0.2		< 0.7	< 3	< 0.07		(Vidal et al., 2010)
Slovenia	0.1-0.4	< 0.15-0.33			< 0.27			(Cuderman and Heath, 2007)
Greece	2.4-3.3					< 0.9-2		(Lambropoulou et al., 2002)

In several studies it has shown that, the UV filters may undergo some degradation in aqueous media under sunlight or chlorine environment (Gong et al., 2015; Santos et al., 2012). Photostability of the organic UV filters can be characterized from their aromatic structure with conjugated *pi*-bonds. Under high energetic UV radiation, one of the *pi*-electrons transfer from its ground-state to the next higher orbital (*pi*<sup>\*</sup>) and become excited. Under this circumstance, two possible phenomena may occur, (i) the excited UV molecule may degrade into photo inactive compounds or (ii) the excited *pi*-electron returns to its original ground state by emitting the absorbed light in a longer wavelength and thereby restore its original structure (Shaath, 1987;

Silvia Díaz-Cruz et al., 2008). However, many researchers suggested that, the water constituents such as dissolved organic compounds, alkalinity of the water, nitrogen and chlorine concentration may influence the photodegradation of the UV filters in the aquatic environment (Zhang et al., 2010; Serpone et al., 2002; Santos et al., 2012). Specially, in swimming pool and sea water excited UV filters may undergo some degradation by their interaction with the chlorinated media. The degradation by-products are even more poisonous than the parent compounds; which may penetrate on the human skin and accumulate in the aquatic environment.

Environmental concerns are arising regarding the UV filters due to their tendency to accumulate or concentrate in the aquatic and marine environments as well as in the food chain. In a study, Balmer et al. detected four UV filters – BP-3, OMC, 4-MBC and OC in the fish sample with concentration level of 123, 72, 166 and 25 ng/g respectively (Balmer et al., 2005). Also, the photodegradation of UV filters under natural sunlight, reported by many researchers, lead to the formation of undesirable and toxic photoproduct which may penetrate on the human skin and bioaccumulate in human urine, breast milk and human semen (Teo et al., 2015). In a very recent investigation on pregnant women, Krause et al. found several benzophenones in amniotic fluid, cord- and fetal blood (Krause et al., 2018). In other studies, experiment on animals, several UV filters are found to be act as endocrine disruptors with significant estrogenic and anti-thyroid effects (Schlumpf et al., 2004).

#### **4.4. Degradation of organic UV filters by AOPs**

Very few studies are reported on the application of AOPs for the elimination of UV filters from the wastewater. Table 4.3 summarizes the AOP processes used for the exclusion of UV filters from the wastewater. Both  $HO^\bullet$  and  $SO_4^{\bullet-}$  radical based AOPs were studied by different researchers. The efficiency of an AOP process mainly relies on the formation of the free radicals. One major advantages of the AOPs are that it does not require extreme temperature and pressure to generate highly reactive free radicals which are expected to mineralize the complex organic pollutants completely.

Hydroxyl radicals ( $HO^\bullet$ ) are one of the most influential oxidizing agents known. Reaction mechanism of  $HO^\bullet$  radicals to organic contaminants can be described by three following steps: (i) electrophilic addition of  $HO^\bullet$  radicals to the aromatic rings (ii) Generation of carbon-centered

radicals by the abstraction of hydrogen atom and (iii) oxidation reaction where electron gaining of hydroxyl radicals from the organic pollutants takes place (Sillanpää et al., 2018). Table 4.3 summarizes the application of AOPs for the degradation of UV filters in recent years.

Table 4.3: Summary of AOP methods used for UV filter degradation.

AOP Methods	UV Filter	Experimental Conditions	Major Findings	Ref.
TiO <sub>2</sub> /H <sub>2</sub> O <sub>2</sub>	BP-3	Initial pollutant conc.- 1 mg/L, pH-9.0, TiO <sub>2</sub> conc.-1.184 g/L, H <sub>2</sub> O <sub>2</sub> conc.-128.069 mg/L	<ul style="list-style-type: none"> <li>- Complete removal of BP-3 was obtained in 45 min of reaction.</li> <li>- Almost 67% of TOC was removed in 300 min.</li> <li>- Overall ten degradation by-products were identified.</li> </ul>	(Henry Zúñiga-Benítez et al., 2016a)
Ultrasound/O <sub>3</sub>	BP-3	Initial BP-3 conc. - 3.9 mg/L, pH - 6.5, Power - 55.9 W, Frequency - 20kHz, Temp. - 25 ± 2°C	<ul style="list-style-type: none"> <li>- Ultrasound with ozonation completely removes the BP-3 in 50 min</li> <li>- This process removes more than 80% TOC.</li> </ul>	(H Zúñiga-Benítez et al., 2016)
TiO <sub>2</sub> /H <sub>2</sub> O <sub>2</sub> /UV	PBSA BP-3 BP-4	UV filter conc.- 0.04µM, H <sub>2</sub> O <sub>2</sub> conc.- 0.59mM, pH - 7, reaction time - 6 min, light intensity - 6W, monolithic structures of catalysts coated with 3 layers of TiO <sub>2</sub> .	<ul style="list-style-type: none"> <li>- Removal efficiency is 65%</li> <li>- Complete removal</li> <li>- Complete removal</li> </ul>	(Celeiro et al., 2018)
Photo-Fenton	BP-3	Initial BP-3 conc.- 1.0 ppm, pH- 3.0, Fe <sup>2+</sup> - 168 mg/L, H <sub>2</sub> O <sub>2</sub> conc. - 3449.29 mg/L, Temp. - 35 ± 2°C, irradiance- 350 W/m <sup>2</sup>	<ul style="list-style-type: none"> <li>- Complete removal of BP-3 after 60 min of operation</li> <li>- Photo-Fenton process was more effective than the Fenton process.</li> <li>- More than 60% of organic carbon were mineralized after 300 min of treatment.</li> </ul>	(Henry Zúñiga-Benítez et al., 2016b)

AOP Methods	UV Filter	Experimental Conditions	Major Findings	Ref.
O <sub>3</sub> electrolysis	Octocrylene (OC)	Inlet ozone conc. - 26.1 ppm, Cathodic current density - 26.4 mA/cm <sup>2</sup> , Initial pH = 10.	- 87.2% removal of OC was achieved within 5 min.	(Wu et al., 2017)
Cobalt ferrite peroxymonosulfate (PMS) system	PBSA	Initial PMS conc.- 0.1mM, Catalyst dose - 0.08 g/L, Initial PBSA conc.- 4 μM, pH = 6.75	- SO <sub>4</sub> <sup>•-</sup> and •OH radicals were generated and took part in the degradation of PBSA. - 75% removal of PBSA was observed after 240 min of reaction. - TOC removal was 32%. - Fifteen degradation byproducts were identified.	(Al-Anazi et al., 2018)
Co-doped carbon nanotube-PMS system	BP-4	Initial conc. of pollutant - 10 mg/L, Initial pH - 7, Catalyst dose - 100 mg/L, PMS conc. - 1.0 g/L, Temp.- 25°C	- Complete elimination of BP-4 within 30 min of reaction. - The reaction followed pseudo-first order kinetics and the corresponding rate constant was 0.1617 min <sup>-1</sup> . - TOC removal was 20% after 30 min of reaction. - Total 7 intermediate degradation product was detected.	(Liu et al., 2016)

## 5. MATERIALS AND METHODS

### 5.1. Chemicals

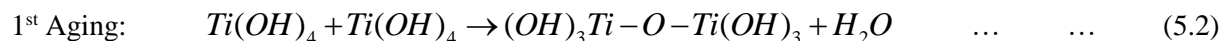
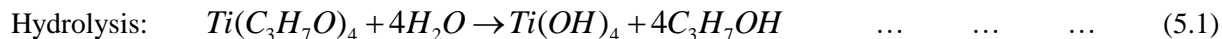
Analytical grade Lead (II) nitrate, Titanium (IV) butoxide, Antimony (III) chloride, Titanium (IV) isopropoxide, Triethanolamine, Benzophenone-3 (BP-3) were procured from the Sigma-Aldrich. All the solutions were prepared using deionized water (18.2 M $\Omega$ ) produced from a Milli-Q water purification system. Methanol, ethanol and acetonitrile used in the experiments were HPLC grade and purchased from Sigma-Aldrich. For pH adjustment sodium hydroxide, potassium hydroxide and 25% ammonia solution were used.

### 5.2. Catalyst synthesis methods

#### 5.2.1. Synthesis of TiO<sub>2</sub>

Nanostructured TiO<sub>2</sub> were synthesized by sol-gel method from titanium isopropoxide (TIPO) precursor according to the guideline provided by Lee et al. (Lee et al., 2010). Initially, calculated amount of TIPO and triethanolamine (TEA) was taken in a 500 ml conical flask and set it on a magnetic stirrer. Stirring speed was set as 500 rpm. The ratio of TIPO to TEA was kept as 1:2. Finally, the concentration of stock solution was settled as 0.5M Ti<sup>4+</sup> by adding doubly distilled water.

After that, 50 ml of stock solution was taken in a screw-caped Pyrex bottle and same amount of water was added with it. The mixed solution was then kept in an oven at 100°C for 24 hours after maintaining its pH (using NaOH or HClO<sub>4</sub>) as ~9.6 for gel formation. This step is called first aging step. After the first aging period, the resulting gel was transferred into an autoclave for second aging. The second aging period was 72 h long and the temperature was maintained as 140°C during the period. After the second aging period the gel was transferred into sol in which titania nanoparticles were dispersed. The sol was then washed with NaOH solution, dil. HNO<sub>3</sub> solution and distilled water and centrifuged to separate the nanoparticles from the residual dissolved components. The nanoparticles were then dried in an oven at 80°C for 24 h to take out the residual water. After that, the dried powder was calcinated at 500°C for better crystallinity. The following reactions takes place during this sol-gel process (Kashyout et al., 2010).



### 5.2.2. Synthesis of PbO/TiO<sub>2</sub>

For the synthesis of PbO/TiO<sub>2</sub> composite, a hydrothermal method was adopted according to the guideline provided by (Cheng and Zhao, 1994). Starting material for the synthesis was Lead nitrate (Pb(NO<sub>3</sub>)<sub>2</sub>) and titanium butoxide (Ti[O(CH<sub>2</sub>)<sub>3</sub>CH<sub>3</sub>]<sub>4</sub>). Initially, the precursor solution was prepared by dissolving titanium butoxide into ethanol and lead nitrate into water, named solution A and B respectively. Amount of Ti(OBu)<sub>4</sub> and Pb(NO<sub>3</sub>)<sub>2</sub> was calculated by maintaining a molar ratio of PbO/TiO<sub>2</sub> from 0.5 to 2. After that, Solution B was mixed with solution A under vigorous stirring and the pH of the solution was maintained at 13-14 by adding 5M KOH solution. The final solution was then sonicated for 10 min and shifted into a Teflon-lined stainless-steel autoclave for hydrothermal treatment. The hydrothermal reactions took place at a temperature of 160°C for 2 h. After the completion of hydrothermal treatment, the autoclave apparatus was cooled down to ambient temperature and the white precipitate was isolated by centrifugal action. The final product was then washed with deionized water until a neutral pH was obtained, dried at 80°C for 24h and then calcinated at 500°C for 1h. Complete synthesis process is presented in the Figure 5.1 and required amount of Lead nitrate and titanium butoxide for different molar ratio are given in Table 5.1.

Reactions:

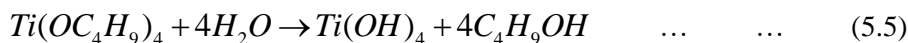
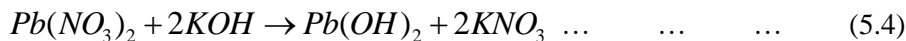
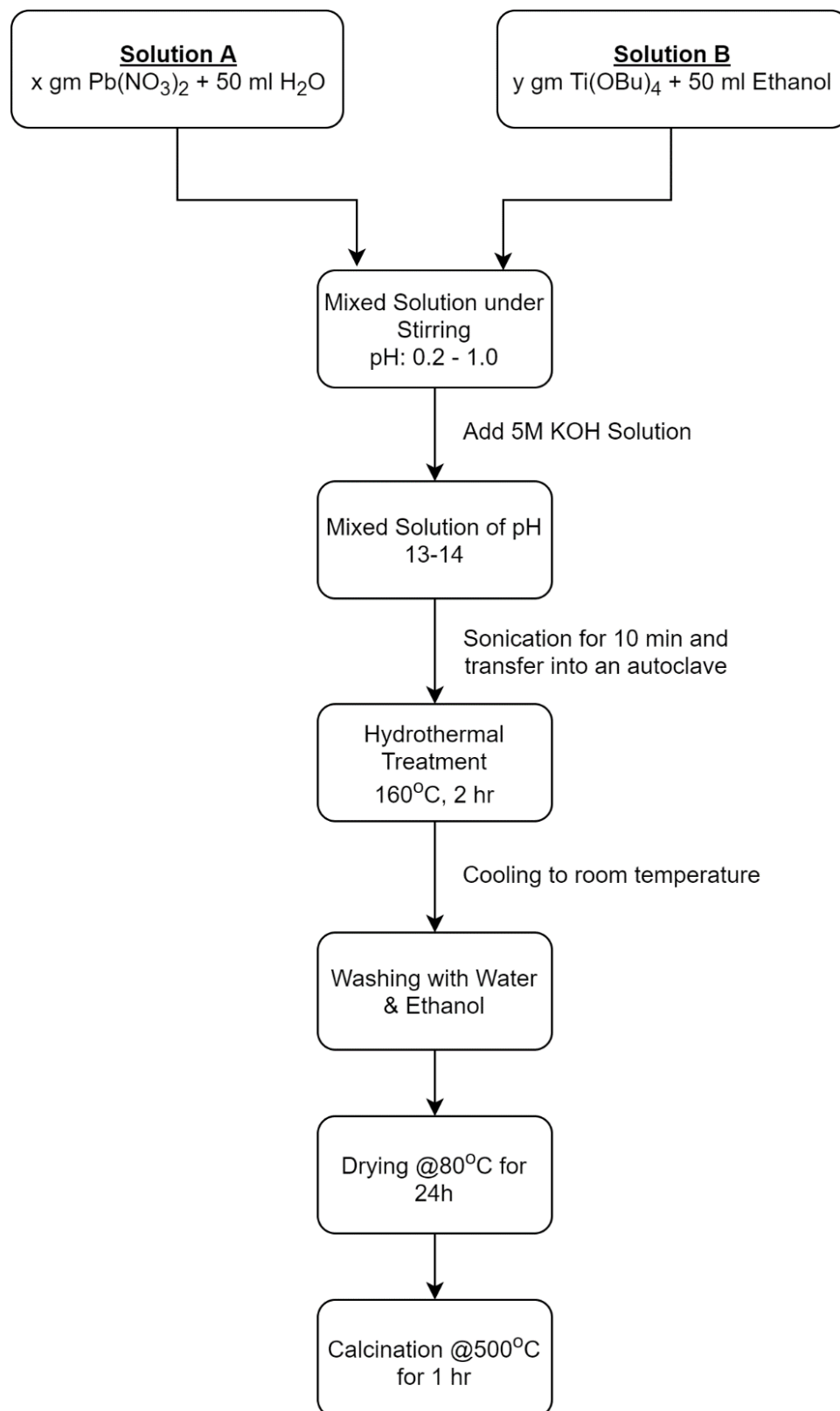


Table 5.1: Required amount of lead nitrate and titanium butoxide for synthesis

Molar ratio of PbO to TiO <sub>2</sub>	Lead nitrate, gm	Titanium butoxide, ml
0.5	6.22	12.81
1	8.29	8.54
2	9.95	5.12

Figure 5.1: Synthesis process of PbO/TiO<sub>2</sub> nanocatalysts.

### 5.2.3. Synthesis of Sb<sub>2</sub>O<sub>3</sub>/TiO<sub>2</sub>

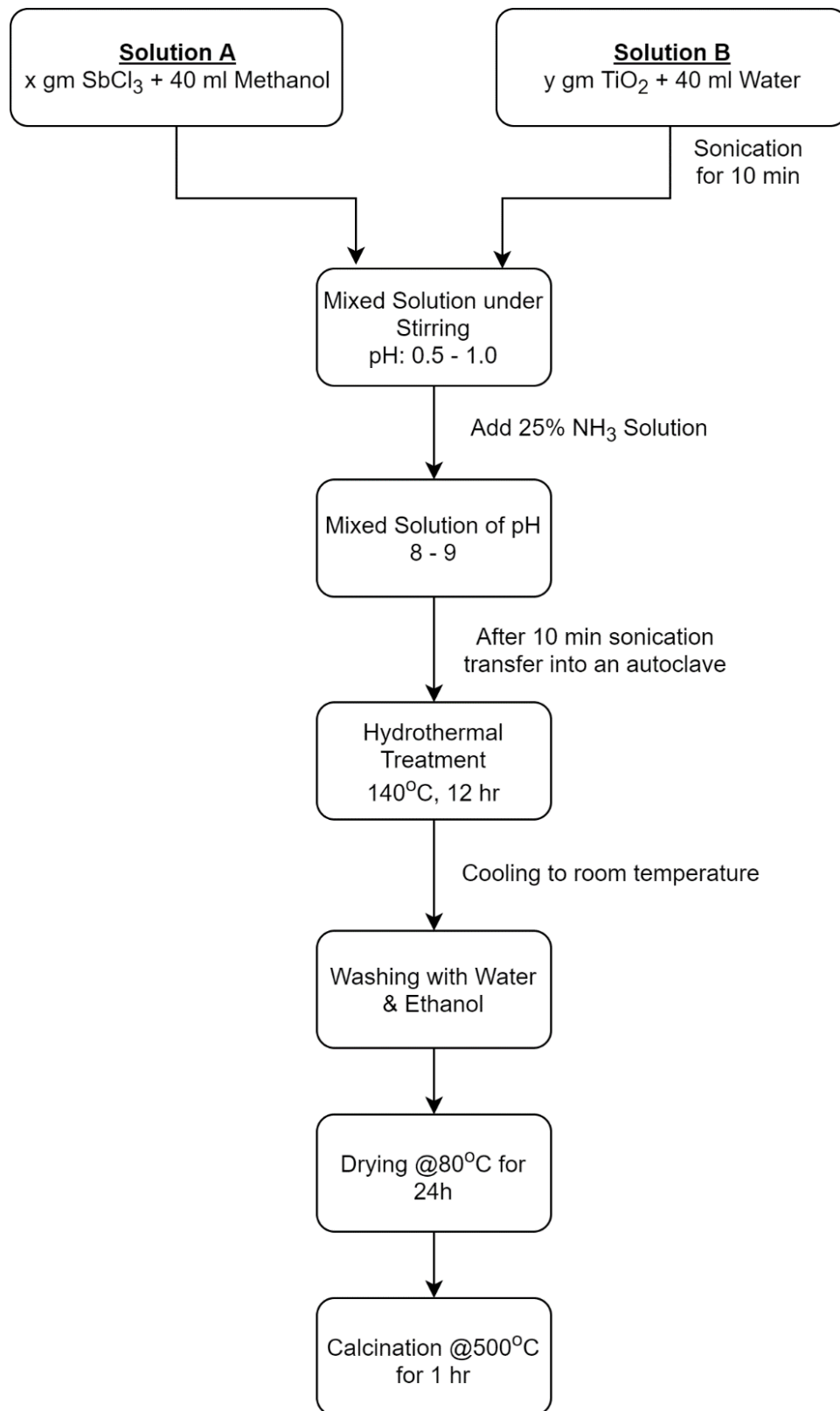
Series of Sb<sub>2</sub>O<sub>3</sub>/TiO<sub>2</sub>, with the molar ratio of Sb<sub>2</sub>O<sub>3</sub> to TiO<sub>2</sub> in the range of 0.5-2 mol%, were synthesized according to the literature from (Liu et al., 2012), named facile hydrothermal technique. In a typical process, certain amount of antimony trichloride (SbCl<sub>3</sub>) was dissolved in 40 ml pure methanol at room temperature to form a solution, named as solution A. Another solution, named as solution B, was made by dissolving the proportional amount of TiO<sub>2</sub> in 40 ml distilled water and activated by sonication for 10 min. TiO<sub>2</sub> was synthesized earlier as described in section 5.2.1. Then under stirring, two above solutions (A and B) were mixed to form a suspension and the pH of the suspension was maintained at 8-9 by adding ammonia (NH<sub>3</sub>·H<sub>2</sub>O, 25 wt%) solution. The suspension was then subjected to sonication for 10 min and then it was transferred into a Teflon-lined stainless-steel autoclave for hydrothermal treatment for 12 h at 140°C. After hydrothermal treatment, the autoclave was cooled down to room temperature. The white powder of Sb<sub>2</sub>O<sub>3</sub>/TiO<sub>2</sub> was separated by centrifugation and washed with distilled water then with pure alcohol, followed by drying at 80°C. Finally, the white powder was calcinated at 500°C for one hour.

Reactions:



Table 5.2: Required amount of antimony trichloride and titanium dioxide for synthesis

Molar ratio of Sb <sub>2</sub> O <sub>3</sub> to TiO <sub>2</sub>	Antimony trichloride, gm	Titanium dioxide, gm
0.5	7.14	2.5
1	9.14	1.6
2	10.28	0.9

Figure 5.2: Synthesis process of  $\text{Sb}_2\text{O}_3/\text{TiO}_2$  nanocatalysts.

### **5.3. Characterization methods**

#### **5.3.1. XRD analysis**

X-ray Diffraction is, a nondestructive technique, widely used for the identification of crystalline structure of unknown powdered materials (Callister and Rethwisch, 2011). It delivers information related to unit cell dimensions, crystal phase, crystal orientation and crystallinity of the materials. XRD analysis was made in a PANalytical X'pert Pro Multipurpose X-ray Diffractometer. In a typical experiment powdered material are placed in the sample holder and the diffraction peaks, generated by the interaction of monochromatic X-rays and crystalline materials, are recorded against diffraction angle  $2\theta$  (10-100°). High intensity of the peaks is observed when the Bragg's law is satisfied by a set of crystallographic planes. Finally, the observed peaks were matched and compared with the JCPDS (Joint Committee of Powder Diffraction Standards) database and the crystalline phases were determined.

#### **5.3.2. SEM and EDX analysis**

Scanning Electron Microscopy (HITACHI, S-4800) was used to study the surface morphology of the catalysts. Micrographs were taken at 100k and 250k times magnification while the operating voltage was 30 kV. Elemental composition was analyzed by using an Energy- dispersive X-ray (EDX) spectrometer that was equipped with SEM.

#### **5.3.3. BET Analysis**

Textural properties of the synthesized catalysts were determined from N<sub>2</sub> adsorption-desorption isotherm at 77K. The experiments were performed in a Micromeritics Tristar II plus surface area and porosity analyzer.

#### **5.3.4. UV-Vis diffuse reflectance spectra**

The optical properties of the synthesized catalysts were characterized by UV-Vis diffuse reflectance spectroscopy. Reflectance spectra of the powdered materials were recorded on a Lambda 950 spectrophotometer (Perkin Elmer) using BaSO<sub>4</sub> as a reference material. All the experiments were conducted at room temperature in the wavelength range of 200-800 nm.

Obtained reflectance spectra was then converted to the absorption spectrum using the Kubelka–Munk function (Wang et al., 2012):

$$F(R) = \frac{1-R^2}{2R} \dots \dots \dots \dots \quad (5.9)$$

Where, R is the reflectance spectra. The band gap energy was determined from the theory of optical absorption (Aghabeygi and Khademi-Shamami, 2018):

$$\alpha h\nu = C(h\nu - E_g)^{1/2} \dots \dots \quad (5.10)$$

Where,  $\alpha$  = absorption co-efficient  
 $h$  = Planck's constant,  $6.63 \times 10^{-34}$  m<sup>2</sup> kg/s.  
 $\nu$  = light frequency  
 $C$  = proportionality constant based on material  
 $E_g$  = the bandgap energy.

The bandgap energy can be obtained by extrapolating the steeper portion of the  $(\alpha h\nu)^2$  vs.  $h\nu$  plot (also known as Tauc's plot) to  $(\alpha h\nu)^2 = 0$ . It can be noted that, the Kubelka–Munk function,  $F(R)$ , can be used instead of  $\alpha$  in Eq. (2).

#### 5.4. Photocatalytic Experiment

Photocatalytic experiment was conducted in a 50 cm<sup>3</sup> quartz beaker under the UV light irradiation. In a typical experiment, the calculated amount of catalysts and BP-3 solutions were taken into the reactor and placed on a magnetic stirrer. The rotational speed of the stirrer was fixed at 500 rpm during all the experiment. Prior to light irradiation, the mixed sample was kept stirring in dark condition for 0.5 h to achieve the adsorption-desorption equilibrium. Photocatalytic reaction time was started with the starting time of light irradiation. The first sample was taken at the end of dark condition and considered as the initial concentration for photocatalytic degradation. The samples were then withdrawn periodically, and the suspended catalysts were removed by filtration with 0.2  $\mu$ m RC membrane prior to store in a vial for HPLC analysis. Photocatalytic degradation rate was calculated by  $C_t/C_0$ . Where,  $C_0$  is the initial concentration before light irradiation and  $C_t$  is the concentration at time t.

## 5.5. Analytical Methods

### 5.5.1. HPLC method for BP-3 analysis

BP-3 was analyzed on a SHIMADZU LC-20ADsp HPLC equipped with a UV/VIS detector. The detection wavelength of BP-3 was 287 nm. A Kinetex 5 $\mu$ m EVO C18 100Å column (150 x 4.6 mm) was used for the separation. Mobile phase was consisted of acetonitrile and 0.1% acetic acid solution (70:30, v/v) and the flowrate was maintained as 1.0 ml/min. The column temperature was upheld at 30°C and the injection volume of BP-3 was 20 $\mu$ L.

### 5.5.2. GC-MS for identification of degradation intermediates

Degradation byproducts were identified using GC-MS analysis. Samples were prepared using the solid phase extraction (SPE) columns (Chromabond C18 ec, octadecyl-modified silica, encapped, Macherey-Nagel). The column contains 500 mg of C18 phase having a volume of 3 mL. The column was first conditioned with acetone and water of pH 7. After that, 3 ml of the sample was passed through the column slowly and then collected using acetone for analysis. The samples were analyzed by GC-MS (Agilent-GC 6890N, MS 5975) with an Agilent GC column DB-1MS (dimensions: 30 m  $\times$  0.25 mm, 0.25 micrometer). The inlet temperature was 250°C in the splitless mode, and the injection volume was 1.0 ml. The oven temperature was programmed at 60°C for 2min, followed by a heating rate of 5°C /min to reach 300°C, where it was held for 2 min at 300°C. The obtained results were compared with the reference available in the NIST2014 MS library.

### 5.5.3. Methods of TOC determination

The degree of mineralization after the photocatalytic treatment was estimated by analyzing the Total Organic Carbon (TOC) before and after the experiment using a TOC analyzer (SHIMADZU TOC-V<sub>CPH/CPN</sub> equipped with ASI-V Autosampler). The TOC removal efficiency was calculated by the following equation:

$$\% \text{Removal of TOC} = \frac{TOC_i - TOC_f}{TOC_i} \times 100 \quad \dots \quad (5.11)$$

Where,  $TOC_i$  and  $TOC_f$  represents the initial and final TOC concentration (mg/L) respectively.

## 6. RESULT AND DISCUSSION

This section deals with the outcome of research plan with possible discussion of obtained result. This section is organized with the characterization results followed by photocatalytic experiment results.

### 6.1. Characterization of catalysts

Synthesized composite catalysts were characterized by different characterization techniques such as XRD, SEM, BET, FTIR, UV-Vis DRS and results are discussed in the following sub-sections.

#### 6.1.1. XRD Analysis

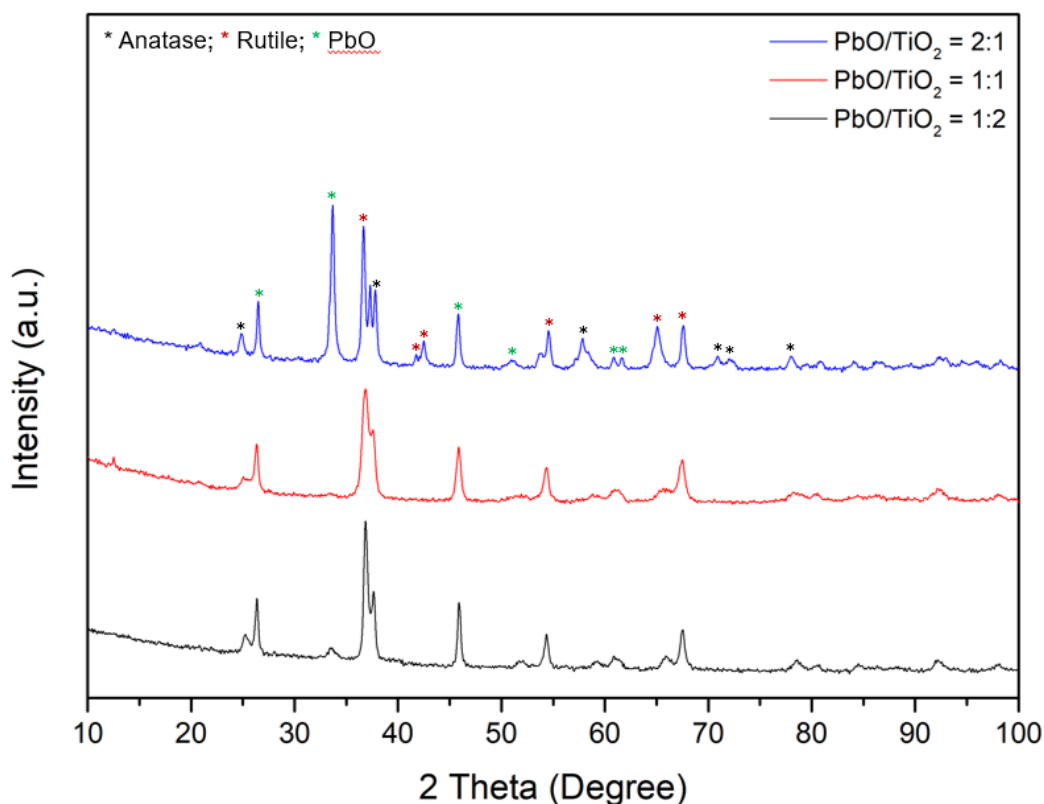


Figure 6.1: XRD patterns of synthesized PbO/TiO<sub>2</sub> catalysts of different ratio.

X-ray Diffraction peaks of PbO/TiO<sub>2</sub> catalysts for different ratio of composites are illustrated in the Figure 6.1. The diffraction peaks at 25.3°, 37.8° and 54.0° corresponds to the (101), (004) and (105) planes of anatase TiO<sub>2</sub> (JCPDS #21-1272), respectively. The other peaks at 27.4°, 36.1°,

55.3° and 68.7 could be indexed to the (110), (101), (211) and (112) facets of rutile TiO<sub>2</sub> (JCPDS #21-1276). The characteristic peaks of PbO at 2θ of 28.5° and 31.7° corresponds to the plane of (101) and (110) respectively (JCPDS #78-1666) and confirms the formation of PbO/TiO<sub>2</sub> composites.

Figure 6.2 represents the XRD patterns of Sb<sub>2</sub>O<sub>3</sub>/TiO<sub>2</sub> catalysts with different molar ratio of Sb<sub>2</sub>O<sub>3</sub> to TiO<sub>2</sub>. It can be seen both anatase and rutile phase exists in the synthesized catalysts. The characteristic peaks match with the (JCPDS #21-1272) and (JCPDS #21-1276) for anatase and rutile respectively. The characteristic peak at diffraction angle of 28.3° corresponds to the orthorhombic Sb<sub>2</sub>O<sub>3</sub> (JCPDS #11-694). Peaks at 28.3, 34.5, 57.2 and 59.5° corresponds to the (222), (331), (444) and (551) planes respectively (Zeng et al., 2004). A little shift in the peaks can be attributed to the partial substitution of Ti<sup>4+</sup> sites in TiO<sub>2</sub> by Sb<sup>3+</sup> (Liu et al., 2012).

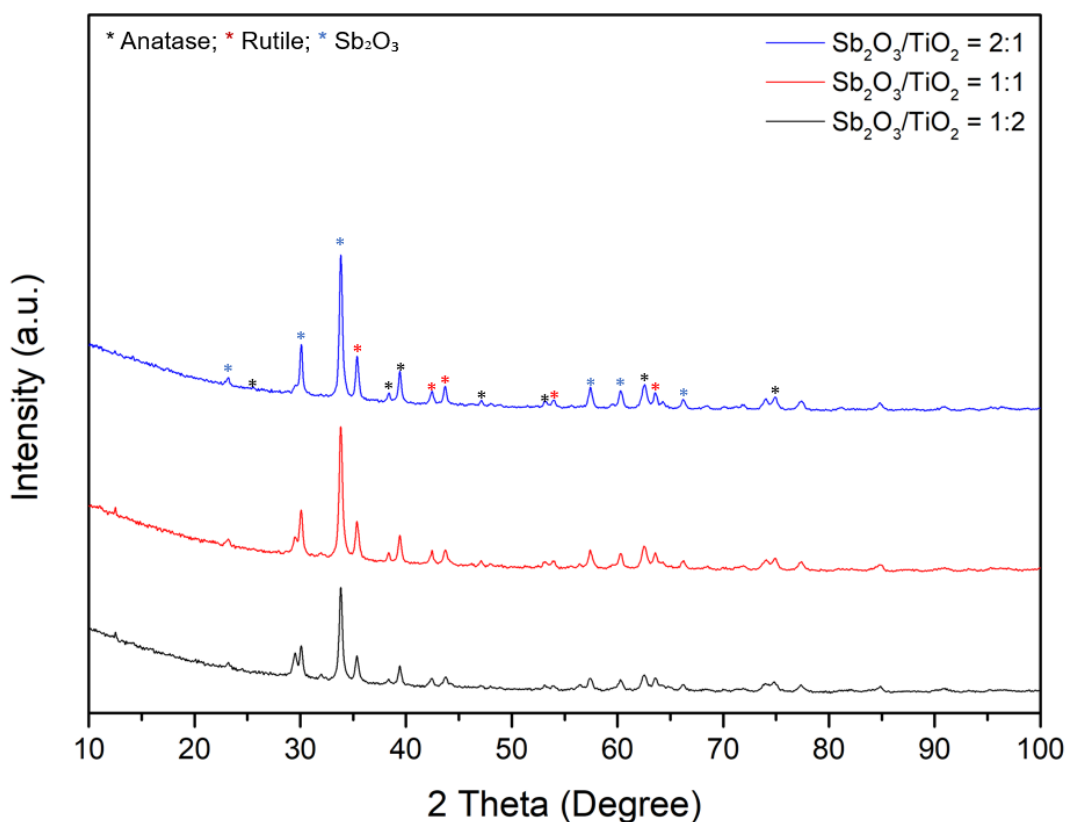


Figure 6.2: XRD patterns of synthesized Sb<sub>2</sub>O<sub>3</sub>/TiO<sub>2</sub> catalysts of different ratio.

### 6.1.2. SEM Analysis

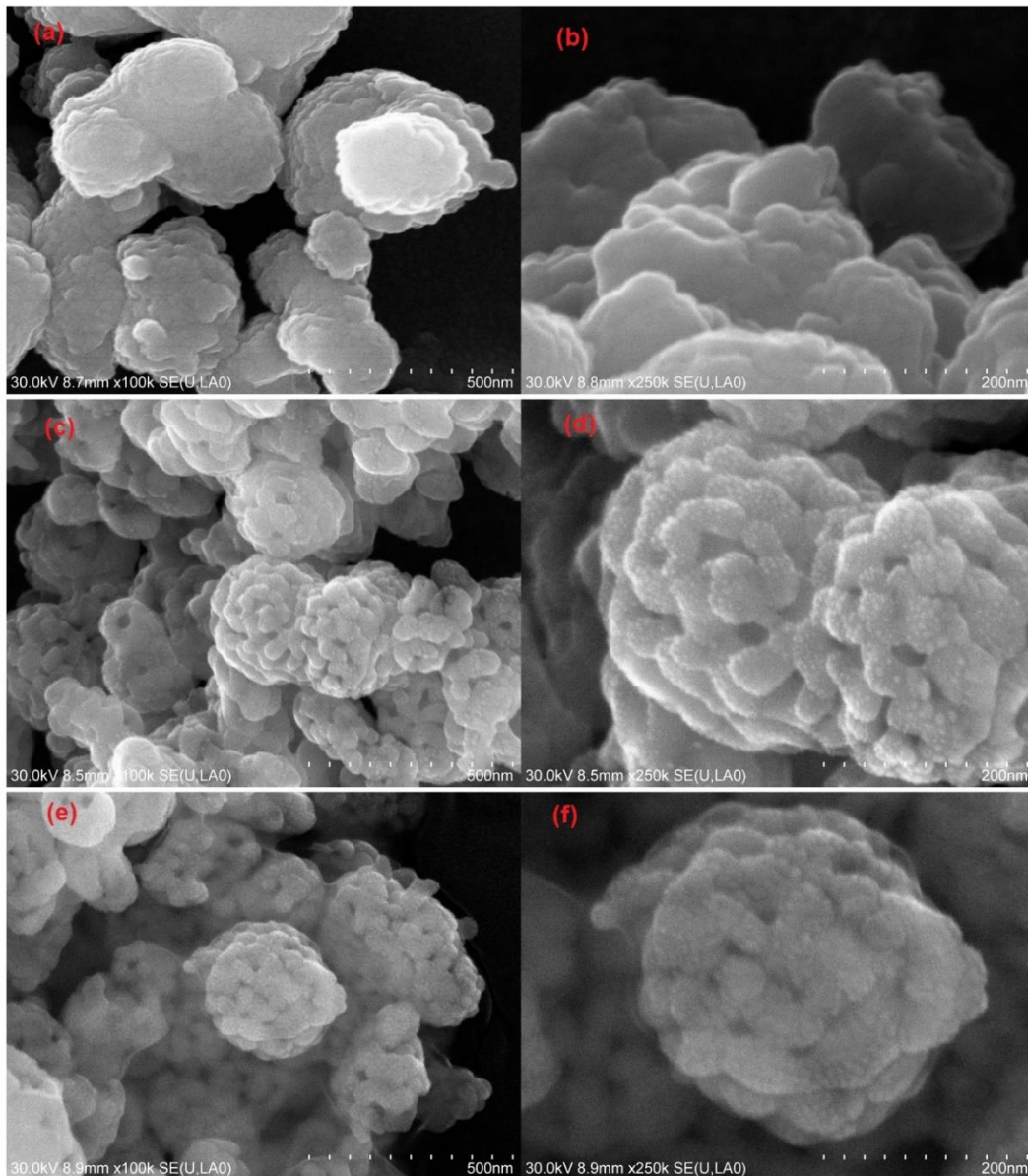


Figure 6.3: SEM micrograph of synthesized  $\text{PbO}/\text{TiO}_2$  photocatalysts (a&b:  $\text{PbO}/\text{TiO}_2 = 1:2$ ; c&d:  $\text{PbO}/\text{TiO}_2 = 1:1$ ; e&f:  $\text{PbO}/\text{TiO}_2 = 2:1$ ).

Scanning Electron Micrographs (SEM) of  $\text{PbO}/\text{TiO}_2$  catalysts are presented in Figure 6.3. As can be seen from the figure that, the particles have an agglomerated flower like structures (a & e) which results in a high surface area. Also, the surface of the particles seems to be porous that may facilitate the adsorption during experiment. The particle size was approximately 200-300 nm.

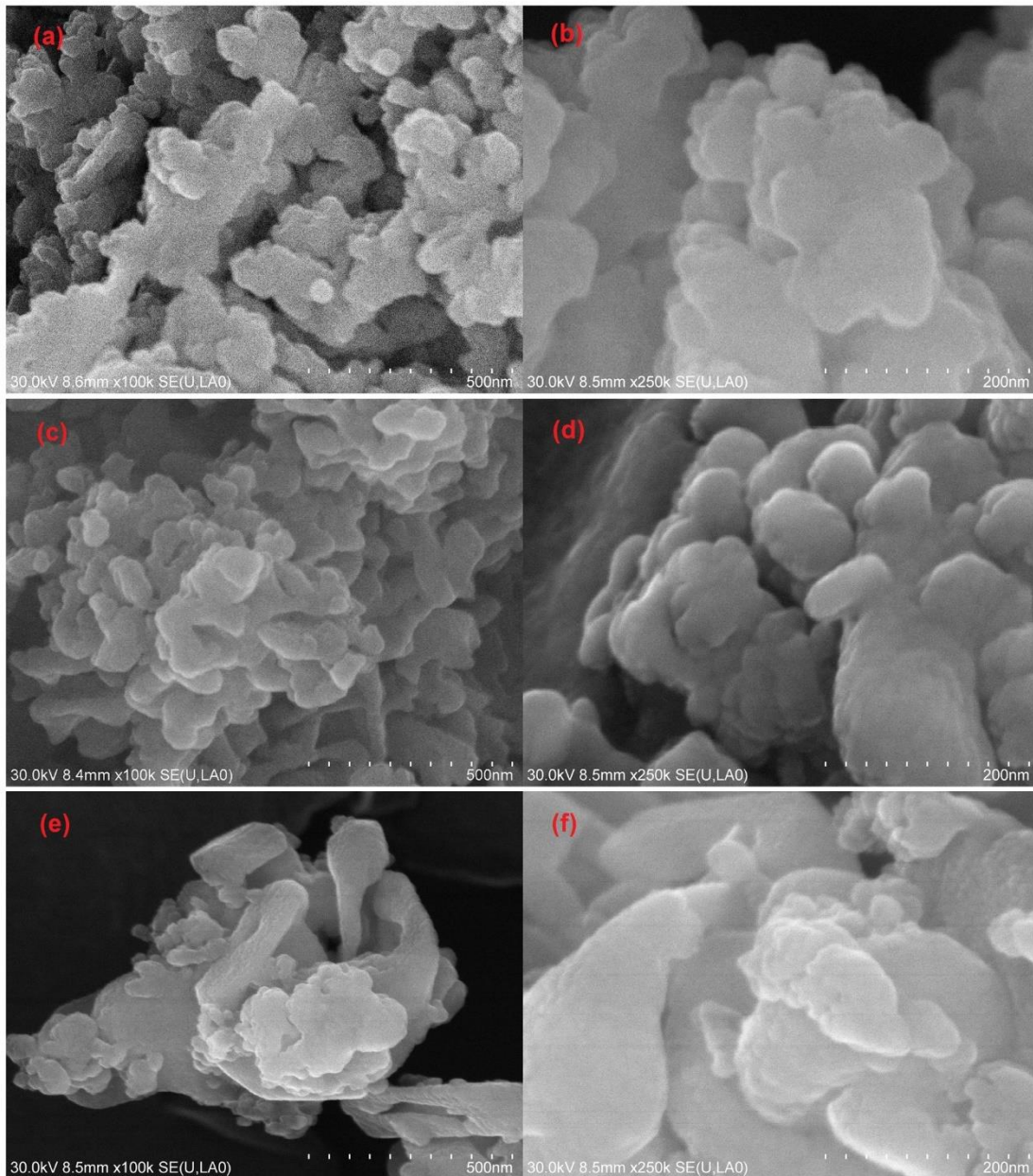
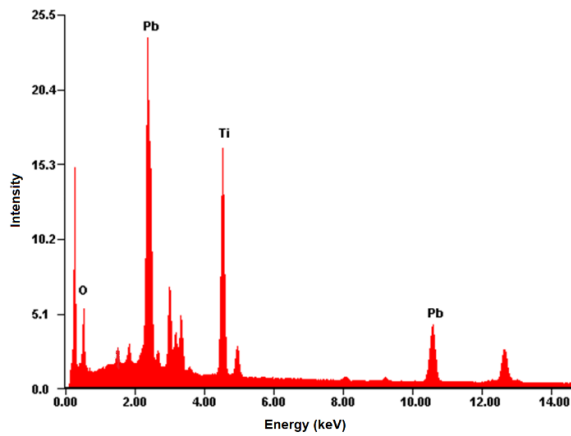
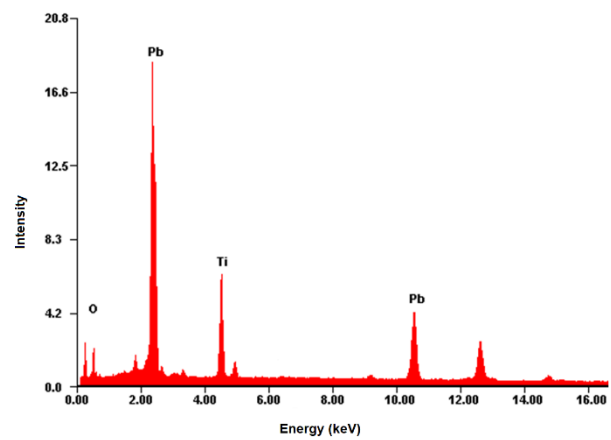
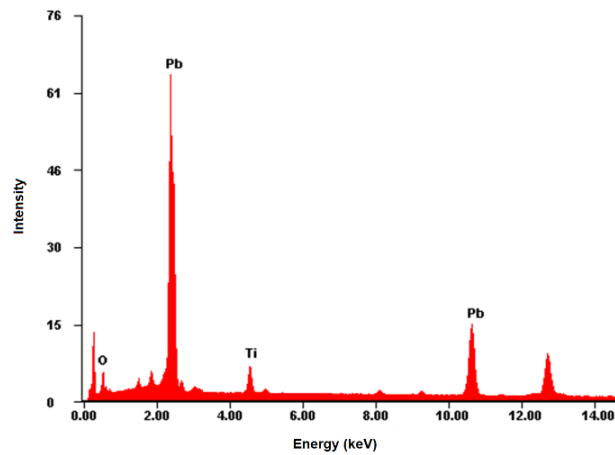


Figure 6.4: SEM micrograph of synthesized  $\text{Sb}_2\text{O}_3/\text{TiO}_2$  photocatalysts (a&b:  $\text{Sb}_2\text{O}_3/\text{TiO}_2 = 1:2$ ; c&d:  $\text{Sb}_2\text{O}_3/\text{TiO}_2 = 1:1$ ; e&f:  $\text{Sb}_2\text{O}_3/\text{TiO}_2 = 2:1$ )

SEM images of  $\text{Sb}_2\text{O}_3/\text{TiO}_2$  composite materials are presented in Figure 6.4. It can be seen that, in every case  $\text{Sb}_2\text{O}_3/\text{TiO}_2$  composites are consists of an irregular shaped aggregated particle. Particles size ranges from 50-100 nm due to their irregular shape and structure.

### 6.1.3. EDS Analysis

Figure 6.5: EDS spectrum of PbO/TiO<sub>2</sub> (1:2).Figure 6.6: EDS spectrum of PbO/TiO<sub>2</sub> (1:1).Figure 6.7: EDS spectrum of PbO/TiO<sub>2</sub> (2:1).

EDS spectrum of PbO/TiO<sub>2</sub> catalysts are presented in Figure 6.5 to Figure 6.7. Elemental peaks of Pb, Ti and O are detected in every case as shown in the figure. Corresponding elemental compositions are presented in Table 6.1.s

Table 6.1: Mass and Atomic composition of PbO/TiO<sub>2</sub> catalysts from EDS data.

Elements	PbO/TiO <sub>2</sub> (1:1)		PbO/TiO <sub>2</sub> (1:2)		PbO/TiO <sub>2</sub> (2:1)	
	Wt%	At%	Wt%	At%	Wt%	At%
Pb	57.21	09.67	56.21	07.81	26.49	02.52
Ti	10.68	07.81	02.66	01.60	09.75	04.02
O	10.84	23.72	09.53	17.15	18.86	23.24

EDS spectrum of  $\text{Sb}_2\text{O}_3/\text{TiO}_2$  composites for different composition are presented in Figure 6.8 to Figure 6.10. Corresponding elemental compositions in terms of weight and atomic percentage are presented in the Table 6.2.

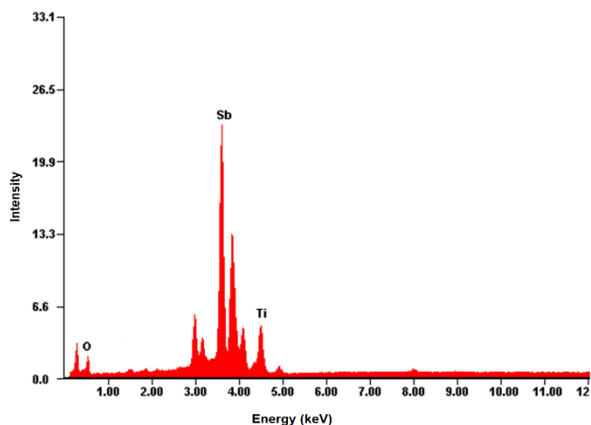


Figure 6.8: EDS spectrum of  $\text{Sb}_2\text{O}_3/\text{TiO}_2$  (1:1).

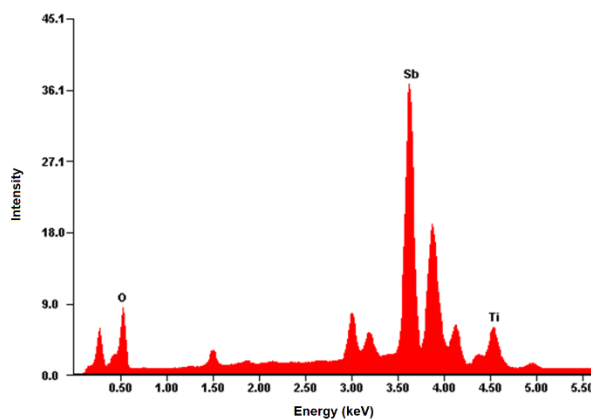


Figure 6.9: EDS spectrum of  $\text{Sb}_2\text{O}_3/\text{TiO}_2$  (2:1).

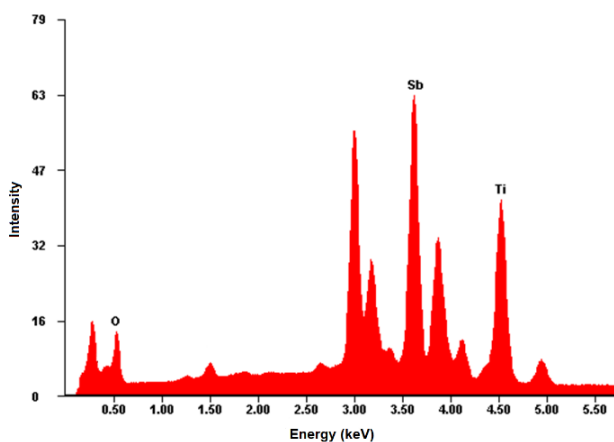


Figure 6.10: EDS spectrum of  $\text{Sb}_2\text{O}_3/\text{TiO}_2$  (1:2).

Table 6.2: Mass and Atomic composition of  $\text{Sb}_2\text{O}_3/\text{TiO}_2$  catalysts from EDS data

Elements	$\text{Sb}_2\text{O}_3/\text{TiO}_2$ (1:1)		$\text{Sb}_2\text{O}_3/\text{TiO}_2$ (2:1)		$\text{Sb}_2\text{O}_3/\text{TiO}_2$ (1:2)	
	Wt%	At%	Wt%	At%	Wt%	At%
Sb	60.58	17.58	51.81	13.56	30.64	05.39
Ti	08.27	06.10	04.65	03.10	11.83	05.29
O	07.78	17.17	17.98	35.82	19.57	26.21

### 6.1.4. BET Analysis

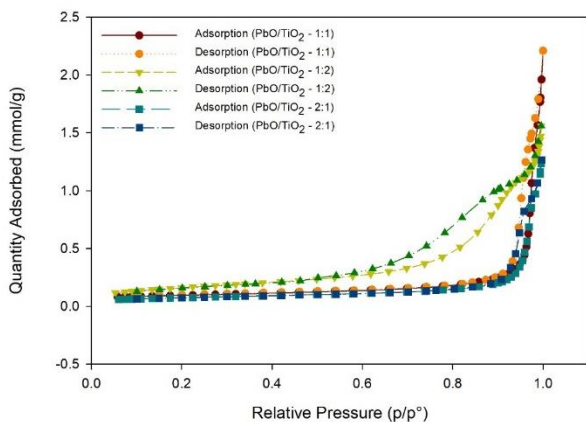


Figure 6.11: N<sub>2</sub> adsorption-desorption isotherm of PbO/TiO<sub>2</sub> photocatalysts.

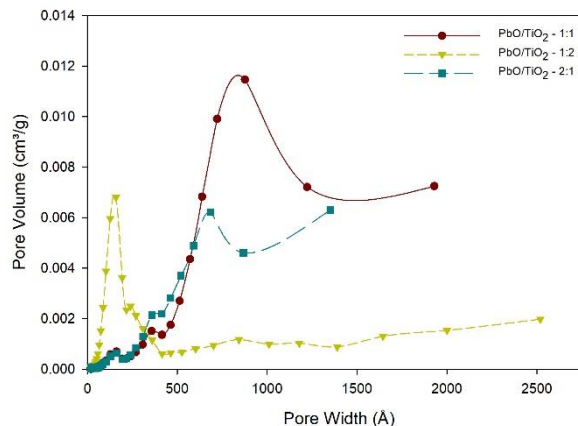


Figure 6.12: Pore size distribution of PbO/TiO<sub>2</sub> photocatalysts.

Textural properties of PbO/TiO<sub>2</sub> composites are analyzed by N<sub>2</sub> adsorption-desorption isotherm and the results are presented in Figure 6.11. The isotherms of PbO/TiO<sub>2</sub>-1:1 and PbO/TiO<sub>2</sub>-2:1 reveals the type III shape while type IV shape was observed in case of PbO/TiO<sub>2</sub>- 1:2 composite. A change from type IV to type III for increasing ratio of PbO reveals the change of surface properties due to the presence of PbO onto the TiO<sub>2</sub> surface. Also in case of type III shape the interaction between the adsorbate and adsorption site is relatively poor than type IV shape (Kruk and Jaroniec, 2001). A H3 hysteresis loop on type IV isotherm can be observed when materials comprised of aggregates of plate like particles that can be seen in Figure 6.3(a). Figure 6.12 represents the Barrett–Joyner–Halenda (BJH) pore distribution curve for three composites. BET surface area, average pore volume and pore size for three composites are presented in Table 6.3. Surface area decreases with the increased ratio of PbO to TiO<sub>2</sub>. Lowest pore volume was observed when the PbO/TiO<sub>2</sub> ratio was 2:1. Maximum average pore size was obtained at a ratio of 1:1 of PbO/TiO<sub>2</sub>.

Table 6.3: Physical properties of PbO/TiO<sub>2</sub> catalyts.

Catalysts	BET surface area (m <sup>2</sup> /g)	Pore volume (cm <sup>3</sup> /g)	Avg. pore size (Å)
PbO/TiO <sub>2</sub> (1:2)	13.13	0.050	149.09
PbO/TiO <sub>2</sub> (1:1)	7.08	0.060	508.79
PbO/TiO <sub>2</sub> (2:1)	5.79	0.040	340.38

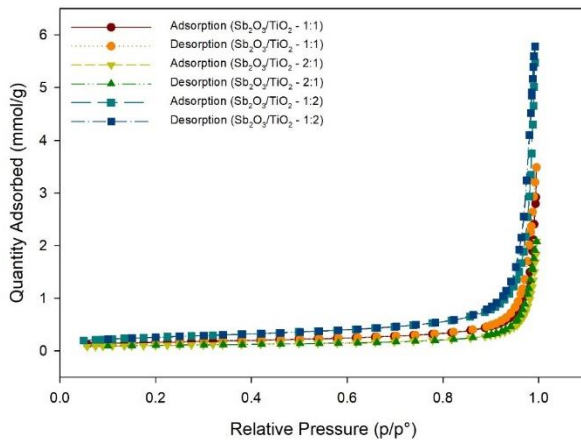


Figure 6.13: N<sub>2</sub> adsorption-desorption isotherm of Sb<sub>2</sub>O<sub>3</sub>/TiO<sub>2</sub> photocatalysts.

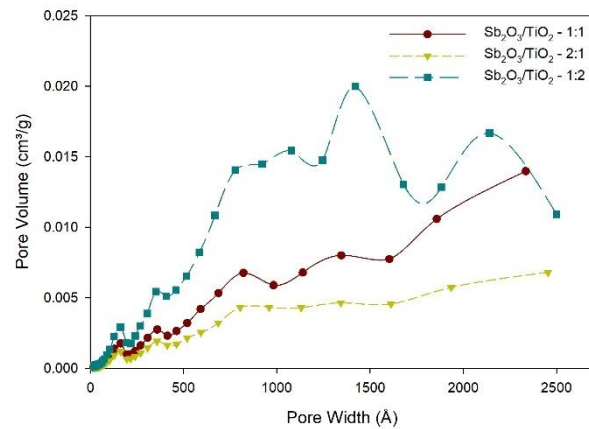


Figure 6.14: Pore size distribution of Sb<sub>2</sub>O<sub>3</sub>/TiO<sub>2</sub> photocatalysts.

Figure 6.13 represents the N<sub>2</sub> adsorption desorption isotherm of Sb<sub>2</sub>O<sub>3</sub>/TiO<sub>2</sub> catalysts and the corresponding pore size distribution curve is presented in Figure 6.14. In this case the isotherm shape belongs to type III which means the poor adsorption affinity to the adsorbate molecules. Moreover, no hysteresis loops were observed in case of Sb<sub>2</sub>O<sub>3</sub>/TiO<sub>2</sub> composites. Physical properties obtained from the adsorption-desorption isotherms are presented in Table 6.4 and it can be visualized that the BET surface area decreases with the increase of Sb<sub>2</sub>O<sub>3</sub> into the TiO<sub>2</sub> surface. Moreover, a decrease in the pore volume with the increase of Sb<sub>2</sub>O<sub>3</sub> content can be attributed to the formation of Sb<sub>2</sub>O<sub>3</sub> layer onto the TiO<sub>2</sub> surface.

Table 6.4: Physical properties of Sb<sub>2</sub>O<sub>3</sub>/TiO<sub>2</sub> catalysts.

Catalysts	BET surface area (m <sup>2</sup> /g)	Pore volume (cm <sup>3</sup> /g)	Avg. pore size (Å)
Sb <sub>2</sub> O <sub>3</sub> /TiO <sub>2</sub> (1:2)	20.27	0.199	465.72
Sb <sub>2</sub> O <sub>3</sub> /TiO <sub>2</sub> (1:1)	12.58	0.095	393.27
Sb <sub>2</sub> O <sub>3</sub> /TiO <sub>2</sub> (2:1)	7.99	0.057	394.93

### 6.1.5. Optical properties of the synthesized catalysts

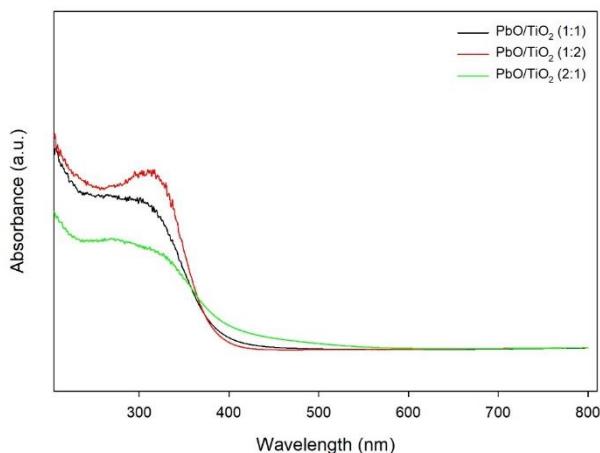


Figure 6.15: UV-Vis DR spectra of PbO/TiO<sub>2</sub> photocatalysts

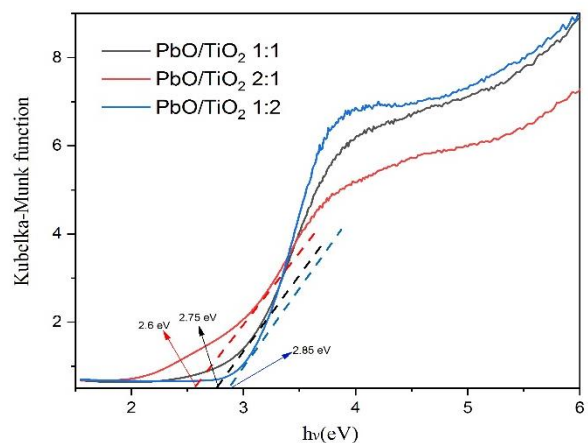


Figure 6.16: Plot of  $(\alpha h\nu)^2$  vs. photon energy ( $h\nu$ ) for bandgap estimation of PbO/TiO<sub>2</sub> photocatalysts.

To investigate the optical properties of the synthesized catalysts, light absorption efficiency was analyzed using UV-Vis Diffuse Reflectance spectrometer. Reflectance spectra of PbO/TiO<sub>2</sub> photocatalysts are illustrated in Figure 6.15 and the corresponding Tauc's plot is presented in Figure 6.16.

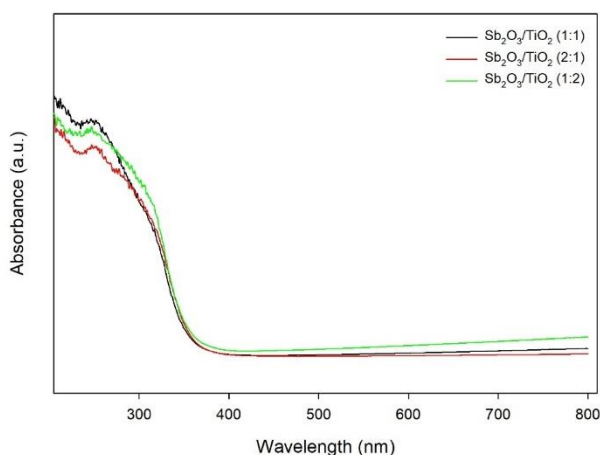


Figure 6.17: UV-Vis DR spectra of Sb<sub>2</sub>O<sub>3</sub>/TiO<sub>2</sub> photocatalysts.

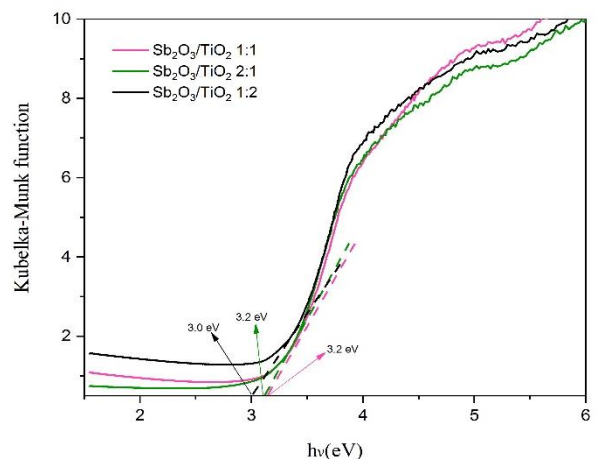


Figure 6.18: Plot of  $(\alpha h\nu)^2$  vs. photon energy ( $h\nu$ ) for bandgap estimation of Sb<sub>2</sub>O<sub>3</sub>/TiO<sub>2</sub> photocatalysts.

The bandgap values were determined from the Tauc's plot and the values are obtained as 2.75, 2.85 and 2.6 for PbO/TiO<sub>2</sub> (1:1), PbO/TiO<sub>2</sub> (1:2) and PbO/TiO<sub>2</sub> (2:1) respectively. The bandgap

values were narrower with the increasing amount of PbO which is in good agreement with Leelavathi et al. (Leelavathi et al., 2013).

The light absorption spectrum of  $\text{Sb}_2\text{O}_3/\text{TiO}_2$  catalysts are given in Figure 6.17. As can be visualized from the figure, all three catalysts displayed adsorption edges near 400 nm and the corresponding bandgap values are obtained from the Tauc's plot (Figure 6.18) as 3.2, 3.2 and 3.0 for  $\text{Sb}_2\text{O}_3/\text{TiO}_2$  (1:1),  $\text{Sb}_2\text{O}_3/\text{TiO}_2$  (2:1) and  $\text{Sb}_2\text{O}_3/\text{TiO}_2$  (1:2) respectively.

## 6.2. Photocatalytic performance of synthesized catalysts

Photocatalytic activity of the synthesized catalysts was verified under UV-C irradiation and the results are presented in Figure 6.19. Three experiments, two with catalysts and one without catalyst, were conducted under UV-C irradiation for 2 hours with 20  $\mu\text{M}$  concentration of pollutant in water. The catalysts were chosen arbitrary where the composite ratio was 1:1 and dose was 1g/L for the catalytic experiments. From the experiment it was found that, the degradation rate of BP-3 was only 2.5% after 2 hour of UV light irradiation; whereas, in presence of catalysts the degradation rate was 49.5% and 36.6% for  $\text{PbO}/\text{TiO}_2$  and  $\text{Sb}_2\text{O}_3/\text{TiO}_2$  respectively.

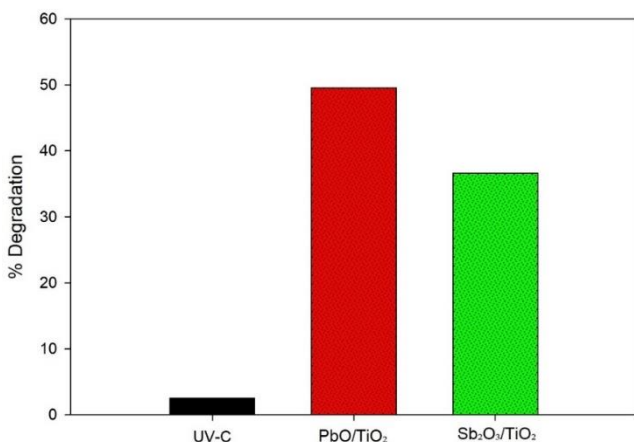


Figure 6.19: Performance testing of synthesized catalysts (Catalysts dose: 1g/L, Initial conc.: 20 $\mu\text{M}$ , Irradiation time: 2 hr).

### 6.3. Effect of Initial pH

In heterogeneous photocatalytic water treatment process pH plays a significant role since it can disturb the isoelectric point of photocatalysts. As a result, the surface charge of the catalysts changes which affects the interaction between the water contaminants and the catalysts surface. Also, the pH of the solution may alter the recombination rate of electron hole on the catalysts surface (Aghabeygi and Khademi-Shamami, 2018).

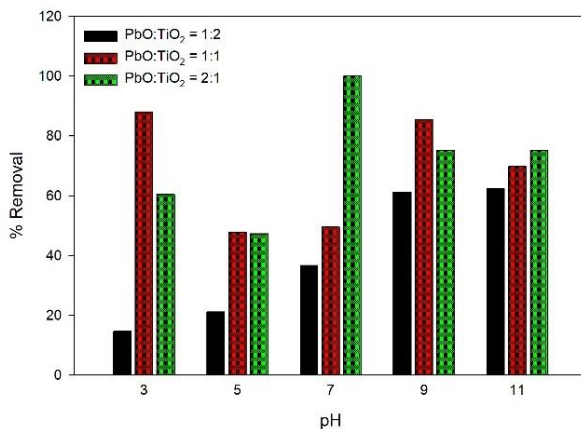


Figure 6.20: Effect of Initial pH on overall removal of pollutant by PbO/TiO<sub>2</sub> catalysts (Initial concentration = 20 $\mu$ M, Catalyst dose = 1g/L, UVC irradiation time = 120 min).

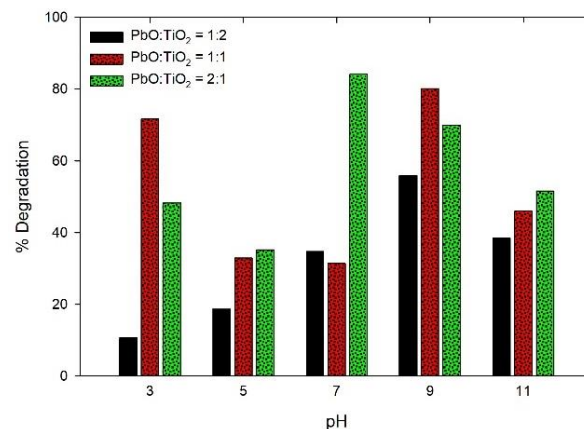


Figure 6.21: Effect of Initial pH on the photocatalytic degradation of pollutant by PbO/TiO<sub>2</sub> catalysts (Initial concentration = 20 $\mu$ M, Catalyst dose = 1g/L, UVC irradiation time = 120 min).

Photocatalytic experiments were performed at initial pH of 3, 5, 7, 9, 11 to investigate the effect of pH on photocatalytic degradation of BP-3. All the experiments were conducted at an initial concentration of 20 $\mu$ M, with catalyst dose of 1g/L and an irradiation time of 120 min. As can be seen from Figure 6.20 and Figure 6.21, each composite catalyst does not respond similarly at different pH conditions. For the catalyst PbO/TiO<sub>2</sub> (1:2) both removal and degradation rate were increased with the increasing pH up to 9 and at pH 11 the removal rate was almost same while the degradation rate was declined. For composite ratio 1:1, better removal and degradation rate was obtained at pH 9. Complete removal and maximum degradation rate of 84.1% was observed by PbO/TiO<sub>2</sub> (1:2) catalysts at pH 7. Comparing all these it can be conclude that, the best catalyst composite was PbO/TiO<sub>2</sub> (2:1) and the optimum initial pH of the solution for this catalyst is 7.

On the other hand,  $\text{Sb}_2\text{O}_3/\text{TiO}_2$  catalysts showed better photocatalytic activity at higher pH for all the composite ratios. The maximum removal efficiency was attained at pH 11 by  $\text{Sb}_2\text{O}_3/\text{TiO}_2$  (2:1) composites; however, the maximum degradation rate was observed at pH 9. Better degradation rate at alkaline conditions can be attributed to the higher density of hydroxyl ions, which facilitates the generation of more hydroxyl radical and therefore the better degradation rate of BP-3.

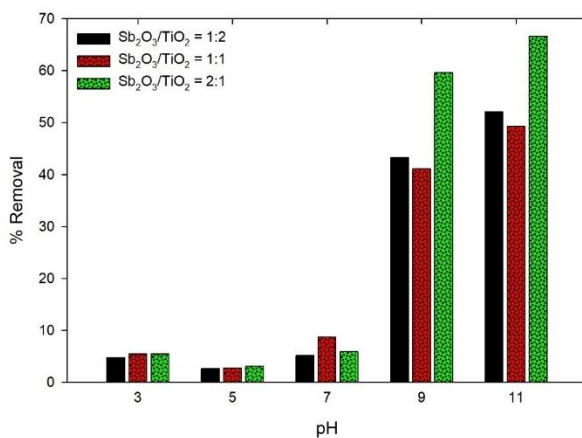


Figure 6.22: Effect of Initial pH on overall removal of pollutant by  $\text{Sb}_2\text{O}_3/\text{TiO}_2$  catalysts (Initial concentration =  $20\mu\text{M}$ , Catalyst dose =  $1\text{g/L}$ , UVC irradiation time = 120 min).

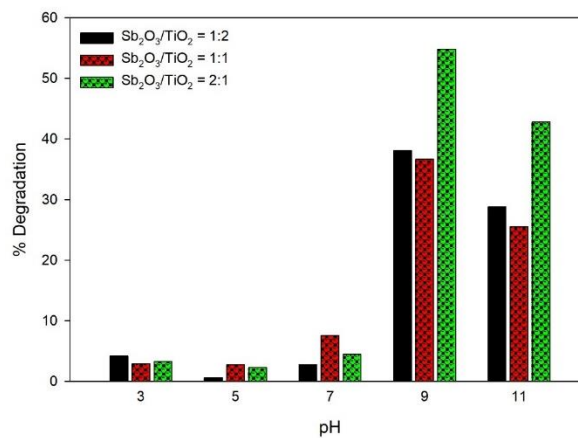


Figure 6.23: Effect of Initial pH on photocatalytic degradation of pollutant by  $\text{Sb}_2\text{O}_3/\text{TiO}_2$  catalysts (Initial concentration =  $20\mu\text{M}$ , Catalyst dose =  $1\text{g/L}$ , UVC irradiation time = 120 min).

## 6.4. Effect of catalysts dose

Photocatalytic reaction rate is strongly dependent on the catalysts loading. In many literatures it was evidenced a proportional relationship between the reaction rate and catalysts dose until an optimum loading is achieved. Beyond this optimum loading the reaction rate starts to decrease due to light screening effect of excess catalysts. As a result, the photocatalytic efficiency decreases. To estimate the optimum catalysts dosage the photocatalytic experiment was carried out at different amount of catalysts loading while the other operating parameters such as initial pH, concentration and reaction time were kept constant.

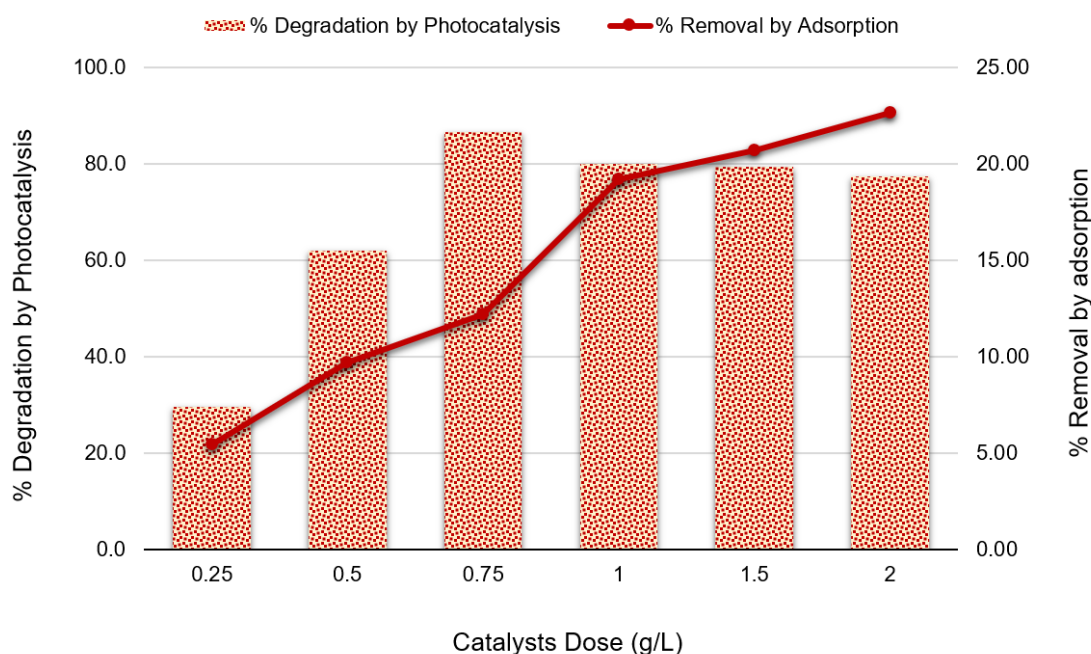


Figure 6.24: Effect of catalysts (PbO/TiO<sub>2</sub> (2:1)) dose on BP-3 degradation (Initial pH = 7, Initial concentration = 20 $\mu$ M, UVC irradiation time = 120 min).

Figure 6.24 represents the catalysts loading effects on photocatalytic degradation of BP-3. The experiments were carried out at pH 7 with an initial concentration of 20 $\mu$ M of BP-3 for 120 min. It is clearly seen that the photodegradation rate increases with increasing catalysts dosage and after a certain value it starts to decrease. However, a rising trend of adsorptive removal rate was observed with increasing catalysts dosage which increases the overall removal rate. Maximum photodegradation of 86.6% and overall removal of 98.8% was obtained when the catalysts dose was 0.75g/L. Complete removal was obtained when the catalysts dose was 1.5 g/L however the

photodegradation rate was relatively lower, 79.3%, due to higher adsorptive removal. Therefore, in terms of photocatalytic degradation the optimum dose of catalyst is 0.75 g/L.

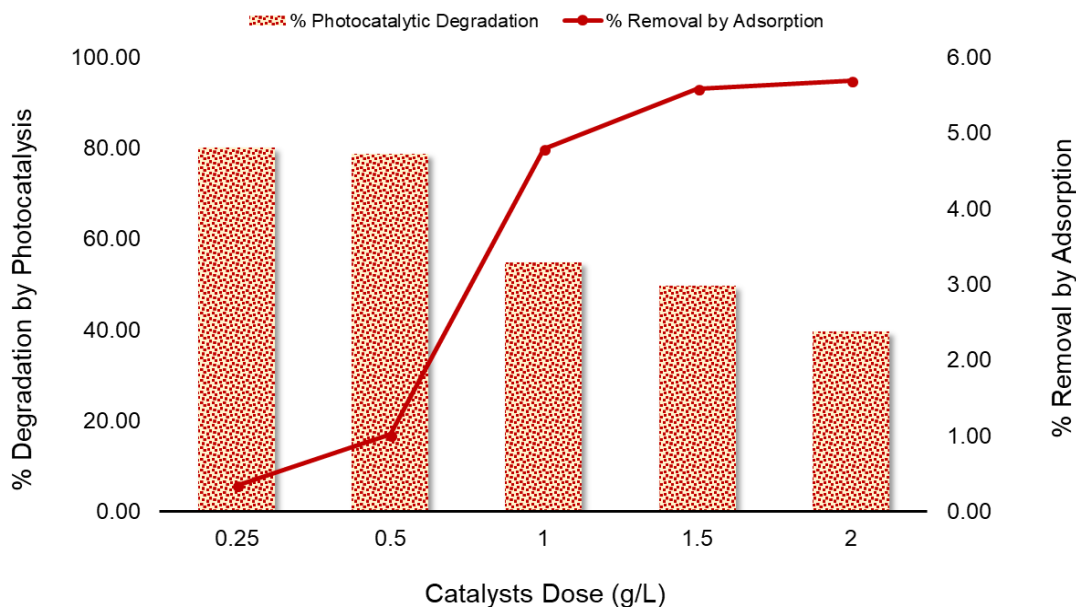


Figure 6.25: Effect of catalysts ( $\text{Sb}_2\text{O}_3/\text{TiO}_2$  (2:1)) dose on BP-3 degradation (Initial pH = 9, Initial concentration =  $20\mu\text{M}$ , UVC irradiation time = 120 min).

To investigate the effect of catalysts loading on the degradation of BP-3 by  $\text{Sb}_2\text{O}_3/\text{TiO}_2$  (2:1) catalysts a series of experiments were carried out at different catalysts doses ranging from 0.25 to 2 g/L. All the experiments were conducted with initial BP-3 concentration of  $20\mu\text{M}$  at pH 9 for 120 min under UV-C irradiation and the results are presented in Figure 6.25. A maximum photodegradation of 80.3% of BP-3 was obtained when the catalyst dose was 0.25 g/L. Further increase in catalysts loading significantly reduces the photodegradation rate. Also, the adsorptive removal rate was increasing with the increment of catalysts loading. It must be noted that the adsorptive removal is relatively low in case of  $\text{Sb}_2\text{O}_3/\text{TiO}_2$  catalyst than the  $\text{PbO}/\text{TiO}_2$  (2:1) catalyst due to their surface characteristics.

## 6.5. Effect of initial concentration

Initial concentration of water contaminants may significantly influence the performance of an established operating condition by reducing the photocatalytic efficiency. It is evident that, the surface of photocatalysts become saturated at higher concentration of contaminants which impedes the lights to reach the catalysts surface (Aghabeygi and Khademi-Shamami, 2018). As a result, the highly reactive hydroxyl radical production as well as the photocatalytic degradation rate declined. To study the concentration effect, the experiments were carried out different initial concentration while the other parameters such as operating pH, catalysts dose and reaction time were kept constant.

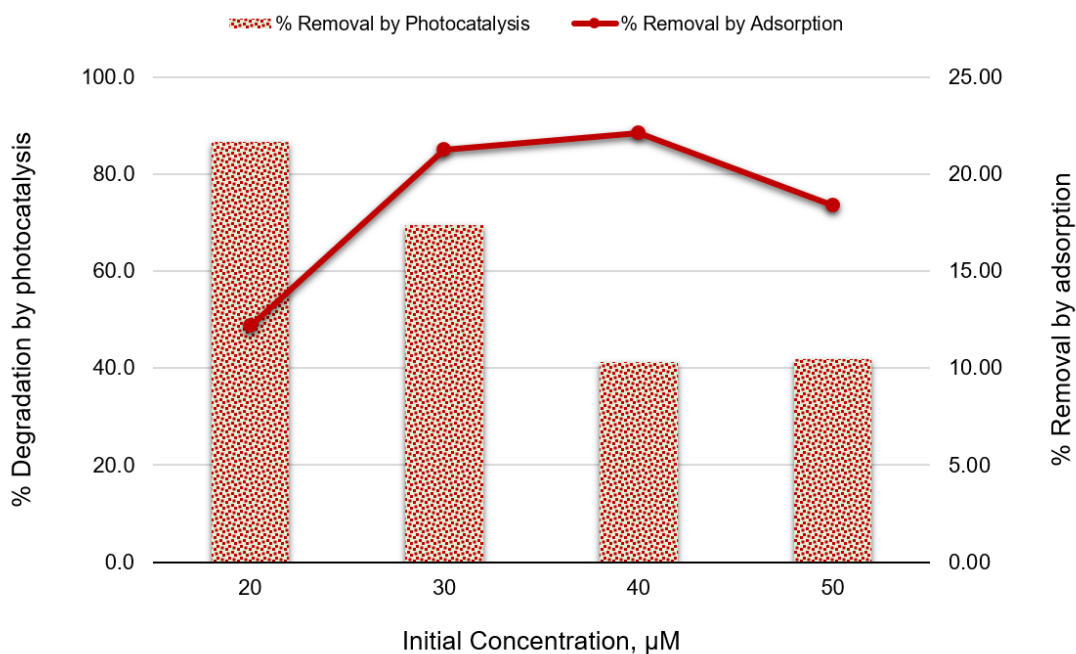


Figure 6.26: Effect of initial pollutant concentration on the degradation of BP-3 by PbO/TiO<sub>2</sub> (2:1) catalyst (Initial pH = 7, Catalyst dose = 0.75 g/L, UVC irradiation time = 120 min).

The photodegradation of BP-3 by PbO/TiO<sub>2</sub> (2:1) catalyst was studied at different initial concentration ranging from 20 to 50  $\mu\text{M}$  and the results are illustrated in Figure 6.26. all the experiments were conducted under UV-C irradiation at pH 7 and the catalysts dose was 0.75g/L. The experimental results revealed a declined trend in the photodegradation rate with the increasing initial concentration. The maximum degradation and removal was obtained at 20  $\mu\text{M}$  initial

concentration. Time dependent photodegradation was also studied (Figure 6.27) and modelled by Langmuir-Hinshelwood equation. The model equation that describes the photodegradation kinetics of BP-3 is expressed by the following equation (Al-Hamdi, 2017; Barka et al., 2008):

$$r = -\frac{dC}{dt} = \frac{k_r K_{ad} C}{1 + K_{ad} C} \quad \dots \quad \dots \quad \dots \quad \dots \quad (6.1)$$

Where,  $r$ ,  $k_r$ ,  $K_{ad}$  and  $C$  is the degradation rate, intrinsic rate constant, adsorption equilibrium constant and concentration of the pollutant respectively. Equation (6.1) can be simplified to the first-order kinetics expression by assuming the weak adsorption and low concentration of the compound as shown by equation (6.2).

$$-\ln\left(\frac{C}{C_o}\right) = k_r K_{ad} t = k_{app} t \quad \dots \quad \dots \quad \dots \quad (6.2)$$

Here,  $k_{app}$  is the apparent rate constant which can be obtained from the slope of  $-\ln(C/C_o)$  vs  $t$  plot.

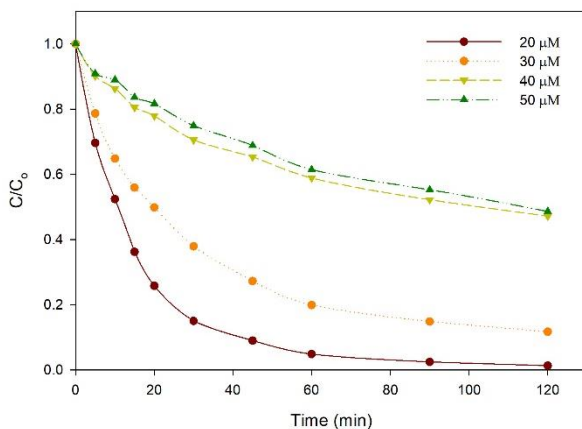


Figure 6.27: Degradation kinetics of BP-3 by (PbO/TiO<sub>2</sub> (2:1)) at different initial concentration of pollutant (Initial pH = 7, Catalyst dose = 0.75 g/L).

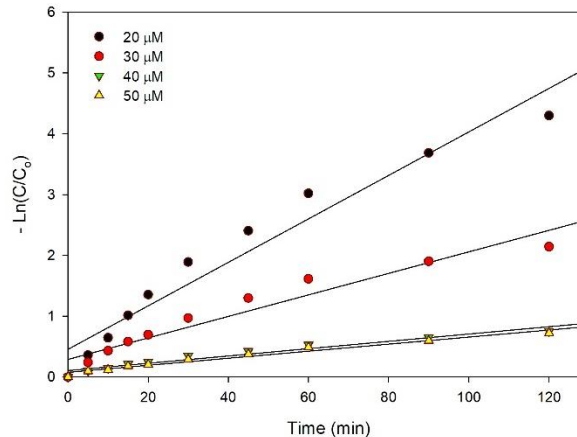


Figure 6.28: Degradation kinetics modelling of BP-3 by (PbO/TiO<sub>2</sub> (2:1)) at different initial concentration of pollutant (Initial pH = 7, Catalyst dose = 0.75 g/L).

A plot of  $-\ln(C/C_o)$  vs  $t$  for different initial concentration was presented in Figure 6.28 and the corresponding values of apparent rate constants were found from the slope of the plot and listed in Table 6.5 with their correlation coefficients. It was found a good relationship between the model

and experimental data and the apparent rate constant was declined with the increasing concentrations of BP-3.

Table 6.5: Kinetic parameters of BP-3 degradation by (PbO/TiO<sub>2</sub> (2:1)) at different initial concentration.

Initial Concentration, $\mu\text{M}$	20	30	40	50
$k$ ( $\text{min}^{-1}$ )	$3.58 \times 10^{-2}$	$1.77 \times 10^{-2}$	$0.60 \times 10^{-2}$	$0.58 \times 10^{-2}$
$R^2$	0.95	0.93	0.94	0.97

In case of Sb<sub>2</sub>O<sub>3</sub>/TiO<sub>2</sub> (2:1) catalyst, the effect of initial concentration on the photodegradation of BP-3 was studied in the range of 10-50 $\mu\text{M}$ . The reactions were carried out at pH 9 for 120 min under UV-C irradiation and the catalyst dose was kept 0.25 g/L in all case. Figure 6.29 represents the outcome of the experimental results and it can be visualize that the maximum photodegradation was at lower concentration and the degradation rate decreased gradually with the increasing initial concentration which was in agreement with (Aghabeygi and Khademi-Shamami, 2018).

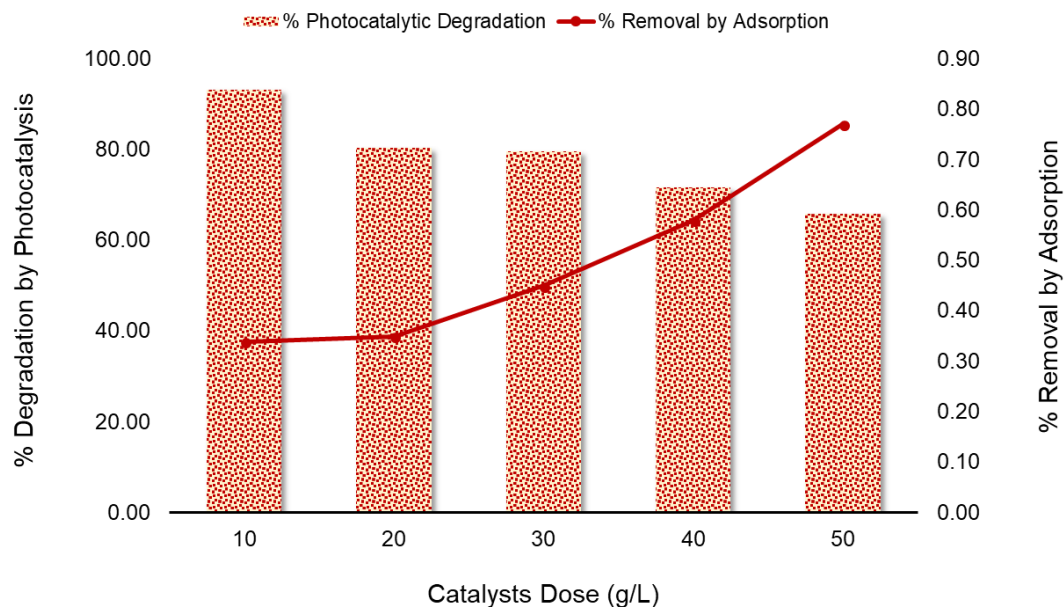


Figure 6.29: Effect of initial pollutant concentration on the degradation of BP-3 by Sb<sub>2</sub>O<sub>3</sub>/TiO<sub>2</sub> (2:1) catalyst (Initial pH = 7, Catalyst dose = 0.25 g/L, UVC irradiation time = 120 min).

The illustration of degradation kinetics is presented in Figure 6.30 and the corresponding kinetic modelling plot is given in Figure 6.31. Kinetics data were well fitted with the model equation (Eq.

6.2) and the values of rate constants for different initial concentrations are listed in Table 6.6. the maximum value of rate constant was observed at an initial concentration of 10 $\mu$ M.

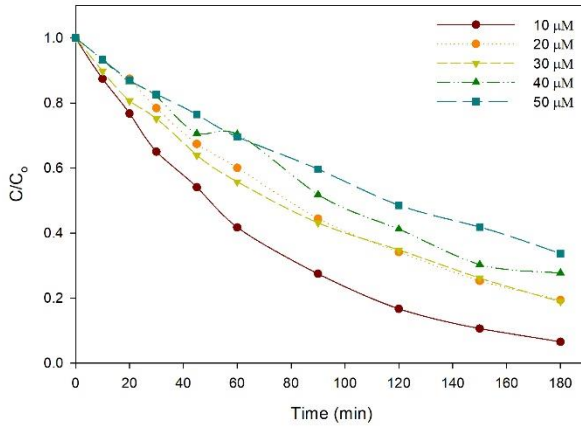


Figure 6.30: Degradation kinetics of BP-3 by (Sb<sub>2</sub>O<sub>3</sub>/TiO<sub>2</sub> (2:1)) at different initial concentration of pollutant (Initial pH = 7, Catalyst dose = 0.25 g/L).

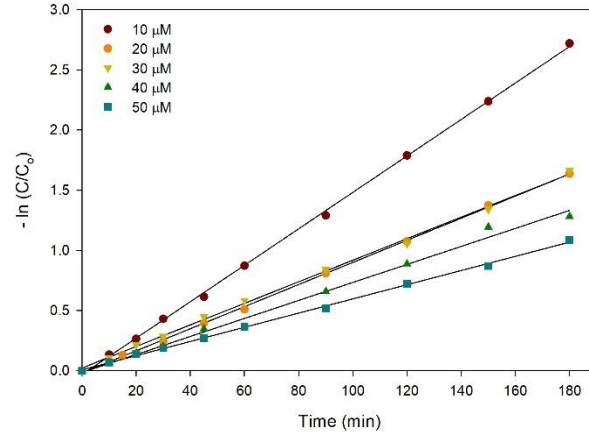


Figure 6.31: Degradation kinetics modelling of BP-3 by (Sb<sub>2</sub>O<sub>3</sub>/TiO<sub>2</sub> (2:1)) at different initial concentration of pollutant (Initial pH = 7, Catalyst dose = 0.25 g/L).

Table 6.6: Kinetic parameters of BP-3 degradation by (Sb<sub>2</sub>O<sub>3</sub>/TiO<sub>2</sub> (2:1)) at different initial concentration.

Initial Concentration, $\mu$ M	10	20	30	40	50
k ( $\text{min}^{-1}$ )	$1.51 \times 10^{-2}$	$0.92 \times 10^{-2}$	$0.89 \times 10^{-2}$	$0.75 \times 10^{-2}$	$0.59 \times 10^{-2}$
R <sup>2</sup>	0.99	0.99	0.99	0.99	0.99

## 6.6. Mineralization study

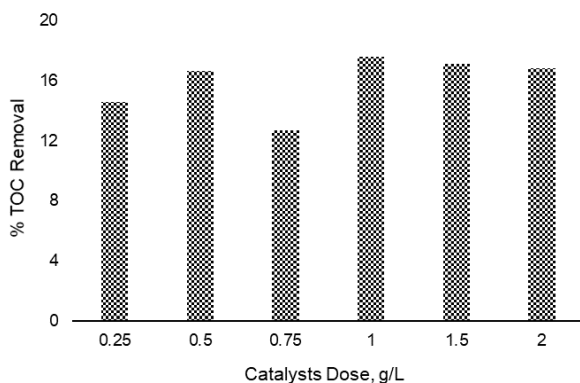


Figure 6.32: Mineralization efficiency of  $\text{PbO/TiO}_2$  (2:1) catalysts at different catalysts loading (Initial pH = 7, Initial concentration =  $20\mu\text{M}$ , UV-C irradiation time = 120 min).

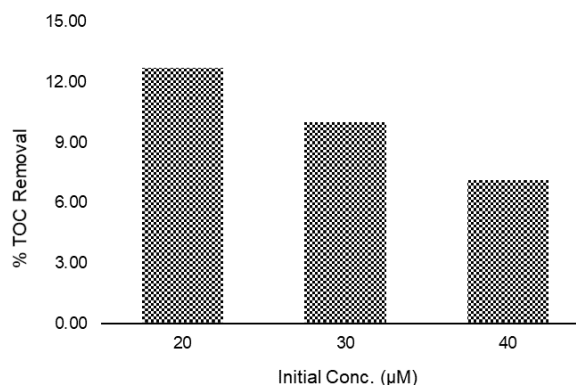


Figure 6.33: Mineralization efficiency of  $\text{PbO/TiO}_2$  (2:1) catalysts at different Initial Concentration (Initial pH = 7, Catalyst dose =  $0.75\text{ g/L}$ , UV-C irradiation time = 120 min).

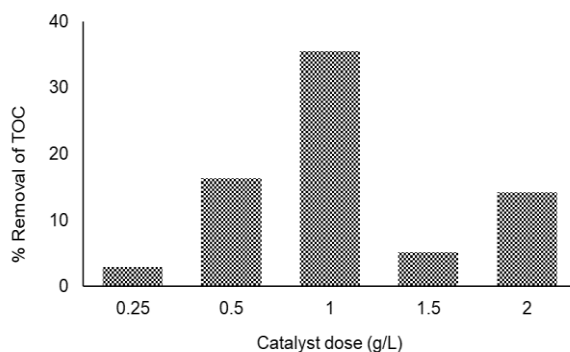


Figure 6.34: Mineralization efficiency of  $\text{Sb}_2\text{O}_3/\text{TiO}_2$  (2:1) catalysts at different catalysts loading (Initial pH = 9, Initial concentration =  $20\mu\text{M}$ , UV-C irradiation time = 120 min).

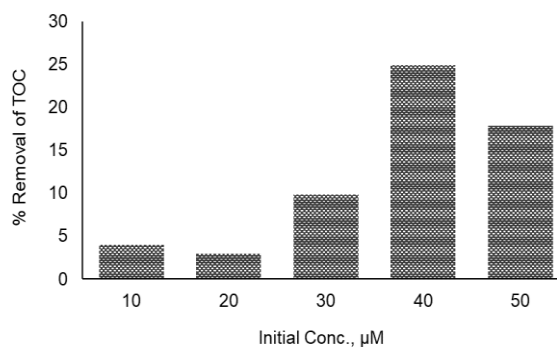


Figure 6.35: Mineralization efficiency of  $\text{Sb}_2\text{O}_3/\text{TiO}_2$  (2:1) catalysts at different Initial Concentration (Initial pH = 9, Catalyst dose =  $0.25\text{ g/L}$ , UV-C irradiation time = 120 min).

Mineralization efficiency in one of the key parameter that indicates the photocatalytic performance of the synthesized catalysts. Figure 6.32 represents the degree of mineralization by  $\text{PbO/TiO}_2$  (2:1) catalysts at different catalysts loading. The maximum mineralization efficiency of 17.6% was achieved when the catalyst loading was  $1\text{ g/L}$ . Mineralization efficiency at different initial concentration was presented in Figure 6.33. After two hours of reaction under UV-C irradiation maximum mineralization efficiency was achieved at  $20\mu\text{M}$  concentration. On the other hand,

mineralization efficiency was unpredictable in  $\text{Sb}_2\text{O}_3/\text{TiO}_2$  catalysis. Maximum mineralization efficiency of 35.5% was achieved when the catalysts dose was 1g/L (Figure 6.34). Effect of initial pollutant concentration on degree of mineralization for  $\text{Sb}_2\text{O}_3/\text{TiO}_2$  catalysis is presented in Figure 6.35. Poor mineralization efficiency in 120 min can be attributed to the absence of hydroxyl radical in the photocatalytic process. However, the mineralization efficiency can be improved by increasing the reaction time, is given in the Appendix Figure 2.

## 6.7. Identification of degradation byproducts

The GC-MS analysis was carried out for those samples achieved in optimum conditions for all system and it was observed that in all cases most byproducts were same. According to the structure of BP-3, the most probable degradation/transformation of BP-3 is due to a dominant photochemical and  $^1\text{O}_2$  radicals scavenger of the BP-3. Molecular structures were proposed for each intermediated/product based on the molecular ion masses and MS fragmentation patterns and presented in Figure 6.36. Among the byproducts, compounds include ethanol, pentamethyl-, 5-Hydroxy-7-methoxy-2-methyl-3-phenyl-4-chromenone and Phthalic acid, cyclobutyl propyl ester.

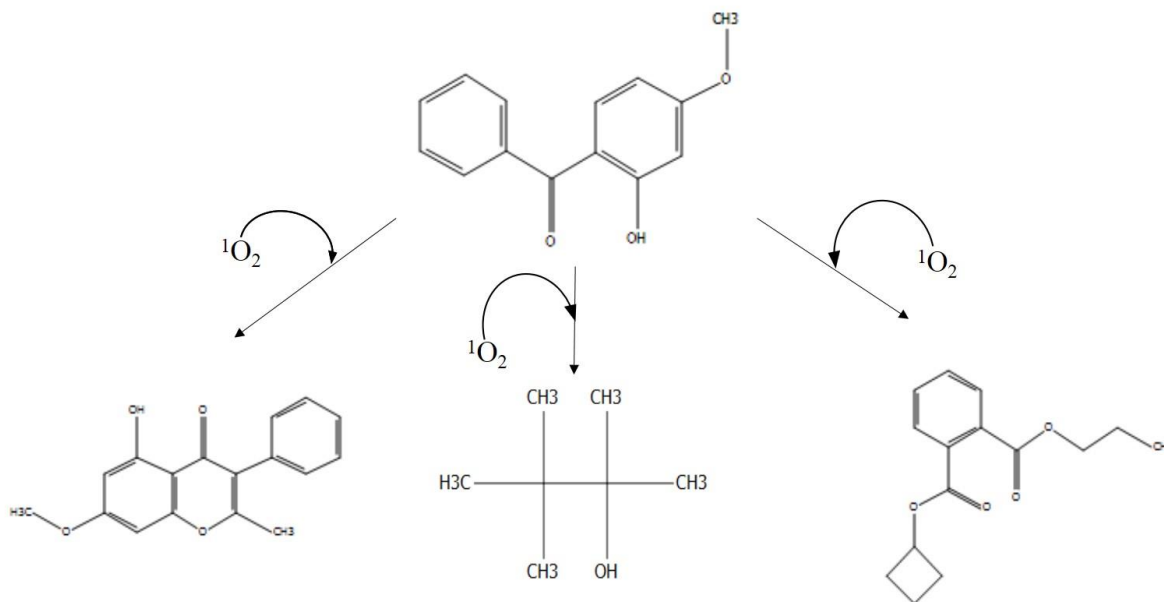


Figure 6.36: Possible degradation byproducts from photocatalytic degradation of BP-3.

## 7. CONCLUSION AND RECOMMENDATION

Photocatalytic degradation of organic UV filter BP-3 was studied under UV-C irradiation. Two composite photocatalysts, PbO/TiO<sub>2</sub> and Sb<sub>2</sub>O<sub>3</sub>/TiO<sub>2</sub> were synthesized by hydrothermal method. The characterization result reveals the formation of composite with desired physical and optical properties. Photocatalytic degradation results confirm the photocatalytic activity of the synthesized catalysts. The best result was obtained with PbO/TiO<sub>2</sub> composite where the ratio of PbO to TiO<sub>2</sub> was 2:1. This catalyst can completely remove the BP-3 from waste water at pH 7. However, the mineralization rate was relatively poor due to the absence of hydroxyl radical.

There are also some scopes to further research regarding these materials and processes. Some future recommendations are given below:

- In catalyst level:
  - Particle size and shape modification using different modifying agent.
  - Develop indirect Z-Scheme heterojunction.
- In Experiment level:
  - Development of new photocatalytic experiment system so that the light and catalysts interaction increase.
  - Development of continuous reactor system including monolith structures.

## REFERENCES

- Acero, J.L., Benitez, F.J., Teva, F., Leal, A.I., 2010. Retention of emerging micropollutants from UP water and a municipal secondary effluent by ultrafiltration and nanofiltration. *Chem. Eng. J.* 163, 264–272. doi:10.1016/j.cej.2010.07.060
- Aghabeygi, S., Khademi-Shamami, M., 2018. ZnO/ZrO<sub>2</sub>nanocomposite: Sonosynthesis, characterization and its application for wastewater treatment. *Ultrason. Sonochem.* 41, 458–465. doi:10.1016/j.ultsonch.2017.09.020
- Ahmad, S., Naseem, F., Shahid, M., Shakir, I., Aboud, M.F.A., Sarfraz, M., Khan, M.A., Rehman, A.U., Warsi, M.F., 2017. Visible light driven photocatalysis for water purification by highly crystalline multiferroic BiFeO<sub>3</sub>nanoparticles synthesized via wet chemical route. *Desalin. Water Treat.* 85. doi:10.5004/dwt.2017.21264
- Al-Anazi, A., Abdelraheem, W.H., Han, C., Nadagouda, M.N., Sygellou, L., Arfanis, M.K., Falaras, P., Sharma, V.K., Dionysiou, D.D., 2018. Cobalt ferrite nanoparticles with controlled composition-peroxymonosulfate mediated degradation of 2-phenylbenzimidazole-5-sulfonic acid. *Appl. Catal. B Environ.* 221, 266–279.
- Al-Hamdi, A., 2017. Synthesis and comparison of the photocatalytic activities of antimony, iodide, and rare earth metals on SnO<sub>2</sub> for the photodegradation of phenol and its intermediates under uv, solar and visible light irradiations. Lappeenranta University of Technology.
- An, T., Liu, J., Li, G., Zhang, S., Zhao, H., Zeng, X., Sheng, G., Fu, J., 2008. Structural and photocatalytic degradation characteristics of hydrothermally treated mesoporous TiO<sub>2</sub>. *Appl. Catal. A Gen.* 350, 237–243. doi:10.1016/j.apcata.2008.08.022
- Asahi, R., Morikawa, T., Ohwaki, T., Aoki, K., Taga, Y., 2001. Visible-light photocatalysis in nitrogen-doped titanium oxides. *Science (80-. )*. 293, 269–271. doi:10.1126/science.1061051
- Bai, J., Li, J., Liu, Y., Zhou, B., Cai, W., 2010. A new glass substrate photoelectrocatalytic electrode for efficient visible-light hydrogen production: CdS sensitized TiO<sub>2</sub>nanotube arrays. *Appl. Catal. B Environ.* 95, 408–413. doi:10.1016/j.apcatb.2010.01.020

- Baker, D.R., Kamat, P. V., 2009. Photosensitization of TiO<sub>2</sub> nanostructures with CdS quantum dots: Particulate versus tubular support architectures. *Adv. Funct. Mater.* 19, 805–811. doi:10.1002/adfm.200801173
- Bakkiyaraj, R., Bharath, G., Hasini Ramsait, K., Abdel-Wahab, A., Alsharaeh, E.H., Chen, S.-M., Balakrishnan, M., 2016. Solution combustion synthesis and physico-chemical properties of ultrafine CeO<sub>2</sub> nanoparticles and their photocatalytic activity. *RSC Adv.* 6. doi:10.1039/c6ra00382f
- Balmer, M.E., Buser, H.-R., Müller, M.D., Poiger, T., 2005. Occurrence of some organic UV filters in wastewater, in surface waters, and in fish from Swiss lakes. *Environ. Sci. Technol.* 39, 953–962.
- Barka, N., Assabbane, A., Nounah, A., Ichou, Y.A., 2008. Photocatalytic degradation of indigo carmine in aqueous solution by TiO<sub>2</sub>-coated non-woven fibres. *J. Hazard. Mater.* 152, 1054–1059. doi:10.1016/j.jhazmat.2007.07.080
- Batt, A.L., Furlong, E.T., Mash, H.E., Glassmeyer, S.T., Kolpin, D.W., 2017. The importance of quality control in validating concentrations of contaminants of emerging concern in source and treated drinking water samples. *Sci. Total Environ.* 579, 1618–1628.
- Behar, D., Rabani, J., 2006. Kinetics of hydrogen production upon reduction of aqueous TiO<sub>2</sub> nanoparticles catalyzed by Pd<sub>0</sub>, Pt<sub>0</sub>, or Au<sub>0</sub> coatings and an unusual hydrogen abstraction; steady state and pulse radiolysis study. *J. Phys. Chem. B* 110, 8750–8755. doi:10.1021/jp060971m
- Bester, K., 2003. Triclosan in a sewage treatment process—balances and monitoring data. *Water Res.* 37, 3891–3896.
- Bokare, A.D., Choi, W., 2014. Review of iron-free Fenton-like systems for activating H<sub>2</sub>O<sub>2</sub> in advanced oxidation processes. *J. Hazard. Mater.* doi:10.1016/j.jhazmat.2014.04.054
- Bokare, A.D., Choi, W., 2014. Review of iron-free Fenton-like systems for activating H<sub>2</sub>O<sub>2</sub> in advanced oxidation processes. *J. Hazard. Mater.* 275, 121–135.
- Bono-Blay, F., Guart, A., de la Fuente, B., Pedemonte, M., Pastor, M.C., Borrell, A., Lacorte, S.,

2012. Survey of phthalates, alkylphenols, bisphenol A and herbicides in Spanish source waters intended for bottling. *Environ. Sci. Pollut. Res.* 19, 3339–3349.
- Borhade, A. V., Uphade, B.K., Tope, D.R., 2013. PbO as an efficient and reusable catalyst for one-pot synthesis of tetrahydro benzo pyrans and benzyldene malonitriles. *J. Chem. Sci.* 125, 583–589. doi:10.1007/s12039-013-0396-8
- Callister, W.D., Rethwisch, D.G., 2011. *Materials Science and Engineering*, Eighth. ed. John Wiley & Sons, Inc.
- Celeiro, M., Vignola Hackbarth, F., U. de Souza, S.M.A.G., Llompert, M., Vilar, V.J.P., 2018. Assessment of advanced oxidation processes for the degradation of three UV filters from swimming pool water. *J. Photochem. Photobiol. A Chem.* doi:10.1016/j.jphotochem.2017.10.023
- Chatterjee, D., Mahata, A., 2001. Demineralization of organic pollutants on the dye modified TiO<sub>2</sub> semiconductor particulate system using visible light. *Appl. Catal. B Environ.* 33, 119–125. doi:10.1016/S0926-3373(01)00170-9
- Chen, X., Mao, S.S., 2007. Titanium dioxide nanomaterials: Synthesis, properties, modifications and applications. *Chem. Rev.* doi:10.1021/cr0500535
- Cheng, H., Zhao, Z., 1994. Hydrothermal Synthesis of PbO-TiO<sub>2</sub> Solid Solution. *Chem. Mater.* 46, 1033–1040. doi:10.1021/cm00043a027
- Chi, C., Pan, J., You, M., Dong, Z., Zhao, W., Song, C., Zheng, Y., Li, C., 2018. The porous TiO<sub>2</sub> nanotubes/Ag<sub>3</sub>PO<sub>4</sub> heterojunction for enhancing sunlight photocatalytic activity. *J. Phys. Chem. Solids* 114, 173–178. doi:10.1016/j.jpcs.2017.11.028
- Cihlar, J., Cihlar, J., Bartonickova, E., 2013. Low-temperature sol-gel synthesis of anatase nanoparticles modified by Au, Pd and Pt and activity of TiO<sub>2</sub>/Au, Pd, Pt photocatalysts in water splitting. *J. Sol-Gel Sci. Technol.* 65, 430–442. doi:10.1007/s10971-012-2955-8
- Cuderman, P., Heath, E., 2007. Determination of UV filters and antimicrobial agents in environmental water samples. *Anal. Bioanal. Chem.* 387, 1343–1350.

- Demeestere, K., Dewulf, J., Ohno, T., Salgado, P.H., Van Langenhove, H., 2005. Visible light mediated photocatalytic degradation of gaseous trichloroethylene and dimethyl sulfide on modified titanium dioxide. *Appl. Catal. B Environ.* 61, 140–149. doi:10.1016/j.apcatb.2005.04.017
- Díaz-Cruz, M.S., Gago-Ferrero, P., Llorca, M., Barceló, D., 2012. Analysis of UV filters in tap water and other clean waters in Spain. *Anal. Bioanal. Chem.* 402, 2325–2333. doi:10.1007/s00216-011-5560-8
- Domingo, E., Beltrán, A., Sanchis, R., García, T., Solsona, B., Galindo, F., 2018. Photocatalytic Activity of Mesoporous  $\alpha$ -Fe<sub>2</sub>O<sub>3</sub> Synthesized via Soft Chemistry and Hard Template Methods for Degradation of Azo Dye Orange II. *Catal. Letters* 1–7. doi:10.1007/s10562-018-2340-5
- Dvoranova, D., Brezova, V., Mazúr, M., Malati, M.A., 2002. Investigations of metal-doped titanium dioxide photocatalysts. *Appl. Catal. B Environ.* 37, 91–105.
- Ehrhardt, M., Bouchertall, F., Hopf, H.-P., 1982. Aromatic ketones concentrated from Baltic Sea water. *Mar. Chem.* 11, 449–461.
- Estévez, E., del Carmen Cabrera, M., Molina-Díaz, A., Robles-Molina, J., del Pino Palacios-Díaz, M., 2012. Screening of emerging contaminants and priority substances (2008/105/EC) in reclaimed water for irrigation and groundwater in a volcanic aquifer (Gran Canaria, Canary Islands, Spain). *Sci. Total Environ.* 433, 538–546.
- Fuerte, A., Hernández-Alonso, M.D., Maira, A.J., Martínez-Arias, A., Fernández-García, M., Conesa, J.C., Soria, J., 2001. Visible light-activated nanosized doped-TiO<sub>2</sub> photocatalysts. *Chem. Commun.* 0, 2718–2719. doi:10.1039/b107314a
- Gan, X., Zheng, R., Liu, T., Meng, J., Chen, R., Sun, X., Sun, X., 2017. N-Doped Mesoporous In<sub>2</sub>O<sub>3</sub> for Photocatalytic Oxygen Evolution from the In-based Metal–Organic Frameworks. *Chem. - A Eur. J.* 23, 7264–7271. doi:10.1002/chem.201605576
- Garrido, T., Fraile, J., Niñerola, J.M., Figueras, M., Ginebreda, A., Olivella, L., 2000. Survey of ground water pesticide pollution on rural areas of Catalonia (Spain). *Int. J. Environ. Anal.*

Chem. 78, 51–65.

- Gong, P., Yuan, H., Zhai, P., Xue, Y., Li, H., Dong, W., Mailhot, G., 2015. Investigation on the degradation of benzophenone-3 by UV/H<sub>2</sub>O<sub>2</sub> in aqueous solution. *Chem. Eng. J.* 277, 97–103. doi:10.1016/j.cej.2015.04.078
- Guo, Q., Li, H., Zhang, Q., Zhang, Y., 2018. Fabrication, characterization and mechanism of a novel Z-scheme Ag<sub>3</sub>PO<sub>4</sub>/NG/polyimide composite photocatalyst for microcystin-LR degradation. *Appl. Catal. B Environ.* 229, 192–203. doi:10.1016/j.apcatb.2018.02.023
- Guo, Y., Yang, X., Ma, F., Li, K., Xu, L., Yuan, X., Guo, Y., 2010. Additive-free controllable fabrication of bismuth vanadates and their photocatalytic activity toward dye degradation. *Appl. Surf. Sci.* 256, 2215–2222. doi:10.1016/j.apsusc.2009.09.076
- Hai, K., Tang, D., Wang, X.G., 2013. Effect of an oxidizing environment on the phase structure of lead oxide nanowires. *AIP Adv.* 3. doi:10.1063/1.4793208
- He, G.H., Liang, C.J., Ou, Y. Da, Liu, D.N., Fang, Y.P., Xu, Y.H., 2013. Preparation of novel Sb<sub>2</sub>O<sub>3</sub>/WO<sub>3</sub> photocatalysts and their activities under visible light irradiation. *Mater. Res. Bull.* 48, 2244–2249. doi:10.1016/j.materresbull.2013.02.055
- He, J., Wang, W., Long, F., Zou, Z., Fu, Z., Xu, Z., 2012. Hydrothermal synthesis of hierarchical rose-like Bi<sub>2</sub>WO<sub>6</sub> microspheres with high photocatalytic activities under visible-light irradiation. *Mater. Sci. Eng. B* 177, 967–974. doi:10.1016/j.mseb.2012.04.018
- Hoon, T., Wook, D., Won, S., Sun, I., Hoe, D., Soo, H., Sun, K., 2012. Facile hydrothermal synthesis of InVO<sub>4</sub> microspheres and their visible-light photocatalytic activities. *Mater. Lett.* 72, 98–100. doi:10.1016/j.matlet.2011.12.013
- Hu, P., Long, M., 2016. Cobalt-catalyzed sulfate radical-based advanced oxidation: a review on heterogeneous catalysts and applications. *Appl. Catal. B Environ.* 181, 103–117.
- Hu, Y., Tsai, H.-L., Huang, C.-L., 2003. Effect of brookite phase on the anatase–rutile transition in titania nanoparticles. *J. Eur. Ceram. Soc.* 23, 691–696.
- Huerta-Fontela, M., Galceran, M.T., Ventura, F., 2008. Stimulatory drugs of abuse in surface

- waters and their removal in a conventional drinking water treatment plant. *Environ. Sci. Technol.* 42, 6809–6816.
- Ishibai, Y., Sato, J., Akita, S., Nishikawa, T., Miyagishi, S., 2007. Photocatalytic oxidation of NO<sub>x</sub> by Pt-modified TiO<sub>2</sub> under visible light irradiation. *J. Photochem. Photobiol. A Chem.* 188, 106–111. doi:10.1016/j.jphotochem.2006.11.026
- Iwaszuk, A., Nolan, M., 2013. Lead oxide-modified TiO<sub>2</sub> photocatalyst: Tuning light absorption and charge carrier separation by lead oxidation state. *Catal. Sci. Technol.* 3, 2000–2008. doi:10.1039/c3cy00194f
- Jiang, L., Yuan, X., Zeng, G., Liang, J., Chen, X., Yu, H., Wang, H., Wu, Z., Zhang, J., Xiong, T., 2018. In-situ synthesis of direct solid-state dual Z-scheme WO<sub>3</sub>/g-C<sub>3</sub>N<sub>4</sub>/Bi<sub>2</sub>O<sub>3</sub> photocatalyst for the degradation of refractory pollutant. *Appl. Catal. B Environ.* 227, 376–385. doi:10.1016/j.apcatb.2018.01.042
- Jonjana, S., Phuruangrat, A., Thongtem, T., Kuntalue, B., Thongtem, S., 2018. Decolorization of rhodamine B photocatalyzed by Ag<sub>3</sub>PO<sub>4</sub>/Bi<sub>2</sub>WO<sub>6</sub> nanocomposites under visible radiation. *Mater. Lett.* 218, 146–149. doi:10.1016/j.matlet.2018.01.176
- Jorgenson, Z.G., Thomas, L.M., Elliott, S.M., Cavallin, J.E., Randolph, E.C., Choy, S.J., Alvarez, D.A., Banda, J.A., Gefell, D.J., Lee, K.E., 2018. Contaminants of emerging concern presence and adverse effects in fish: A case study in the Laurentian Great Lakes. *Environ. Pollut.* 236, 718–733.
- Jurado, A., Vázquez-Suñé, E., Carrera, J., de Alda, M.L., Pujades, E., Barceló, D., 2012. Emerging organic contaminants in groundwater in Spain: a review of sources, recent occurrence and fate in a European context. *Sci. Total Environ.* 440, 82–94.
- Kashyout, A.B., Soliman, M., Fathy, M., 2010. Effect of preparation parameters on the properties of TiO<sub>2</sub> nanoparticles for dye sensitized solar cells. *Renew. Energy* 35, 2914–2920. doi:10.1016/j.renene.2010.04.035
- Köck-Schulmeyer, M., Ginebreda, A., de Alda, M.L., Barceló, D., 2012. Fate and risks of polar pesticides in groundwater samples of Catalonia, in: *Emerging Organic Contaminants and*

- Human Health. Springer, pp. 375–394.
- Krause, M., Frederiksen, H., Sundberg, K., Jørgensen, F.S., Jensen, L.N., Nørgaard, P., Jørgensen, C., Ertberg, P., Juul, A., Drzewiecki, K.T., 2018. Presence of benzophenones commonly used as UV filters and absorbers in paired maternal and fetal samples. *Environ. Int.* 110, 51–60.
- Kruk, M., Jaroniec, M., 2001. Gas adsorption characterization of ordered organic-inorganic nanocomposite materials. *Chem. Mater.* doi:10.1021/cm0101069
- Lacorte, S., Latorre, A., Guillamon, M., Barceló, D., 2002. Nonylphenol, octylphenol, and bisphenol a in groundwaters as a result of agronomic practices. *Sci. World J.* 2, 1095–1100.
- Lambropoulou, D.A., Giokas, D.L., Sakkas, V.A., Albanis, T.A., Karayannis, M.I., 2002. Gas chromatographic determination of 2-hydroxy-4-methoxybenzophenone and octyldimethyl-p-aminobenzoic acid sunscreen agents in swimming pool and bathing waters by solid-phase microextraction. *J. Chromatogr. A* 967, 243–253.
- Lapworth, D.J., Baran, N., Stuart, M.E., Ward, R.S., 2012. Emerging organic contaminants in groundwater: a review of sources, fate and occurrence. *Environ. Pollut.* 163, 287–303.
- Lassner, E., Schubert, W., 1999. Tungsten: properties, chemistry, technology of the elements, alloys, and chemical compounds, *Chemistry, Technology of the Element, Alloys, and ....* doi:10.1007/978-1-4615-4907-9
- Lee, G.-J., Wu, J.J., 2017. Recent developments in ZnS photocatalysts from synthesis to photocatalytic applications — A review. *Powder Technol.* 318, 8–22. doi:10.1016/j.powtec.2017.05.022
- Lee, K.M., Lai, C.W., Ngai, K.S., Juan, J.C., 2016. Recent developments of zinc oxide based photocatalyst in water treatment technology: A review. *Water Res.* doi:10.1016/j.watres.2015.09.045
- Lee, S., Cho, I.-S., Lee, J.H., Kim, D.H., Kim, D.W., Kim, J.Y., Shin, H., Lee, J.-K., Jung, H.S., Park, N.-G., 2010. Two-step sol-gel method-based TiO<sub>2</sub> nanoparticles with uniform morphology and size for efficient photo-energy conversion devices. *Chem. Mater.* 22, 1958–1965.

- Leelavathi, A., Mukherjee, B., Nethravathi, C., Kundu, S., Dhivya, M., Ravishankar, N., Madras, G., 2013. Highly photoactive heterostructures of PbO quantum dots on TiO<sub>2</sub>. *RSC Adv.* 3, 20970. doi:10.1039/c3ra44301a
- Li, F.B., Li, X.Z., 2002. The enhancement of photodegradation efficiency using Pt-TiO<sub>2</sub> catalyst. *Chemosphere* 48, 1103–1111. doi:10.1016/S0045-6535(02)00201-1
- Li, H., Zhao, G., Chen, Z., Han, G., Song, B., 2010. Low temperature synthesis of visible light-driven vanadium doped titania photocatalyst. *J. Colloid Interface Sci.* 344, 247–250. doi:10.1016/j.jcis.2010.01.019
- Li, X., Shen, R., Ma, S., Chen, X., Xie, J., 2018. Graphene-based heterojunction photocatalysts. *Appl. Surf. Sci.* 430, 53–107. doi:10.1016/j.apsusc.2017.08.194
- Li, X., Yu, J., Wageh, S., Al-Ghamdi, A.A., Xie, J., 2016. Graphene in Photocatalysis: A Review. *Small*. doi:10.1002/sml.201600382
- Li, X.Z., Li, F.B., 2001. Study of Au/Au<sup>3+</sup>-TiO<sub>2</sub> photocatalysts toward visible photooxidation for water and wastewater treatment. *Environ. Sci. Technol.* 35, 2381–2387.
- Lin, L., Lin, W., Zhu, Y., Zhao, B., Xie, Y., 2005. Phosphor-doped Titania —a Novel Photocatalyst Active in Visible Light. *Chem. Lett.* 34, 284–285. doi:10.1246/cl.2005.284
- Linsebigler, A.L., Lu, G., Yates, J.T., 1995. Photocatalysis on TiO<sub>2</sub> Surfaces: Principles, Mechanisms, and Selected Results. *Chem. Rev.* 95, 735–758. doi:10.1021/cr00035a013
- Liu, C., Huang, H., Cui, W., Dong, F., Zhang, Y., 2018. Band structure engineering and efficient charge transport in oxygen substituted g-C<sub>3</sub>N<sub>4</sub> for superior photocatalytic hydrogen evolution. *Appl. Catal. B Environ.* 230, 115–124. doi:10.1016/j.apcatb.2018.02.038
- Liu, D.-N., He, G.-H., Zhu, L., Zhou, W.-Y., Xu, Y.-H., 2012. Enhancement of photocatalytic activity of TiO<sub>2</sub> nanoparticles by coupling Sb<sub>2</sub>O<sub>3</sub>. *Appl. Surf. Sci.* 258, 8055–8060.
- Liu, H., Sun, P., Feng, M., Liu, H., Yang, S., Wang, L., Wang, Z., 2016. Nitrogen and sulfur co-doped CNT-COOH as an efficient metal-free catalyst for the degradation of UV filter BP-4 based on sulfate radicals. *Appl. Catal. B Environ.* 187, 1–10.

- Maisang, W., Phuruangrat, A., Randorn, C., Kungwankunakorn, S., Thongtem, S., Wiranwetchayan, O., Wannapop, S., Choopun, S., Kaowphong, S., Thongtem, T., 2017. Enhanced photocatalytic performance of visible-light-driven BiOBr/BiPO<sub>4</sub>composites. *Mater. Sci. Semicond. Process.* doi:10.1016/j.mssp.2017.11.002
- Marci, G., Augugliaro, V., López-Muñoz, M.J., Martín, C., Palmisano, L., Rives, V., Schiavello, M., Tilley, R.J.D., Venezia, A.M., 2001. Preparation characterization and photocatalytic activity of polycrystalline ZnO/TiO<sub>2</sub> systems. 1. Surface and bulk characterization. *J. Phys. Chem. B* 105, 1026–1032.
- Marschall, R., 2014. Semiconductor composites: Strategies for enhancing charge carrier separation to improve photocatalytic activity. *Adv. Funct. Mater.* 24, 2421–2440. doi:10.1002/adfm.201303214
- Medina, J.C., Portillo-Vélez, N.S., Bizarro, M., Hernández-Gordillo, A., Rodil, S.E., 2018. Synergistic effect of supported ZnO/Bi<sub>2</sub>O<sub>3</sub> heterojunctions for photocatalysis under visible light. *Dye. Pigment.* 153, 106–116.
- Moon, J., Yun, C.Y., Chung, K.W., Kang, M.S., Yi, J., 2003. Photocatalytic activation of TiO<sub>2</sub> under visible light using Acid Red 44. *Catal. Today* 87, 77–86. doi:10.1016/j.cattod.2003.10.009
- Murugesan, N., Remona, A.M., Kumar, S.K., Suresh, S., 2018. Facile preparation of diverse copper oxide nanostructures and their characterization. *Mater. Lett.* 222, 100–104. doi:10.1016/j.matlet.2018.03.151
- Naidu, R., Arias Espana, V.A., Liu, Y., Jit, J., 2016. Emerging contaminants in the environment: Risk-based analysis for better management. *Chemosphere* 154, 350–357. doi:10.1016/j.chemosphere.2016.03.068
- Ohno, T., Mitsui, T., Matsumura, M., 2003. Photocatalytic Activity of S-doped TiO<sub>2</sub> Photocatalyst under Visible Light. *Chem. Lett.* 32, 364–365. doi:10.1246/cl.2003.364
- Ohtani, B., 2011. Photocatalysis by inorganic solid materials: Revisiting its definition, concepts, and experimental procedures, in: *Advances in Inorganic Chemistry*. Elsevier, pp. 395–430.

- Pan, D., Ge, S., Zhang, X., Mai, X., Li, S., Guo, Z., 2018. Synthesis and photoelectrocatalytic activity of  $\text{In}_2\text{O}_3$  hollow microspheres *via* a bio-template route using yeast templates. *Dalt. Trans.* 47, 708–715. doi:10.1039/C7DT03878J
- Pattnaik, S.P., Behera, A., Martha, S., Acharya, R., Parida, K., 2018. Synthesis, photoelectrochemical properties and solar light-induced photocatalytic activity of bismuth ferrite nanoparticles. *J. Nanoparticle Res.* 20. doi:10.1007/s11051-017-4110-5
- Pelaez, M., Nolan, N.T., Pillai, S.C., Seery, M.K., Falaras, P., Kontos, A.G., Dunlop, P.S.M., Hamilton, J.W.J., Byrne, J.A., O'Shea, K., Entezari, M.H., Dionysiou, D.D., 2012. A review on the visible light active titanium dioxide photocatalysts for environmental applications. *Appl. Catal. B Environ.* 125, 331–349. doi:10.1016/j.apcatb.2012.05.036
- Pennington, M.J., Rothman, J.A., Jones, M.B., McFrederick, Q.S., Gan, J., Trumble, J.T., 2018. Effects of contaminants of emerging concern on *Myzus persicae* (Sulzer, Hemiptera: Aphididae) biology and on their host plant, *Capsicum annuum*. *Environ. Monit. Assess.* 190, 125.
- Praus, P., Svoboda, L., Dvorský, R., Reli, M., Kormunda, M., Mančík, P., 2017. Synthesis and properties of nanocomposites of  $\text{WO}_3$  and exfoliated g-C $_3$ N $_4$ . *Ceram. Int.* 43, 13581–13591. doi:10.1016/J.CERAMINT.2017.07.067
- Radjenović, J., Petrović, M., Ventura, F., Barceló, D., 2008. Rejection of pharmaceuticals in nanofiltration and reverse osmosis membrane drinking water treatment. *Water Res.* 42, 3601–3610.
- Reddy, C.V., Babu, B., Reddy, I.N., Shim, J., 2018. Synthesis and characterization of pure tetragonal  $\text{ZrO}_2$  nanoparticles with enhanced photocatalytic activity. *Ceram. Int.* 44, 6940–6948.
- Rehman, S., Ullah, R., Butt, A.M., Gohar, N.D., 2009. Strategies of making  $\text{TiO}_2$  and  $\text{ZnO}$  visible light active. *J. Hazard. Mater.* 170, 560–569. doi:10.1016/j.jhazmat.2009.05.064
- Rodriguez-Narvaez, O.M., Peralta-Hernandez, J.M., Goonetilleke, A., Bandala, E.R., 2017. Treatment technologies for emerging contaminants in water: A review. *Chem. Eng. J.*

doi:10.1016/j.cej.2017.04.106

- Santos, A.J.M., Miranda, M.S., Esteves da Silva, J.C.G., 2012. The degradation products of UV filters in aqueous and chlorinated aqueous solutions. *Water Res.* 46, 3167–3176. doi:10.1016/j.watres.2012.03.057
- Sato, J., Kobayashi, H., Saito, N., Nishiyama, H., Inoue, Y., 2003. Photocatalytic activities for water decomposition of RuO<sub>2</sub>-loaded AInO<sub>2</sub> (A = Li, Na) with d10 configuration. *J. Photochem. Photobiol. A Chem.* 158, 139–144. doi:10.1016/S1010-6030(03)00028-5
- Sato, J., Saito, N., Nishiyama, H., Inoue, Y., 2002. Photocatalytic water decomposition by RuO<sub>2</sub>-loaded antimonates, M<sub>2</sub>Sb<sub>2</sub>O<sub>7</sub> (M = Ca, Sr), CaSb<sub>2</sub>O<sub>6</sub> and NaSbO<sub>3</sub>, with d10 configuration. *J. Photochem. Photobiol. A Chem.* 148, 85–89. doi:10.1016/S1010-6030(02)00076-X
- Schlumpf, M., Schmid, P., Durrer, S., Conscience, M., Maerkel, K., Henseler, M., Gruetter, M., Herzog, I., Reolon, S., Ceccatelli, R., 2004. Endocrine activity and developmental toxicity of cosmetic UV filters—an update. *Toxicology* 205, 113–122.
- Seabra, M.P., Salvado, I.M.M., Labrincha, J.A., 2011. Pure and (zinc or iron) doped titania powders prepared by sol-gel and used as photocatalyst. *Ceram. Int.* 37, 3317–3322. doi:10.1016/j.ceramint.2011.04.127
- Serpone, N., 2006. Is the band gap of pristine TiO<sub>2</sub> narrowed by anion- and cation-doping of titanium dioxide in second-generation photocatalysts? *J. Phys. Chem. B* 110, 24287–24293. doi:10.1021/jp065659r
- Serpone, N., Dondi, D., Albini, A., 2007. Inorganic and organic UV filters: Their role and efficacy in sunscreens and suncare products. *Inorganica Chim. Acta* 360, 794–802.
- Serpone, N., Salinaro, A., Emeline, A. V, Horikoshi, S., Hidaka, H., Zhao, J., 2002. An in vitro systematic spectroscopic examination of the photostabilities of a random set of commercial sunscreen lotions and their chemical UVB/UVA active agents. *Photochem. Photobiol. Sci.* 1, 970–981.
- Shaath, N.A., 1987. On the theory of ultraviolet absorption by sunscreen chemicals. *J. Soc. Cosmet. Chem* 82, 193–207.

- Shang, M., Wang, W.Z., Sun, S.M., Zhou, L., Zhang, L., 2008. Bi<sub>2</sub>WO<sub>6</sub> nanocrystals with high photocatalytic activities under visible light. *J. Phys. Chem. C* 112, 10407–10411. doi:10.1021/jp802115w
- Shen, M., Wu, Z., Huang, H., Du, Y., Zou, Z., Yang, P., 2006. Carbon-doped anatase TiO<sub>2</sub> obtained from TiC for photocatalysis under visible light irradiation, *Materials Letters*. doi:10.1016/j.matlet.2005.09.068
- Sillanpää, M., Ncibi, M.C., Matilainen, A., 2018. Advanced oxidation processes for the removal of natural organic matter from drinking water sources: A comprehensive review. *J. Environ. Manage.* 208, 56–76.
- Sillanpää, M., Shestakova, M., Sillanpää, M., Shestakova, M., 2017. Electrochemical Water Treatment Methods, in: *Electrochemical Water Treatment Methods*. pp. 47–130. doi:10.1016/B978-0-12-811462-9.00002-5
- Silvia Díaz-Cruz, M., Llorca, M., Barceló, D., Barceló, D., 2008. Organic UV filters and their photodegradates, metabolites and disinfection by-products in the aquatic environment. *TrAC - Trends Anal. Chem.* 27, 873–887. doi:10.1016/j.trac.2008.08.012
- Sirés, I., Brillas, E., Oturan, M.A., Rodrigo, M.A., Panizza, M., 2014. Electrochemical advanced oxidation processes: today and tomorrow. A review. *Environ. Sci. Pollut. Res.* 21, 8336–8367.
- Sophia A., C., Lima, E.C., 2018. Removal of emerging contaminants from the environment by adsorption. *Ecotoxicol. Environ. Saf.* 150, 1–17. doi:10.1016/j.ecoenv.2017.12.026
- Srinivasan, A., Miyauchi, M., 2012. Chemically stable WO<sub>3</sub> based thin-film for visible-light induced oxidation and superhydrophilicity. *J. Phys. Chem. C* 116, 15421–15426. doi:10.1021/jp303472p
- Tan, Y., Shu, Z., Zhou, J., Li, T., Wang, W., Zhao, Z., 2018. One-step synthesis of nanostructured g-C<sub>3</sub>N<sub>4</sub>/TiO<sub>2</sub> composite for highly enhanced visible-light photocatalytic H<sub>2</sub> evolution. *Appl. Catal. B Environ.* 230, 260–268. doi:10.1016/J.APCATB.2018.02.056
- Tejón, G., Candela, L., Tamoh, K., Molina-Díaz, A., Fernández-Alba, A.R., 2010. Occurrence of

- emerging contaminants, priority substances (2008/105/CE) and heavy metals in treated wastewater and groundwater at Depurbaix facility (Barcelona, Spain). *Sci. Total Environ.* 408, 3584–3595.
- Teo, T.L.L., Coleman, H.M., Khan, S.J., 2015. Chemical contaminants in swimming pools: Occurrence, implications and control. *Environ. Int.* 76, 16–31. doi:10.1016/j.envint.2014.11.012
- Vasudevan, S., Oturan, M.A., 2014. Electrochemistry: as cause and cure in water pollution—an overview. *Environ. Chem. Lett.* 12, 97–108.
- Vidal, L., Chisvert, A., Canals, A., Salvador, A., 2010. Ionic liquid-based single-drop microextraction followed by liquid chromatography-ultraviolet spectrophotometry detection to determine typical UV filters in surface water samples. *Talanta* 81, 549–555.
- Vione, D., Caringella, R., De Laurentiis, E., Pazzi, M., Minero, C., 2013. Phototransformation of the sunlight filter benzophenone-3 (2-hydroxy-4-methoxybenzophenone) under conditions relevant to surface waters. *Sci. Total Environ.* 463–464, 243–251. doi:10.1016/j.scitotenv.2013.05.090
- Wang, J., Huang, J., Meng, J., Li, Q., Yang, J., 2016. Double-hole codoped huge-gap semiconductor  $ZrO_2$  for visible-light photocatalysis. *Phys. Chem. Chem. Phys.* 18, 17517–17524. doi:10.1039/C6CP02047J
- Wang, T.X., Xu, S.H., Yang, F.X., 2012.  $ZnIn_2S_4$  nanopowder as an efficient visible light-driven photocatalyst in the reduction of aqueous Cr(VI). *Mater. Lett.* 83, 46–48. doi:10.1016/j.matlet.2012.05.121
- Wang, Y., Jiang, L., Liu, Y., Tang, D., Liu, F., Lai, Y., 2017. Facile synthesis and photoelectrochemical characterization of  $Sb_2O_3$  nanoprism arrays. *J. Alloys Compd.* 727, 469–474. doi:10.1016/j.jallcom.2017.08.106
- Wei, R. Bin, Huang, Z.L., Gu, G.H., Wang, Z., Zeng, L., Chen, Y., Liu, Z.Q., 2018. Dual-cocatalysts decorated rimous CdS spheres advancing highly-efficient visible-light photocatalytic hydrogen production. *Appl. Catal. B Environ.* 231, 101–107.

doi:10.1016/j.apcatb.2018.03.014

- Wu, D., Zhang, R., Lu, G., Lin, Q., Liu, F., Li, Y., 2017. Degradation of Octocrylene Using Combined Ozonation and Electrolysis Process: Optimization by Response Surface Methodology. *CLEAN - Soil, Air, Water* 45, 1500664. doi:10.1002/clen.201500664
- Wu, J.C.S., Chen, C.H., 2004. A visible-light response vanadium-doped titania nanocatalyst by sol-gel method. *J. Photochem. Photobiol. A Chem.* 163, 509–515. doi:10.1016/j.jphotochem.2004.02.007
- Xia, C., Jia, Y., Tao, M., Zhang, Q., 2013. Tuning the band gap of hematite  $\alpha$ -Fe<sub>2</sub>O<sub>3</sub> by sulfur doping. *Phys. Lett. Sect. A Gen. At. Solid State Phys.* 377, 1943–1947. doi:10.1016/j.physleta.2013.05.026
- Xie, B., Zhang, H., Cai, P., Qiu, R., Xiong, Y., 2006. Simultaneous photocatalytic reduction of Cr(VI) and oxidation of phenol over monoclinic BiVO<sub>4</sub> under visible light irradiation. *Chemosphere* 63, 956–963. doi:10.1016/j.chemosphere.2005.08.064
- Xiong, Z., Wang, H., Xu, N., Li, H., Fang, B., Zhao, Y., Zhang, J., Zheng, C., 2015. Photocatalytic reduction of CO<sub>2</sub> on Pt<sup>2+</sup>-Pt<sup>0</sup>/TiO<sub>2</sub> nanoparticles under UV/Vis light irradiation: A combination of Pt<sup>2+</sup> doping and Pt nanoparticles deposition. *Int. J. Hydrogen Energy* 40, 10049–10062. doi:10.1016/j.ijhydene.2015.06.075
- Yan, Y., Liu, X., Fan, W., Lv, P., Shi, W., 2012. InVO<sub>4</sub> microspheres: Preparation, characterization and visible-light-driven photocatalytic activities. *Chem. Eng. J.* 200–202, 310–316. doi:10.1016/j.cej.2012.05.102
- Yang, H.G., Sun, C.H., Qiao, S.Z., Zou, J., Liu, G., Smith, S.C., Cheng, H.M., Lu, G.Q., 2008. Anatase TiO<sub>2</sub> single crystals with a large percentage of reactive facets. *Nature* 453, 638–641. doi:10.1038/nature06964
- Yang, K., Dai, Y., Huang, B., 2007. Understanding photocatalytic activity of S- And P-doped TiO<sub>2</sub> under visible light from first-principles. *J. Phys. Chem. C* 111, 18985–18994. doi:10.1021/jp0756350
- Yin, J., Zou, Z., Ye, J., 2003. Photophysical and photocatalytic properties of new photocatalysts

- MCrO 4 (M=Sr, Ba). *Chem. Phys. Lett.* 378, 24–28. doi:10.1016/S0009-2614(03)01238-7
- Yin, J., Zou, Z.G., Ye, J.H., 2003. A novel series of the new visible-light-driven photocatalysts MCo1/3Nb2/3O3 (M = Ca, Sr, and Ba) with special electronic structures. *J. Phys. Chem. B* 107, 4936–4941. doi:10.1021/Jp0340919
- Zeng, D.W., Xie, C.S., Zhu, B.L., Song, W.L., 2004. Characteristics of Sb2O3nanoparticles synthesized from antimony by vapor condensation method. *Mater. Lett.* 58, 312–315. doi:10.1016/S0167-577X(03)00476-2
- Zeng, Y., Wu, W., Lee, S., Gao, J., 2007. Photocatalytic performance of plasma sprayed Pt-modified TiO2 coatings under visible light irradiation. *Catal. Commun.* 8, 906–912. doi:10.1016/j.catcom.2006.09.023
- Zhang, J., Ma, Z., 2017a. Flower-like Ag3VO4/BiOBr n-p heterojunction photocatalysts with enhanced visible-light-driven catalytic activity. *Mol. Catal.* 436, 190–198. doi:10.1016/j.mcat.2017.04.004
- Zhang, J., Ma, Z., 2017b. Enhanced visible-light photocatalytic performance of Ag3VO4/Bi2WO6heterojunctions in removing aqueous dyes and tetracycline hydrochloride. *J. Taiwan Inst. Chem. Eng.* 78, 212–218. doi:10.1016/j.jtice.2017.06.002
- Zhang, L., Zhu, Y., 2012. A review of controllable synthesis and enhancement of performances of bismuth tungstate visible-light-driven photocatalysts. *Catal. Sci. Technol.* 2, 694. doi:10.1039/c2cy00411a
- Zhang, S., Chen, J., Qiao, X., Ge, L., Cai, X., Na, G., 2010. Quantum chemical investigation and experimental verification on the aquatic photochemistry of the sunscreen 2-phenylbenzimidazole-5-sulfonic acid. *Environ. Sci. Technol.* 44, 7484–7490.
- Zhang, W., Tang, J., Ye, J., 2007. Structural, photocatalytic, and photophysical properties of perovskite MSnO3 (M = Ca, Sr, and Ba) photocatalysts. *J. Mater. Res.* 22, 1859–1871. doi:10.1557/jmr.2007.0259
- Zhu, W., Qiu, X., Iancu, V., Chen, X.Q., Pan, H., Wang, W., Dimitrijevic, N.M., Rajh, T., Meyer, H.M., Paranthaman, M.P., Stocks, G.M., Weiering, H.H., Gu, B., Eres, G., Zhang, Z., 2009.

Band gap narrowing of titanium oxide semiconductors by noncompensated anion-Cation codoping for enhanced visible-Light photoactivity. *Phys. Rev. Lett.* 103. doi:10.1103/PhysRevLett.103.226401

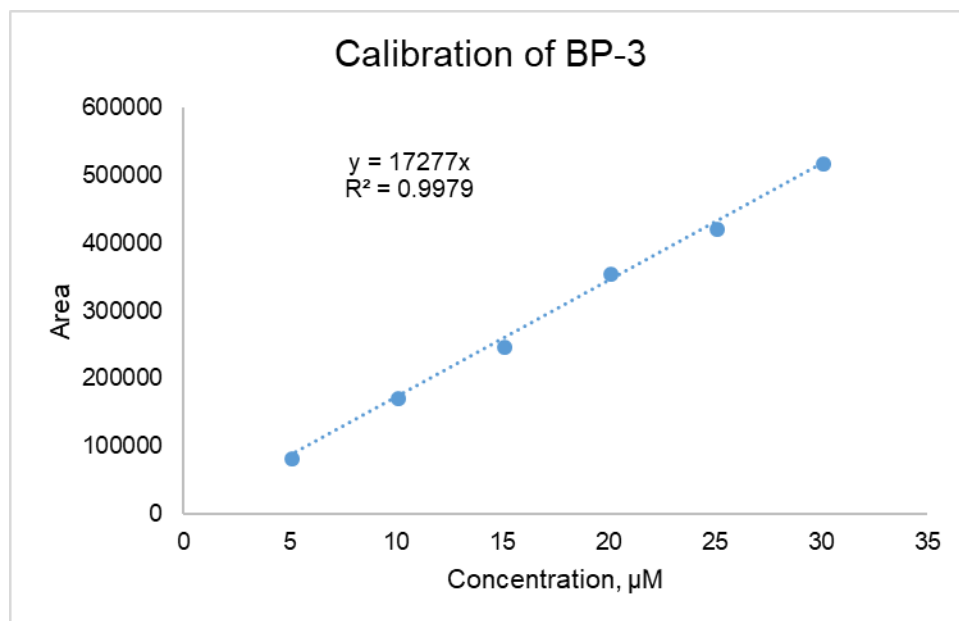
Zúñiga-Benítez, H., Aristizábal-Ciro, C., Peñuela, G.A., 2016a. Heterogeneous photocatalytic degradation of the endocrine-disrupting chemical Benzophenone-3: Parameters optimization and by-products identification. *J. Environ. Manage.* 167, 246–258. doi:10.1016/j.jenvman.2015.11.047

Zúñiga-Benítez, H., Aristizábal-Ciro, C., Peñuela, G.A., 2016b. Photodegradation of the endocrine-disrupting chemicals benzophenone-and methylparaben using Fenton reagent: Optimization of factors and mineralization/biodegradability studies. *J. Taiwan Inst. Chem. Eng.* 59, 380–388. doi:10.1016/j.jtice.2015.09.004

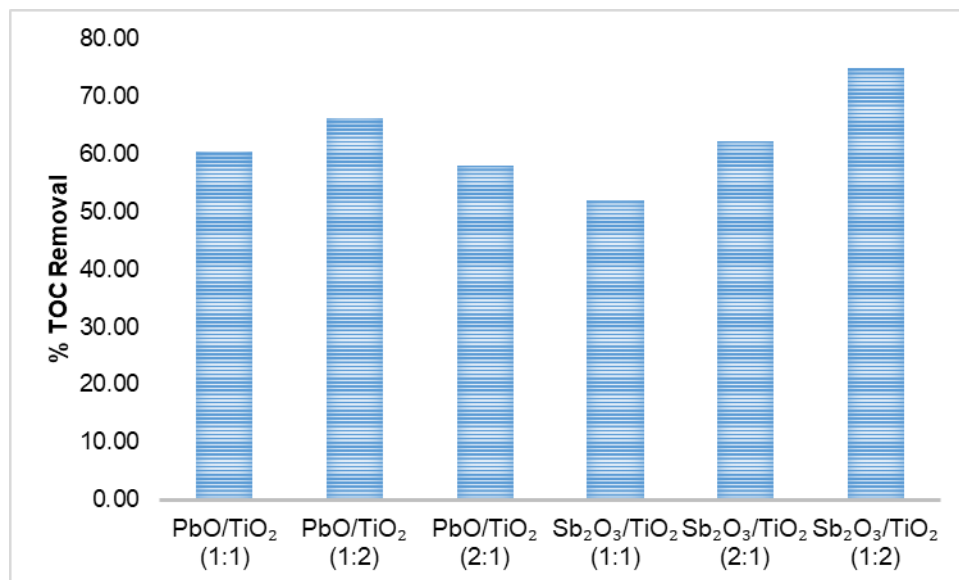
Zúñiga-Benítez, H., Soltan, J., Peñuela, G.A., 2016. Application of ultrasound for degradation of benzophenone-3 in aqueous solutions. *Int. J. Environ. Sci. Technol.* 13, 77–86.

Zwiener, C., Richardson, S.D., De Marini, D.M., Grummt, T., Glauner, T., Frimmel, F.H., 2007. Drowning in disinfection byproducts? Assessing swimming pool water. *Environ. Sci. Technol.* 41, 363–372.

## APPENDIX



Appendix Figure 1: Calibration curve of BP-3 from HPLC data.

Appendix Figure 2: TOC removal efficiency by different catalysts after 6 hr of reaction (Initial pH = 7, Initial conc. = 20  $\mu\text{M}$ , Catalyst dose = 1.0 g/L, under UV-C irradiation).

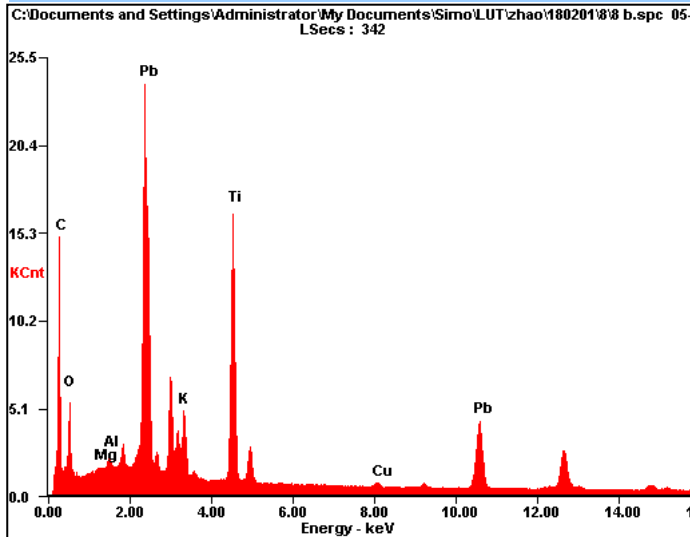
# Microanalysis Report

Prepared for: *Company Name Here*

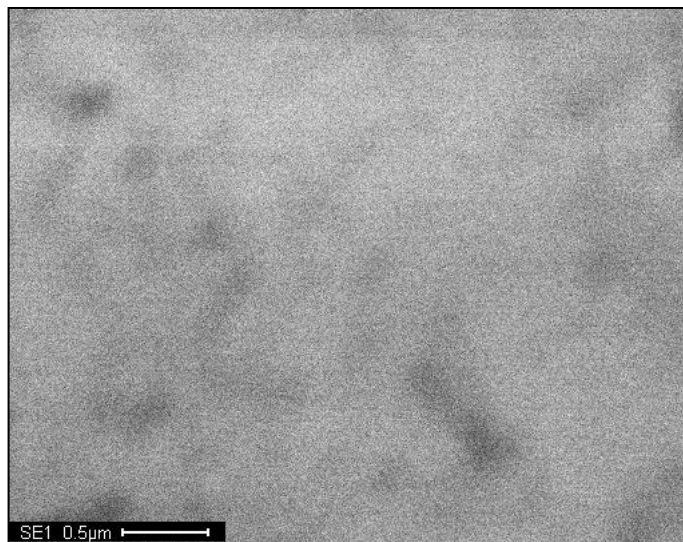
Prepared by: *Your Name Here* 2/5/2018



PbO/TiO<sub>2</sub> = 1:2



Element	Wt%	At%
<i>CK</i>	41.75	68.54
<i>OK</i>	18.86	23.24
<i>MgK</i>	00.11	00.09
<i>AlK</i>	00.53	00.39
<i>KK</i>	02.19	01.10
<i>TiK</i>	09.75	04.02
<i>CuK</i>	00.31	00.10
<i>PbL</i>	26.49	02.52
<i>Matrix</i>	Correction	ZAF



KV 30.0 MAG 17900 TILT 0.0 MICRONSPERPIXY 0.008

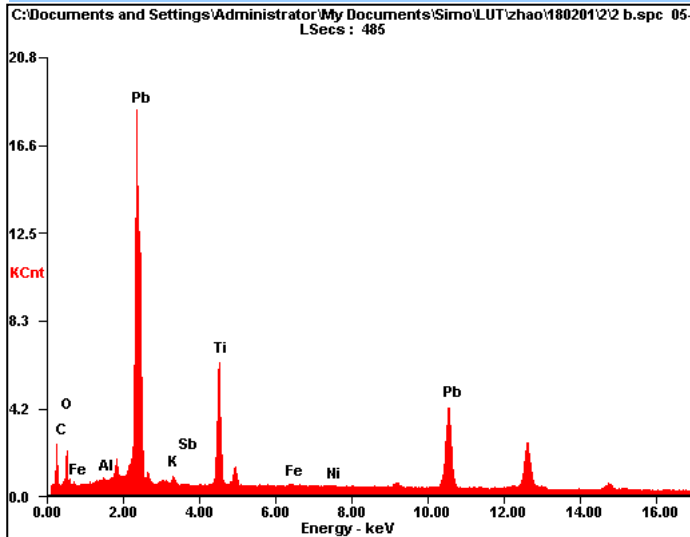
# Microanalysis Report

Prepared for: *Company Name Here*

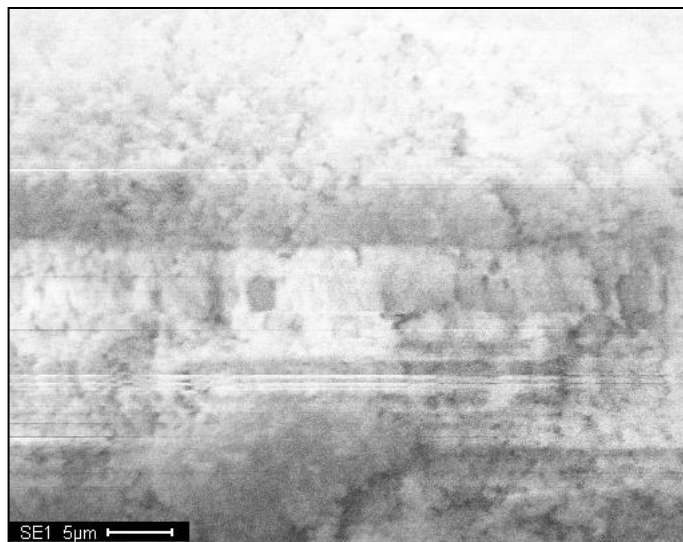
Prepared by: *Your Name Here* 2/5/2018



PbO/TiO<sub>2</sub> = 1:1



<i>Element</i>	<i>Wt%</i>	<i>At%</i>
<i>CK</i>	19.72	57.49
<i>OK</i>	10.84	23.72
<i>AlK</i>	00.21	00.27
<i>KK</i>	00.79	00.70
<i>SbL</i>	00.00	00.00
<i>TiK</i>	10.68	07.81
<i>FeK</i>	00.32	00.20
<i>NiK</i>	00.23	00.14
<i>PbL</i>	57.21	09.67
<i>Matrix</i>	Correction	ZAF

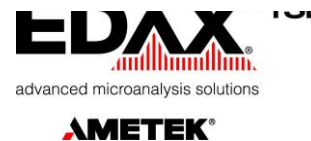


KV 30.0 MAG 1300 TILT 0.0 MICRONSPERPIXY 0.106

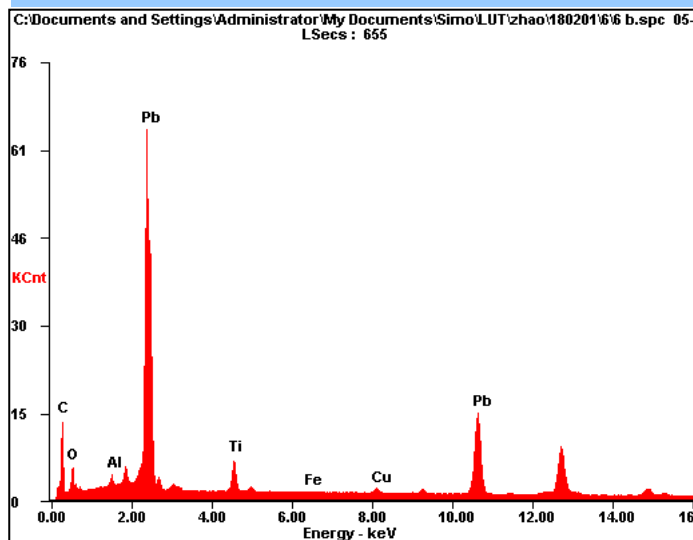
# Microanalysis Report

Prepared for: *Company Name Here*

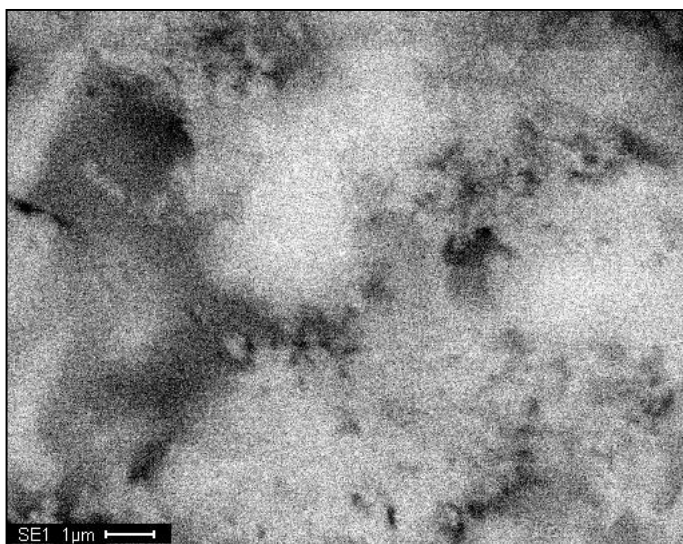
Prepared by: *Your Name Here* 2/5/2018



PbO/TiO<sub>2</sub> = 2:1



Element	Wt%	At%
<i>CK</i>	30.18	72.35
<i>OK</i>	09.53	17.15
<i>AlK</i>	00.72	00.77
<i>TiK</i>	02.66	01.60
<i>FeK</i>	00.09	00.04
<i>CuK</i>	00.61	00.28
<i>PbL</i>	56.21	07.81
<i>Matrix</i>	Correction	ZAF



KV 30.0 MAG 5000 TILT 0.0 MICRONSPERPIXY 0.027

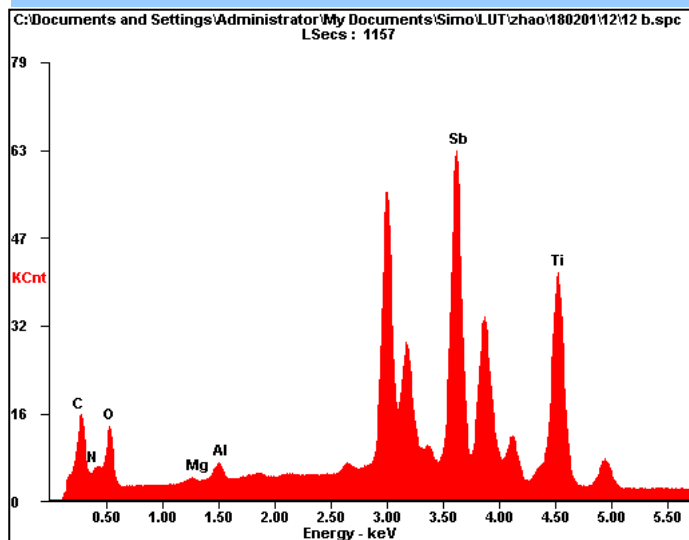
# Microanalysis Report

Prepared for: *Company Name Here*

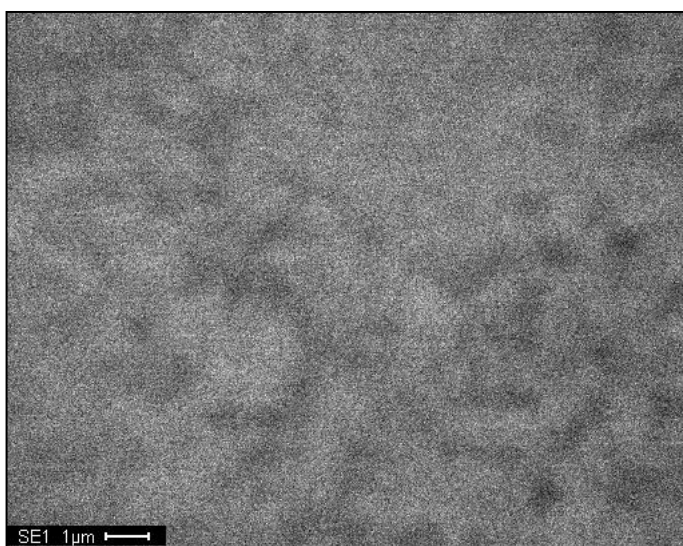
Prepared by: *Your Name Here* 2/5/2018



$Sb_2O_3/TiO_2 = 1:2$



<i>Element</i>	<i>Wt%</i>	<i>At%</i>
<i>CK</i>	24.44	43.60
<i>NK</i>	11.86	18.15
<i>OK</i>	19.57	26.21
<i>MgK</i>	00.37	00.33
<i>AlK</i>	01.28	01.02
<i>SbL</i>	30.64	05.39
<i>TiK</i>	11.83	05.29
<i>Matrix</i>	Correction	ZAF

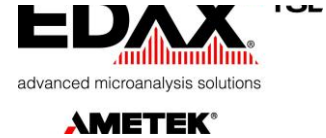


KV 30.0 MAG 4410 TILT 0.0 MICRONSPERPIXY 0.031

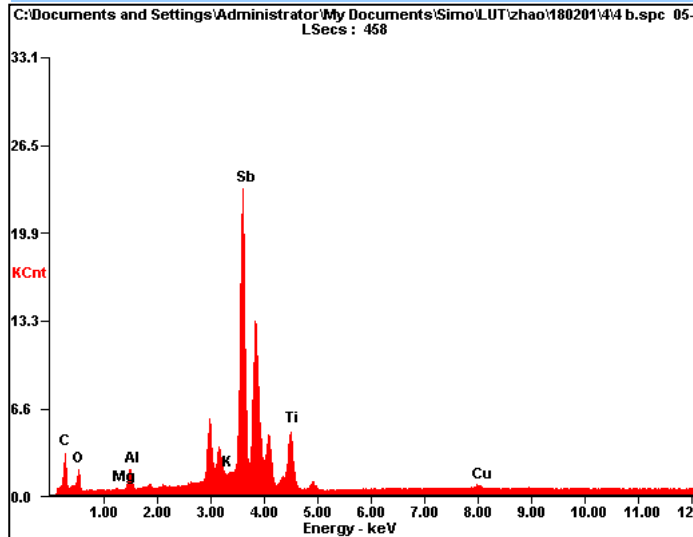
# Microanalysis Report

Prepared for: *Company Name Here*

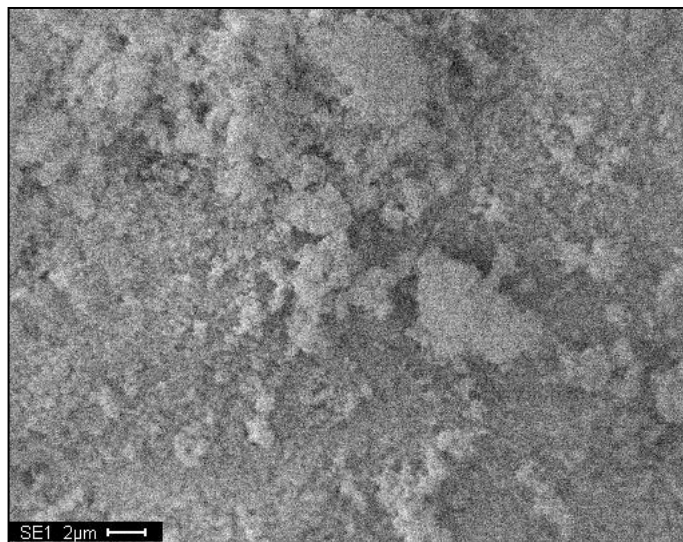
Prepared by: *Your Name Here* 2/5/2018



$Sb_2O_3/TiO_2 = 1:1$



<i>Element</i>	<i>Wt%</i>	<i>At%</i>
<i>CK</i>	18.22	53.59
<i>OK</i>	07.78	17.17
<i>MgK</i>	00.00	00.00
<i>AlK</i>	03.05	03.99
<i>KK</i>	01.16	01.05
<i>SbL</i>	60.58	17.58
<i>TiK</i>	08.27	06.10
<i>CuK</i>	00.96	00.53
<i>Matrix</i>	Correction	ZAF

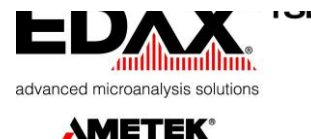


KV 30.0 MAG 2000 TILT 0.0 MICRONS PER PIXY 0.069

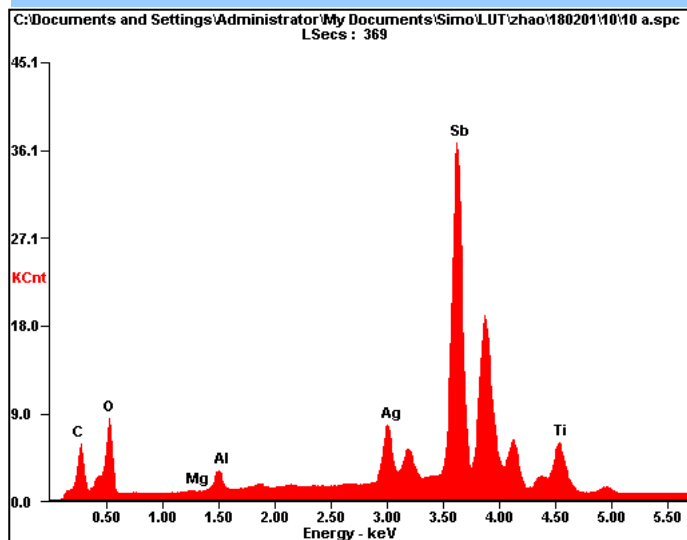
# Microanalysis Report

Prepared for: *Company Name Here*

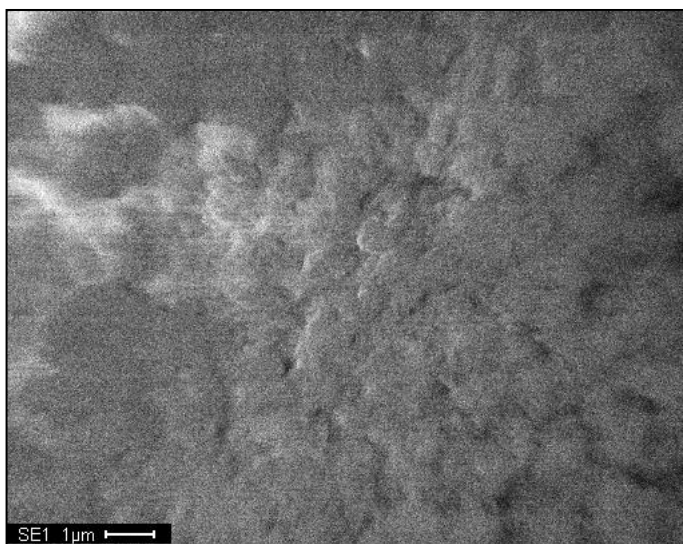
Prepared by: *Your Name Here* 2/5/2018



$Sb_2O_3/TiO_2 = 2:1$



<i>Element</i>	<i>Wt%</i>	<i>At%</i>
<i>CK</i>	16.25	43.11
<i>OK</i>	17.98	35.82
<i>MgK</i>	00.00	00.00
<i>AlK</i>	01.89	02.23
<i>AgL</i>	07.41	02.19
<i>SbL</i>	51.81	13.56
<i>TiK</i>	04.65	03.10
<i>Matrix</i>	Correction	ZAF



KV 30.0 MAG 5000 TILT 0.0 MICRONS PER PIXY 0.027